A SURFACE-TO-AIR MISSILE EQUIPPED WITH A TRACKING BASED ECCM TECHNIQUES

A THESIS SUBMITTED TO
THE GRADUATE SCHOOL OF NATURAL AND APPLIED SCIENCES
OF
MIDDLE EAST TECHNICAL UNIVERSITY

BY

RAĞIP YURTTAŞ

IN PARTIAL FULFILLMENT OF THE REQUIREMENTS
FOR
THE DEGREE OF MASTER OF SCIENCE
IN
ELECTRICAL AND ELECTRONICS ENGINEERING

SEPTEMBER 2013

Approval of the thesis:

A SURFACE-TO-AIR MISSILE EQUIPPED WITH A TRACKING BASED ECCM TECHNIQUES

submitted by **RAĞIP YURTTAŞ** in partial fulfillment of the requirements for the degree of **Master of Science in Electrical and Electronics Engineering Department, Middle East Technical University** by,

Prof. Dr. Canan Özgen _____
Dean, Graduate School of **Natural and Applied Sciences**

Prof. Dr. Gönül Turhan Sayan _____
Head of Department, **Electrical and Electronics Engineering**

Prof. Dr. Kemal Leblebicioğlu _____
Supervisor, **Electrical and Electronics Eng. Dept., METU**

Examining Committee Members:

Prof. Dr. Kemal Özgören
Mechanical Engineering Department, METU _____

Prof. Dr. Kemal Leblebicioğlu
Electrical and Electronics Engineering Department, METU _____

Prof. Dr. Tolga Çiloğlu
Electrical and Electronics Engineering Department, METU _____

Prof. Dr. Şimşek Demir
Electrical and Electronics Engineering Department, METU _____

Assist. Prof. Dr. Umut Orguner
Electrical and Electronics Engineering Department, METU _____

Date: _____

I hereby declare that all information in this document has been obtained and presented in accordance with academic rules and ethical conduct. I also declare that, as required by these rules and conduct, I have fully cited and referenced all material and results that are not original to this work.

Name, Last Name: RAĞIP YURTTAŞ

Signature :

ABSTRACT

A SURFACE-TO-AIR MISSILE EQUIPPED WITH A TRACKING BASED ECCM TECHNIQUES

Yurttaş, Rağıp

M.S., Department of Electrical and Electronics Engineering

Supervisor : Prof. Dr. Kemal Leblebicioğlu

September 2013, 123 pages

Surface-to-air missiles having infrared detectors, aiming to destroy air platforms, determine the position of targets based on the infrared energy radiating from air platforms. It is possible to detect infrared signals radiating from an air platform by a missile seeker. This will enable the missile to estimate target position with respect to missile seeker. On the other hand, there are many advanced techniques developed to prevent missiles to damage targets. It is a real need for the missiles to overcome these ECM (Electronic-Counter-Measures) techniques which are carried out by air platform. In order to satisfy this basic need of missiles, certain techniques called ECCM (Electronic-Counter-Counter-Measures) techniques have been developed.

In this study, surface-to-air missile equipped with imaging infrared seeker, which has dual band Focal-Plane-Array detector, has been designed to detect target position. Infrared detector detects and measures the position of target, if the intensity of the detected infrared signals is above threshold level. In this manner, background noise is eliminated. At the same time, ECCM techniques prevent seeker to be misled by MTV (Magnesium/Teflon/Viton) and spectral flares which are ECM ammunition dispensed by an air platform.

In order to realize and test the models, simulator has been developed. Dynamic motion and 3D infrared signature models of F-16 air platform; detector, ECCM techniques, gimbal, guidance, kinematic motion models of missile; MTV and spectral flares motion and 3D infrared signature models with respect to time have been developed at simulator.

Keywords: Electronic-Counter-Measures, Electronic-Counter-Counter-Measures, Missile, Imag-

ing Infrared Seeker, Surface-to-Air Missile

ÖZ

TAKİBE DAYALI ELEKTRONİK KORUNMA TEKNİKLERİ İLE DONATILMIŞ YERDEN HAVAYA ATILAN FÜZE

Yurttaş, Rağıp

Yüksek Lisans, Elektrik ve Elektronik Mühendisliği Bölümü

Tez Yöneticisi : Prof. Dr. Kemal Leblebicioğlu

Eylül 2013 , 123 sayfa

Hava platformlarına zarar vermek amacıyla tasarlanmış kızılötesi arama başlıklı yerden havaya fırlatılan füzeler hava platformundan yayılan kızılötesi enerjiyi algılayarak hedef konum tespiti yaparlar. Hava platformundan yayılan kızılötesi sinyaller füzenin arama başlığı tarafından algılanarak hedef konum tespiti yapılır. Buna karşılık, füzelerin hedefe zarar vermesini engellemek amacıyla birçok ileri teknik geliştirilmiştir. Füzelerin hava platformu tarafından uygulanan bu Elektronik Taarruz tekniklerine karşılık vermesi ihtiyaçtır. Bu nedenle Elektronik Korunma teknikleri geliştirilmiştir.

Bu tezde, hedef konumunu kestirmek için, çift bant odak düzlem dizisi detektörüne sahip görüntülemeli kızılötesi arama başlıklı yerden havaya atılan füze tasarlanmıştır. Detektör, hedeften gelen kızılötesi sinyallerin belirlenmiş bir eşik şiddeti değeri üzerinde olması durumunda hedef konum tespiti yapmaktadır. Böylece, arka plan gürültüsü engellenecektir. Aynı zamanda, Elektronik Korunma teknikleri sayesinde hava platformu üzerinden fırlatılan Elektronik Taarruz mühimmatı MTV ve spektral ısı fişeklerinin füzenin arama başlığını yanıltması engellenecektir.

Modellerin çalışmasını gerçekleştirmek ve modelleri test edebilmek için simülatör geliştirilmiştir. Simülatörde F-16 hava platformuna ait dinamik hareket, 3B kızılötesi imza modelleri; füze için detektör, Elektronik Korunma teknikleri, gimbal, güdüm ve hareket modelleri; Elektronik Taarruz tekniği olarak MTV ve spektral ısı fişeklerinin zamana karşı hareket ve 3B kızılötesi imza modelleri geliştirilmiştir.

Anahtar Kelimeler: Elektronik Taarruz, Elektronik Korunma, Füze, Görüntülemeli Kızılötesi Arama Başlığı, Yerden Havaya Füze

To my parents, sister, nephew and nieces

Refik YURTTAŞ, Fadime YURTTAŞ, Fikriye HAYTA, Sadık Onur HAYTA, Irmak HAYTA, Asya HAYTA

ACKNOWLEDGMENTS

I would like to express my special thanks and appreciation to my supervisor Prof. Dr. Kemal LEBLEBİCİOĞLU for his constant and valuable guidance, advice, support, friendship and suggestions throughout the research. It was a great honor to work with him.

I am grateful to all of the thesis jury committee members who contributed to this thesis with their valuable comments.

This work is supported by TÜBİTAK-BİDEB Master scholarship (2210). I would like to express my thanks to TÜBİTAK- BİDEB for their support.

Special thanks to not only my residents of my project office but also all my colleagues at TUBİTAK BİLGEM İLTAREN, especially Berk AKAR, Murat Ş. ASLAN, İlhami BEKTAŞ, KAAN ERGÖZ, Şule Ş. YILMAZ, Özlem S. EKİNCİ for their feedback, suggestion and inspiration on this work.

Very special thanks to Ahmet GÜNGÖR, Onur AKIN, Hüseyin YILDIZ, M. Altan TOKSÖZ and Zeynep ESİN who have taught me real meaning of friendship recently.

Last but not least, I would like to thank to my family for their love, help, patience, motivation and support in my entire life.

TABLE OF CONTENTS

LIST OF TABLES

TABLES

LIST OF FIGURES

FIGURES

LIST OF ABBREVIATIONS

λ	Spectral band
λ_{az}	Azimuth LOS angle of missile
λ_{el}	Elevation LOS angle of missile
$\dot{\lambda}_M$	LOS rate
$\alpha(\lambda)$	Spectral absorption coefficient
α	Absorption coefficient
$\tau(\lambda)$	Spectral transmission coefficient
τ	Transmission coefficient
$\rho(\lambda)$	Spectral reflectivity coefficient
ρ	Reflectivity coefficient
$\epsilon(\lambda)$	Spectral emissivity coefficient
ϵ	Emissivity coefficient
$\zeta_{atm}(\lambda)$	Spectral atmospheric transmission
ψ, θ, ϕ	Yaw, pitch, roll Euler angles
$\dot{\psi}, \dot{\theta}, \dot{\phi}$	Euler angle rates
$\psi_{G\sim}$	Estimated gimbal yaw angle
$\theta_{G\sim}$	Estimated gimbal pitch angle
ρ_0	Sea level air density
ρ	Air density
δ_t	Throttle Setting of Aircraft
δ_a	Aileron of Aircraft
δ_e	Elevator of Aircraft
δ_r	Rudder of Aircraft
$\epsilon_{M_{az}}$	Azimuth error angle
$\epsilon_{M_{el}}$	Elevation error angle
α	Angle of attack
$\dot{\alpha}$	Angle of attack rate
β	Side-slip angle
$\dot{\beta}$	Side-slip angle rate
p, q, r	Body-coordinate angular rates
$\dot{p}, \dot{q}, \dot{r}$	Body-coordinate angular rates' derivatives
ω	Angular velocity

μ_{MD}	Mean miss distance
μ_{FT}	Mean flight time
A	Pixel area of selected object
$A^{\sim}$	Estimated area
a_c	Commanded acceleration
a_{Lat}	Lateral acceleration
a_n	Normal acceleration
A_P	Angular position
b	Reference wing span
c	Aerodynamic reference chord
C_D	Drag force coefficient
C_l, C_m, C_n	Aerodynamic coefficient of moments
c_{Light}	Velocity of light
C_X, C_Y, C_Z	Aerodynamic coefficient of forces
D	Drag force
$ECCM_{I_{area}}$	Identification block area ECCM values of source
$ECCM_{I_{AreaGate}}$	Identification block area gate percentage between 0 and 1
$ECCM_{I_{denomination}}$	Identification block denomination ECCM values of sources
$ECCM_{I_{spectral}}$	Identification block spectral ECCM values of source
$ECCM_{M_{area}}$	Matching block area ECCM values of source
$ECCM_{M_{AreaGate}}$	Matching block area gate percentage between 0 and 1
$ECCM_{M_{spectral}}$	Matching block spectral ECCM values of source
F	External force
F_X, F_Y, F_Z	External forces
G_F	Radiation gain of spectral flare
g_0	Standard gravitational acceleration
g_H	Gravity of given altitude
h	Angular momentum
h_{eng}	Angular momentum of F-16 engine
H	Altitude
I_{Binary}	Binary image
$I_{BW_{Labeled}}$	Labeled image
$I_{BW_{Morph}}$	Morphological image
I_{Gray}	Gray scaled image
I_{mc}	Indices of minor case
I_{RGB}	RGB image
I_X, I_Y, I_Z	Moments of inertia

I_{XY}, I_{XZ}, I_{YZ}	Cross-product moments of inertia
$J(\dot{\bar{x}})$	Cost function of aircraft
$L(\lambda, T)$	Spectral radiance of blackbody object
L	radiance of object
$L_{A_{Total}}$	Total radiation of aircraft
L_B	Background radiation
$L_{D_{Max}}$	Maximum detectable radiance of detector
$L_{D_{Min}}$	Minimum detectable radiance of detector
$L_{F_{Total}}$	Total radiation of flare
$L_F(t)$	Radiation of flare with a given time
$level_{BTh}$	Background threshold level
$L_{path-radiance}$	Path radiance
$L_{sky-radiance}$	Sky radiance
L_{Source}	Source radiation
m	Mass
$M_{aircraft}$	Mach number of aircraft
M	External moment
$M(\lambda, T)$	Spectral exitance of blackbody object
M_{TV}	Maneuver timing vector
M_X, M_Y, M_Z	External moments
m_C	Minor cases
M_C	Major cases
N	Navigation constant
$Name$	Name string of sources
NOS	Number of scenario
P_α	Absorbed power
P_τ	Transmitted power
P_ρ	Reflected power
P_A	Actual engine power of aircraft
$\dot{P}_A$	Actual engine power derivative of aircraft
P_B	Body-coordinate 3D position
P_C	Engine commanded power of aircraft
P_E	Earth-fixed coordinate 3D position
P_i	Incident power
P_W	Aircraft power
$\bar{q}$	Dynamic pressure
R	Ratio of LWIR and MWIR radiation

s	Maximum cross-sectional wing area of vehicle
T	Thrust force
T	Surface temperature
$T0$	Sea level temperature
T_B	Body-coordinate
t_{DIBM}	Dispense initiation before maneuver
$t_{dispense}$	Flare dispense time
T_E	Earth-fixed coordinate
T_{EB}	Transformation matrix from body-coordinate to eath-fixed coordinate
$t_{ignition}$	Flare ignition time
t_{IDT}	Flare initial dispense time
T_{I_W}	Identification block total weight of selected object
T_{M_W}	Matching block total weight of selected object
t_r	Flare rise time
T_R	Spectral thresholded pixel value (binary)
T_{Range}	Threshold distance between aircraft and missile
T_S	Stability-coordinate
T_{SB}	Transformation matrix from body-coordinate to stability-coordinate
T_{SR}	Total pixel number which exceed spectral threshold for selected object
t_b	Flare burn time
T_W	Wind-coordinate
T_{WS}	Transformation matrix from stability-coordinate to wind-coordinate
u, v, w	Body-coordinate velocities
X_B, Y_B, Z_B	Body-coordinate positions
X_C	is X axis centroid of object
$X_{C_{intensity}}$	is X axis center of selected objects with respect to intensity centroid detection
X_{CG}	Center of gravity location
X_D	X resolution of detector
X_E, Y_E, Z_E	Earth-fixed coordinate positions
X_S, Y_S, Z_S	Stability-coordinate positions
X_W, Y_W, Z_W	Wind-coordinate positions
V	Velocity
$V_{B_X}, V_{B_Y}, V_{B_Z}$	Body-coordinate 3D velocities
V_C	Closing velocity
V_{DF}	Velocity of dispensing flare
$V_{E_X}, V_{E_Y}, V_{E_Z}$	Earth-fixed coordinate 3D velocityies

V_P	Velocity profile generated by thrust force
$\dot{V}$	Velocity rate
$\vec{V}$	Velocity vector
w_1 to w_6	Cost minimization weight coefficients
W_{I_a}	Identification block weight of area ECCM
W_{I_d}	Identification block weight of denomination ECCM
W_{I_k}	Identification block weight of kinematic ECCM
W_{I_s}	Identification block weight of spectral ECCM
W_{M_a}	Matching block weight of area ECCM
W_{M_k}	Matching block weight of kinematic ECCM
W_{M_s}	Matching block weight of spectral ECCM
Y_C	is Y axis centroid of object
$Y_{C_{intensity}}$	is Y axis center of selected objects with respect to intensity centroid detection
Y_D	Y resolution of detector
AM	Amplitude Modulation
CDU	Control Display Unit
CMDS	Counter-Measure Dispensing System
DOF	Degree of Freedom
ECM	Electronic-Counter-Measure
ECCM	Electronic-Counter-Counter-Measure
ES	Electronic Support
E / O	Electro-optics
FASCODE	Fast Atmospheric Signature Code
FM	Frequency Modulation
FOR	Field of Regard
FOV	Field of View
FPA	Focal Plane Array
$(Hg_{1-x}Cd_xTe)$	Mercury-Cadium-Telluride
HITRAN	High Resolution Transmission
IFOV	Instantaneous Field of View
IIR	Imaging Infrared
InSb	Indium Antimonide
IR	Infrared
IRCM	Infrared Counter-Measure
LOS	Line of Sight
LOWTRAN	Low Resolution Transmission Model

LWIR	Long-wave Infrared
MANPAD	Man-portable-air Defense System
MATLAB	Matrix Laboratory
MODTRAN	Moderate Resolution Atmospheric Transmission
MTV	Magnesium/Teflon/Viton
MWIR	Mid-wave Infrared
MWS	Missile Warning System
NEP	Noise Equivalent Power
NIR	Near Infrared
NSM	Naval Strike Missile
PbS	Lead Sulphide
PbSe	Lead Selenide
PNG	Proportional Navigation Guidance
RGB	Red Green Blue
RWR	Radar Warning Receiver
SIMULINK	Simulation and Model-Based Design
SNR	Signal to Noise Ratio
SWIR	Short-wave Infrared
TPNG	True Proportional Navigation Guidance
USA	United States of America
UV	Ultraviolet
VLWIR	Very Long-wave Infrared
VRML	Virtual Reality Modeling Language
3D	Three Dimensional

CHAPTER 1

INTRODUCTION

1.1 General Information

Missiles are rocket-propelled weapons which are designed to deliver highly explosive warheads with great accuracy towards targets at high speeds. Since their first production and development process missiles have become the most effective and lethal threats against military or civil platforms including all kinds of naval, airborne and ground targets. [2]

Missiles can be classified in different categories with respect to their orientation towards target, operational range, purpose, and seeker type. According to their orientation towards targets, missiles are either unguided (rocket) or guided (homing missile). For a guided missile, there is a seeker system, which measures the target position or takes information about target and the guided missile turns towards it by means of a guidance algorithm and damages the target. Operational range is also a crucial parameter for missile design. Propulsion system sustains the thrust for missiles to move towards targets. Depending on the propulsion sustaining time, operational range of missiles are adjustable. Tactical missiles are suitable for short/medium range; however strategic missiles like ballistic missiles are suitable for long range operations such as intercontinental targets. [3], [4]

With respect to their purpose, missiles can be classified in five subcategorizes which are;

- Surface-to-Air,
- Surface-to-Surface,
- Air-to-Surface,
- Air-to-Air,
- Anti-Satellite. [3], [2]

A surface-to-air missile is launched from the ground and destroy an air platform. These type of missiles are named as anti-aircraft systems as well. For instance, MANPADs are surface-to-air missiles and they are launched from shoulders of a human operator. Main purpose of a surface-to-surface missile is to be launched from ground or sea and destroy targets on land or at sea. Anti-tank and ballistic missiles are the basic examples of surface-to-surface missiles. Air-to-surface missiles are launched from aircraft to destroy targets on land or at sea, for instance cruise missiles and anti-tank missiles. An air-to-air missile is launched from an air platform

to protect itself or destroy another aircraft. The last, an anti-satellite missile is designed to destroy a satellite.

Guided missiles can also be classified with respect to its seeker type. A seeker tracks a target with an antenna which receives energy radiated or reflected from a target. The main seeker types are laser, radar and infrared [5]. After IR technology is developed, this technology has been started to use at missile seekers and advanced detector technologies have been applied for new missile designs as well. In 1958, USA produced Redeye IR missile which had an IR detector [6]. After this important development of missile technology, IR missiles have been the biggest threat for airborne vehicles. In the last decades, approximately seventy percent of military aircraft and helicopters losses have been caused by IR guided missiles. Nowadays, the number of IR missiles exceed 500.000 all over the world. The reasons of this is that IR missiles are cheap and have great probability of kill [7], [8].

Other reasons of why the IR missiles are the most popular threats are that IR missiles are passive homing missile systems and cannot be easily detected by MWS ES systems. On the contrary to the semi-active homing missiles, a passive homing system only senses the target radiation and does not need any other information from off-board systems and does not transmit any signal for the purpose of measuring target position. Semi-active homing missile needs information from off-board systems such as radar systems, launcher and illuminator about target and in some cases, its own position to track targets. An active homing missile transmits signal and receive reflected signal by target and measures the target's position. As a result, passive and active homing missile systems are called fire-and-forget missiles. [5]

To deceive a missile, target uses some techniques which are called as ECM techniques. ECM techniques for IR guided threats are divided into two categories. These are pre-launch and post-launch ECM techniques. The main pre-launch ECM are Infrared Signature Suppression, evasive maneuver etc. Infrared Signature Suppression is used to diminish IR radiation. Post-launch ECM can be classified into two subcategories. These are passive and active ECM techniques. Passive ECM techniques are dispensing decoy or flare which radiates heat higher than targets and missile supposed to lock it on. Active ECM techniques are IRCM Jammer and directed IRCM. IRCM Jammer generates modulated signals to deceive the missile seeker. Directed IRCM is a hard-kill technique which transmits higher energy towards missile seeker so as to harm or dazzle the seeker of a missile. [7], [9]

All the techniques that are used to prevent missiles to be deceived by ECM techniques are called ECCM techniques. The basic aim of ECCM techniques is to decrease efficiency of ECM techniques over missile seekers. The main ECCM techniques are related to target movement and IR radiation characteristics. Thanks to target motions and IR radiation information, missile can differentiate the objects on scene either as ECM technique or as a real target. The focus of this study is on generating effective ECCM techniques for missiles to prevent them locking on ECM ammunitions and losing the track of the target.

A typical IR guided missile seeker subparts are shown in Figure 1.1. IR scene radiation is collected at the E/O block at the dome of the missile. Dome has two important roles; these are protecting missile seeker and collecting IR energy which is radiated from target or other objects in the FOV of seeker on scene, over the E/O block. Collected IR signal is directed to the IR detector by the mirrors or object lenses which are in the E/O block. IR detector converts this energy to electrical energy (voltage) due to the spectral responsivity characteristics of the detector. Processor is the core of the seeker which measures or/and calculates attributes of

objects on the detector. At the same time, all ECCM techniques are developed and applied at this processor. The reason of modeling the gimbal is that, FOV of seeker which is about 2^o - 3^o is too narrow. Gimbal has wide angular limits such as $\pm 45^o$. Owing to this, the seeker can rotate up to gimbal's angular limit. Gimbal has two perpendicular and independent axes which are azimuth and elevation axes. Gimbal is driven by two servo-motors for both of the axes. The limiting angles of servo motors are determined by the gimbals' FOR angle [2].

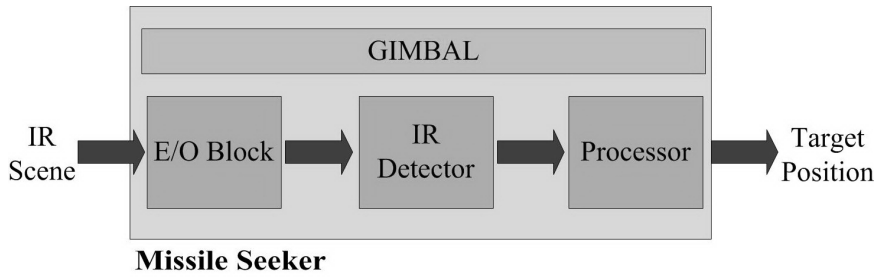

Figure 1.1: Subparts of IR Guided Missile Seeker

In this study, a simulator is designed to realize and test some artificial scenarios. Simulator contains atmospheric effects over radiation models, missile model, target and ECM techniques. The atmospheric effect model is based on spectral air transmittance. At the same time; path radiance, which contains emitting radiation of particles along the path in missile LOS, and sky radiance, which is the radiation of background without any objects and source except air, are used to model high fidelity atmospheric effects. All these atmospheric effects are calculated by MODTRAN. The modeled IR guided missile is shoulder-launched surface-to-air missile. This missile has a gimbal having two perpendicular axes with $\pm 60^o$ angular limits. This gimbaled missile has not only imaging infrared (IIR) seeker but also a guidance block which helps the missile to turn towards a target. Target model is a 6-DOF nonlinear dynamic model of F-16 aircraft. This target model contains not only the dynamic model but also a 3D IR signature with different temperature zones. In order to deceive and break the track gate of the missile, target can make evasive maneuvers and uses ECM techniques. Among the ECM techniques, MTV and spectral flares are dispensed at specified time sequences by the target. Not only MTV but also spectral flares radiate more energy than the target. However, spectral flare IR signature matches with IR signature of the target. If the missile seeker has not the ability to distinguish flare and target, missile locks on the flare on the scene because of more radiation. To equip the missile with this ability, ECCM techniques are developed. By these techniques, missile can discriminate and identify objects on scene and generates position information to the guidance block. Among the ECCM techniques, denomination, track gate, sector strengthening, area, kinematic and dual band ratio information of objects are used. These are compared with the history of the tracked object and a matching is sought. After that, identification block identifies these matched objects either as target or flare. Next, the position information of the target is given to guidance block. Finally, thanks to kinematic motion blocks, missile moves towards target and damage it by its highly explosive warhead and fuze which detonates a warhead. The flow chart and subparts of modeled simulator is shown by Figure 1.2.

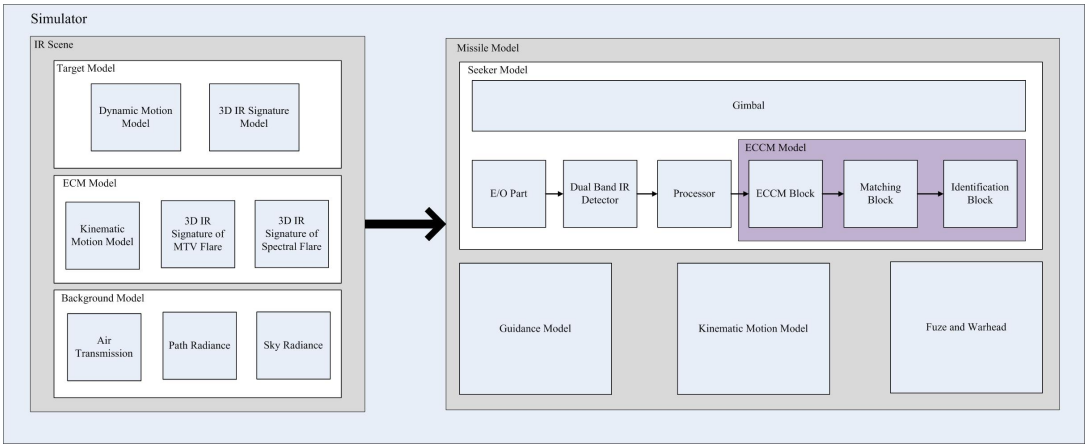

Figure 1.2: The Flow Chart and Subparts of Modeled Simulator

1.2 Infrared Fundamentals

Composing atoms of objects are continuously vibrating, vibration of atoms are directly proportional with energy level of atoms. The average kinetic energy of the vibrating atom particles is determined by the absolute temperature of objects. The electrodynamic laws indicate that a moving electric charge is related with a variable electric field that produces an alternating magnetic field. Fundamentally, this interaction produces an electromagnetic wave that radiates energy from the body of object at the speed of light. In a word, all objects with an absolute temperature over $0\ K$ emit IR radiance. IR radiation of objects is a function of surface temperature and surface physical properties of objects. For instance, hotter objects emit higher radiation than cooler objects. At the same time, peak value of radiation of hotter objects occurs at a shorter band of the IR spectrum. Smooth surface objects emit less radiation than rough surface objects. The following subsection will explain IR electromagnetic spectrum and basic IR theory including formulas of calculation of IR radiance with respect to material properties. [9], [10]

1.2.1 IR Spectrum

IR radiation is electromagnetic waves in the wavelength spectrum range from ultraviolet to microwaves at electromagnetic spectrum. Because of atmospheric effects over emitted IR radiation, IR spectrum has divided into five spectral subbands as depicted in Figure 1.3 [11]. These bands are;

- Near Infrared (NIR),
- Short-wave Infrared (SWIR),
- Mid-wave Infrared (MWIR),
- Long-wave Infrared (LWIR),

- Very Long-wave Infrared (VLWIR) [12].

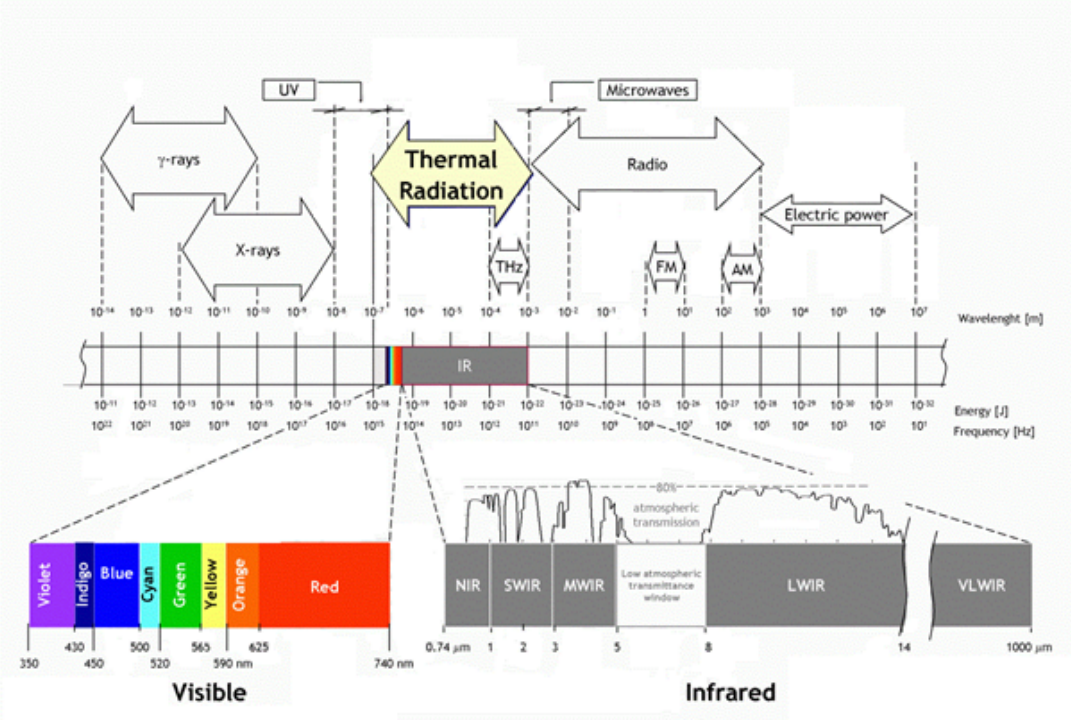

Figure 1.3: Infrared Spectrum

Table 1.1: IR Spectral Band and Dominant Radiation

Spectral Band Designation	Wavelength Range (μm)	Dominant Radiation
UV	0.2 - 0.35	Reflective
Visible	0.35 - 0.74	Reflective
NIR	0.74 - 1	Reflective
SWIR	1 - 3	Reflective
MWIR	3 - 5	Reflective & Emissive
LWIR	8 - 14	Emissive
VLWIR	14 - 1000	Emissive

Spectral band's nominal wavelength range and dominant radiation terms are shown at Table 1.1 [12]. However, nominal wavelength ranges of these spectral bands differ from one reference to another. Because of sun light, reflective radiation is effective at UV, visible, NIR and SWIR bands. For high fidelity modeling, if there is a sensor or detector whose spectral response is peak at these spectral bands, the model must contain reflectivity modeling. Similarly, spectral response of detector is maximal at MWIR spectral range, not only reflectivity but also emissive radiation terms must be modeled. However, for long wave bands, sun lights effect is diminished and emissive radiation model is adequate for high fidelity modeling [13].

1.2.1.1 Criterion of Infrared Band Choice

To design a new IR guided missile seeker, one of the foremost important steps is spectral response of the decided detector. For IIR, generally detector whose spectral response are MWIR or/and LWIR spectral bands are chosen. The main reason for chosen these that, emissive radiation of heat objects are dominant radiation rather than reflective radiation over total radiation sensed by detector [2]. At the same time, basic threats for missile are airborne vehicles whose surface temperature is range from $300\ K$ to $1000\ K$. Peak point of these surface temperatures occur at LWIR and MWIR at IR spectrum. For these reasons, LWIR and MWIR bands are chosen for effective IIR seeker design [9].

Performance of MWIR and LWIR spectral bands differ in respect of some factors. These factors are sensitivity, contrast, air condition, atmospheric effects and background noise. Choosing MWIR band for detector design provides some advantages. MWIR band is more useful for hotter objects than LWIR band. Smaller diameter of optic is enough to sustain a certain resolution. Moreover, MWIR provides higher temporal contrast, better clear-weather performance and better performance at higher humidity. However, LWIR band has also some advantages. These are better performance at foggy, dust and winter haze air conditions, better air transmission, less sun light reflective effect and adaptation aircraft surface temperature. However, to separate background from target, high SNR in LWIR spectral range is not convincing because the background photon fluxes are almost higher to the same extent with target. [13]

In the light of all these performance comparing between MWIR and LWIR, the modeled missile seeker has dual-band detector whose spectral band intervals are MWIR and LWIR.

1.2.1.2 Plank's Law for Blackbody Radiation

Perfect emitter blackbody object absorbs all radiant energy which falls on it, and radiates electromagnetic energy at all frequencies. Blackbody object's emitted radiance energy is calculated with Plank's Law which defines the spectral distribution of emitted energy from blackbody objects [9]. The formula of Plank's Law is shown at equation 1.1 [12].

$$M(\lambda,T) = \frac{3.7418\ 10^4}{\lambda^5(e^{\frac{14388}{\lambda T}}-1)} \qquad \frac{W}{\mu m\ cm^2} \tag{1.1}$$

Where, $M(\lambda,T)$ indicates spectral exitance of blackbody object, T is surface temperature (Kelvin) and λ is spectral band (μm). If the surface of object is isotropic, which is often called Lambertian surface, the relationship between exitance and radiance terms is shown at the equation 1.2. Radiance equation is updated by inserting equation 1.2 into equation 1.1. As a result, equation 1.3 is obtained where, $L(\lambda,T)$ indicates spectral radiance of blackbody. [12]

$$M = \pi L \tag{1.2}$$

$$L(\lambda,T) = \frac{1}{\pi}\frac{3.7418\ 10^4}{\lambda^5(e^{\frac{14388}{\lambda T}}-1)} \qquad \frac{W}{sr\ \mu m\ cm^2} \tag{1.3}$$

1.2.1.3 Effect of Object Physical Properties over Radiation

Radiation from a source of light such as sun light, when incident on object surface, is reflected by the surface, transmitted into the surface or absorbed into the surface. Sum of absorbed, reflected and transmitted power is identical to incident power as shown in equations 1.4, 1.5, 1.6, and 1.7. Where, P_α is absorbed power, P_τ is transmitted power, P_ρ is reflected power and P_i is incident power. To determine physical properties of objects, ratio of quantities of absorbed, reflected and transmitted power with incident power gives absorption (α), reflectivity (ρ) and transmission (τ) spectral coefficients. [9], [14]

$$\alpha = \frac{P_\alpha}{P_i} \tag{1.4}$$

$$\tau = \frac{P_\tau}{P_i} \tag{1.5}$$

$$\rho = \frac{P_\rho}{P_i} \tag{1.6}$$

$$P_i = P_\alpha + P_\tau + P_\rho \tag{1.7}$$

$$1 = \alpha + \tau + \rho \tag{1.8}$$

The sum of absorption, reflectivity and transmission coefficients must be equal to one (equation 1.8). However, for opaque objects, there is no transmission ($\tau = 0$). Thus, reflectivity and absorbance coefficients summation is identical to 1 for opaque objects as shown equation 1.9. At the same time, for IR spectrum, there is a dominant radiant source is absorbance while reflectivity coefficient is much smaller than absorbance coefficient. There is an assumption in this study that, object is neither gaining nor loosing heat. Thus, absorbance coefficient is identical to emissivity (ϵ) coefficient (equation 1.10). [9]

$$\alpha + \rho = 1 \qquad (\tau = 0) \tag{1.9}$$

$$\alpha = \epsilon \tag{1.10}$$

As mentioned before, coefficients of emissivity, transmission and reflectivity are dependent on wavelength and are indicated with $\epsilon(\lambda)$, $\tau(\lambda)$ and $\rho(\lambda)$ symbols. For example, coefficient of emissivity can be classified in three groups. First, blackbody object is a perfect emitter and its emissivity coefficient is identical to 1. Gray body object has constant value less than 1 for throughout IR spectrum and selective radiator takes different values at different wavelengths. However, there is an assumption in this study that, spectral coefficients of materials do not depend on wavelength and fixed throughout the IR spectrum. [9], [12]

To calculate emitted radiation from the viewpoint of missile seeker, atmospheric effects which depends on range between aircraft and missile, altitude, weather condition, geographic conditions etc. and emissivity coefficient of object seen by missile seeker must be included in Plank Equation as shown equation 1.11.

$$L(\lambda, T) = \frac{1}{\pi} \frac{\epsilon(\lambda)\ \zeta_{atm}(\lambda)\ 3.7418\ 10^4}{\lambda^5 (e^{\frac{14388}{\lambda T}} - 1)} \qquad \frac{W}{sr\ \mu m\ cm^2} \tag{1.11}$$

Where, $\epsilon(\lambda)$ is spectral emissivity coefficient and $\zeta_{atm}(\lambda)$ indicates atmospheric transmission.

1.2.1.4 Wien's Displacement Law

Wien's Displacement Law is defined as the wavelength of the maximum emission of blackbody source is inversely proportional with its surface temperature as shown in Figure 1.4. As the temperature rises, the maximum (peak) of the radiant energy shifts toward the shorter wavelengths. Wien Law is shown at equation 1.12, where, λ_{max} is the maximum wavelength in μm, T is absolute surface temperature in Kelvin [12].

$$\lambda_{\text{max}} = \frac{2897.756}{T} \tag{1.12}$$

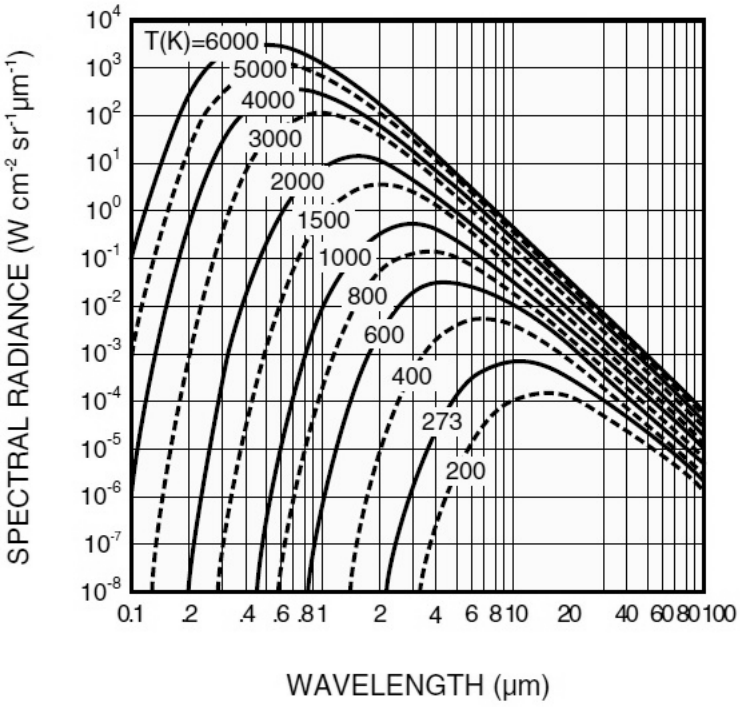

Figure 1.4: Wien's Displacement Law

1.3 Original Contributions of the Thesis

Based on this study, a surface-to-air missile is modeled which contains an IIR seeker equipped with a tracking based ECCM technique. In literature, there are very few IR missile model studies which contain ECCM techniques. In this study, our proposed model of IIR missile has a combination of six ECCM techniques. Moreover, IIR seeker missile technology is still developing among surface-to-air missiles. In general, IIR guided missiles are anti-ship missiles which are launched from air or surface to surface. Our proposed missile is a surface-to-air missile. Herewith, this study presents about new proposed works. The last but not least, the atmospheric effects are incorporated into the artificial scenarios with respect to air conditions, target and missile positions. In the light of these proposed improvements, this study has its own originality among other proposed IR seeker works and may guide new studies.

Three articles relevant with this study are published in SIU 2013 Congress, USMOS 2013 and TOK 2013 Conferences. The additional information about these articles can be obtained by referring them as;

- Rağıp Yurttaş, Kemal Leblebicioğlu, Isı Fişeklerinin Görüntülemeli Kızılötesi Arama Başlıklarına Karşı Etkinliği, SIU 2013, Girne, KKTC.
- Rağıp Yurttaş, Kemal Leblebicioğlu, Isı Fişeklerinin Görüntülemeli Kızılötesi Arama Başlıklarına Karşı Etkinlik Analizi Amacıyla Geliştirilen Benzetim Yazılımı, USMOS 2013, ODTÜ, Ankara.
- Rağıp Yurttaş, Kemal Leblebicioğlu, Görüntülemeli Kızılötesi Arama Başlıklı Güdümlü Mermilere Karşı Etkin Elektronik Taarruz Uygulamaları, TOK 2013, Malatya.

In addition to the afformentioned works, a journal publication is being prepared.

1.4 Thesis Outline

Chapter 2 describes IIR seeker missile model comprising dual band detector, processor, advanced ECCM techniques and gimbal model. In this chapter, literature review about IR missile seeker types and their progress in time, reticle material and IR detector technology are also detailed.

Chapter 3 describes missile guidance law and a point mass kinematic mathematical motion model so as to evaluate missile seeker performance. 6-DOF equations of motion are also derived and obtained in this chapter.

Chapter 4 describes the 6-DOF non-linear dynamic mathematical motion model of an F-16 aircraft and 3D IR signature model of the F-16 aircraft with twenty different temperature zones.

Chapter 5 describes not only IR ECM models which contain time dependent IR signature model and kinematic motion model of spectral and MTV flares but also CMDS model which contains flare dispensing time, dispenser selection and dispensed flare selection models. In this chapter, literature information about pre-launch and after-launch ECM techniques, flare types and performance criteria of flare and CMDS are also explained in detail as well.

Chapter 6 describes simulation results to evaluate the performance of the proposed missile seeker. Also, the 3D trajectories of the missile and aircraft, miss distance and flight time information are given to compare performances based on different input parameters.

Chapter 7 describes results of artificial scenarios and conclusions of this study. Contributions of this study and recommendations for future works are also explained.

CHAPTER 2

IR SEEKER DESIGN

2.1 Introduction

IR guided missiles have seeker system which collects and detects radiated IR energy from target or other sources in FOV of seeker on scene. The main mission of missile seeker is to view the scene and output the detected target position to guidance block. [10]

IR seeker comprises of electro-optics, gimbal, reticle (if necessary), detector, and processor parts. E/O collects IR energy from scene and directs this energy over IR detector through reticle. E/O has dome, mirrors or contact lenses. The dome not only collects IR energy but also protect missile seeker. Most IR missiles use the hemispherical dome. Because hemispherical shape of dome does not change the path of the incoming light rays. These light rays are directed over IR detector by optics that may be mirrors or contact lenses. [10], [15]

IR seeker has mounted on nose of the missile where it can have an unobstructed view ahead as shown Figure 2.1. At the same time, optical part of seeker is usually mounted on gimbal which rotates about $\pm 45^o$ - $\pm 60^o$ in both azimuth and elevation relative to the missile centerline so as to hold target on boresight direction of seeker. To provide the greatest possibility of collecting IR radiation from the target, the IR seeker must have wider FOV. However; seeker FOV is too narrow about 2^o - 3^o, gimbal is necessary to enhance the missile seeker FOV. [2], [15]

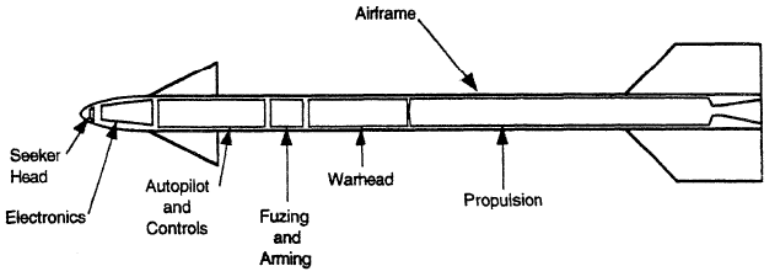

Figure 2.1: Subparts of IR Guided Missile

Reticle of IR seeker modulates incoming light rays with respect to target position. There are several types of reticle patterns design to measure target position with high accuracy. The basic reticle patterns are *rising sun* pattern and *wagon wheel* pattern shown at Figure 2.2

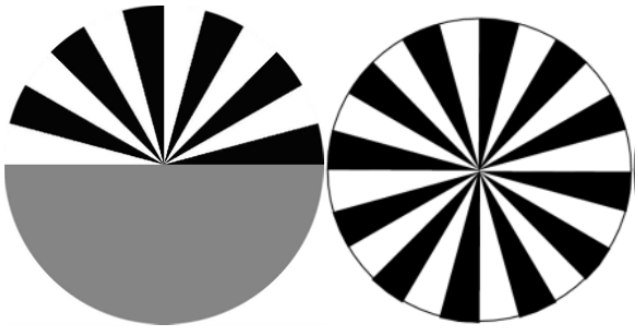

Figure 2.2: *Rising Sun* and *Wagon Wheel* Pattern

2.1.1 IR Detector

IR detectors convert IR energy to voltage level with its spectral responsivity characteristics. As mention Section 1.2.1.1, selection of infrared response of IR detector is the foremost important step to model new design IR seeker. There are some reasons which affect this selection. These are;

- Performance criterion of selected spectral response,
- Performance of detector such as photo sensitivity, NEP, detectability (as shown Figure 2.3), contrast,
- Atmospheric transmission windows where absorption by H_2O, CO_2 etc.,
- Target surface temperature or radiation characteristics and
- Selected detector type such as thermal and quantum. [13]

IR detectors are classified into thermal and quantum types. Thermal detectors, which do not require cooling system, use the infrared energy as heat and their photo sensitivity is independent of wavelength. However, their response time is slower and detection capability is lower than quantum type detectors. Although, quantum type detectors offer higher detection performance, they require cooling system so as to accurate measurement except for detector used in the near infrared region. Types of IR detectors are shown in Figure 2.4. [16]

In the light of constraints, $1-3\ \mu m$ band was used by early IR seekers (first generation IR seeker), which has not cooling system. The $3-5\ \mu m$ band is the most applicable to current cooled IR seekers. $8-12\ \mu m$ band is also most applicable for imaging IR detectors [17], [9]. Detector materials of early and today's technology IR seeker is listed at Table 2.1. [10]

2.1.2 IR Seeker Types

Improvement at ECM techniques such as advanced flares and IRCM jammers, reveals the idea of development of new IR missile seekers. Through the years, advanced technologies at IR

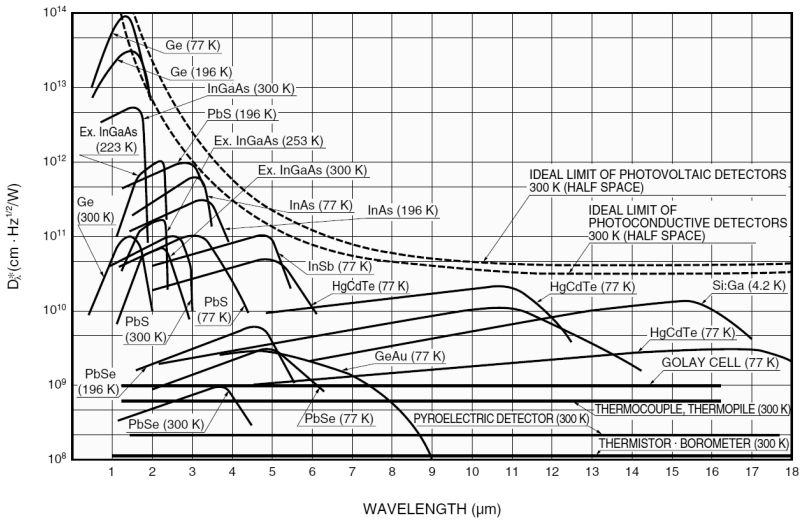

Figure 2.3: Performance of Detector Materials

Type			Detector	Spectral response (μm)	Operating temperature (K)	D*(cm · Hz^1/2 / W)
Thermal type	Thermocouple · Thermopile Bolometer Pneumatic cell Pyroelectric detector		 Golay cell, condenser-microphone PZT, TGS, $LiTaO^3$	Depends on window material	300 300 300 300	D^* (λ,10,1) = 6×10^8 D^* (λ,10,1) = 1×10^8 D^* (λ,10,1) = 1×10^9 D^* (λ,10,1) = 2×10^8
Quantum type	Intrinsic type	Photoconductive type	PbS PbSe InSb HgCdTe	1 to 3.6 1.5 to 5.8 2 to 6 2 to 16	300 300 213 77	D^* (500,600,1) = 1×10^9 D^* (500,600,1) = 1×10^8 D^* (500,1200,1) = 2×10^9 D^* (500,1000,1) = 2×10^{10}
		Photovoltaic type	Ge InGaAs Ex. InGaAs InAs InSb HgCdTe	0.8 to 1.8 0.7 to 1.7 1.2 to 2.55 1 to 3.1 1 to 5.5 2 to 16	300 300 253 77 77 77	D^* (λp) = 1×10^{11} D^* (λp) = 5×10^{12} D^* (λp) = 2×10^{11} D^* (500,1200,1) = 1×10^{10} D^* (500,1200,1) = 2×10^{10} D^* (500,1000,1) = 1×10^{10}
	Extrinsic type		Ge : Au Ge : Hg Ge : Cu Ge : Zn Si : Ga Si : As	1 to 10 2 to 14 2 to 30 2 to 40 1 to 17 1 to 23	77 4.2 4.2 4.2 4.2 4.2	D^* (500,900,1) = 1×10^{11} D^* (500,900,1) = 8×10^9 D^* (500,900,1) = 5×10^9 D^* (500,900,1) = 5×10^9 D^* (500,900,1) = 5×10^9 D^* (500,900,1) = 5×10^9

Figure 2.4: Types of IR Detector

Table 2.1: IR Detector Materials

IR Detector Materials	Cooled (μm)	Band Interval (μm)
Lead Sulphide (PbS)	No	1.5 - 2.5
Lead Sulphide (PbS)	Yes	2 - 4
Lead Selenide (PbSe)	No	2 - 4.2
Lead Selenide (PbSe)	Yes	3 - 5
Indium Antimonide (InSb)	Yes	2 - 5
Mercury-Cadmium-Telluride $(Hg_{1-x}Cd_xTe)$	Yes	8 - 13

detectors have resulted in new design IR seeker as well. As a consequence of these, new IR seeker has been developed during 1950s.

IR missiles can be categorized as four generations with respect to their seeker types. These are spin scan seekers (first generation), con-scan seekers (second generation), pseudo-imaging seekers (third generation), and imaging seekers (fourth generation). [17]

Since first generation spin scan IR seeker has been developed, IR seeker evaluation has been proceeded until today as shown at Figure 2.5. At the following section, all these generations will be explained in detail respectively.

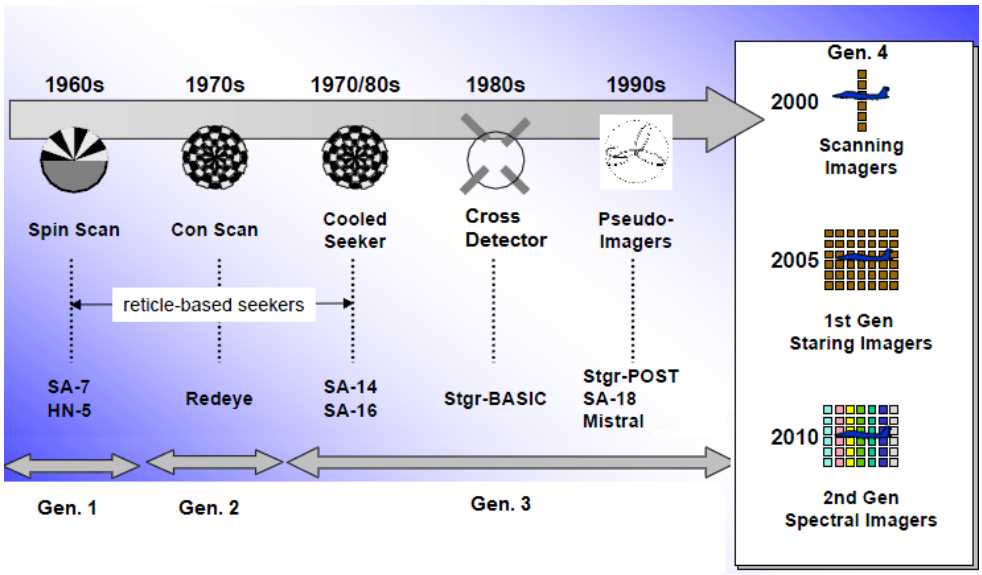

Figure 2.5: IR Seeker Types

2.1.2.1 Spin Scan Seekers

First generation spin scan seeker has spinning reticle which rotates constant frequency so as to generate modulated signal over detector as shown Figure 2.6 [9], [1]. The popular reticle for spin scan seekers is *rising sun* reticle as shown left side of Figure 2.2. The *rising sun* reticle is a thin plate of optical material has opaque, transparent and semi-transparent patterns on it. Grey pattern of reticle is semi-transparent, black and white patterns are opaque and transparent respectively. As the reticle is rotated, the IR energy is modulated by reticle patterns. Modulated IR signal is converted electrical signal at uncooled PbS detector whose spectral response is in NIR band (Table 2.1). Modulated electrical signal is processed at processor and angular positions (azimuth, elevation angles) of target are measured.[17]

Because of its reticle pattern, spin scan seeker generates AM output signal. This type seekers lock on the hottest object (on hot engine tailpipe or afterburner of aircraft) on scene after processor demodulates that signal. Flares such as conventional flares and spectral etc., which radiates higher than target may be effective ECM techniques so as to break a lock of missile seeker [18]. At the same time, when target is boresight of seeker, error signal is generated. To

prevent from this problem, first generation IR missiles move undulating path. [10]

Examples of first generation IR seeker are FIM-43 Redeye [1], [18], SA-7 [18], HN-5 [8].

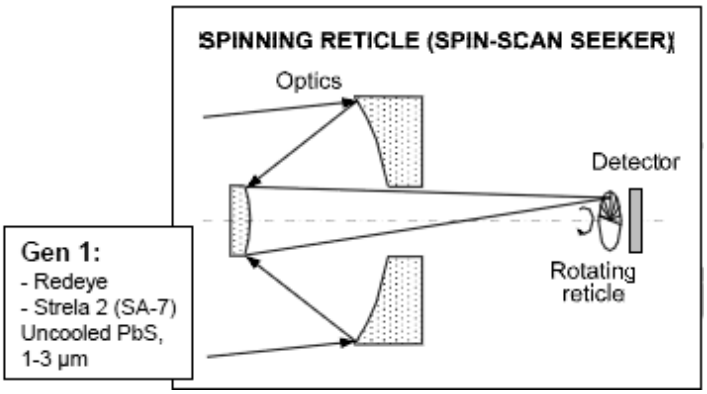

Figure 2.6: Spin Scan Seekers [1]

2.1.2.2 Con-Scan Seekers

Constraints of spin scan seekers reveal a demand about new generation seeker which is con-scan seekers as shown Figure 2.7. This type seeker has fixed reticle. However, nutating secondary mirror generates scene on *wagon wheel* reticle as shown right side of Figure 2.2. This reticle modulates IR signal over detector. Con-scan seeker has cooled InSb detector whose spectral response is in MWIR band (Table 2.1). Operating at longer wavelengths allowed cooler parts of the engine, hot parts of the airframe, flare rejection and the cooler CO_2 emissions in the exhaust plume to be detected, thus allowing wider angles of engagement (head on attack) [9], [18]. However, advanced flares and IRCM Jammer which jams the modulated FM signal may be effective ECM techniques for con-scan seekers IR missiles.

When the target is centered in the seeker scan, the detector generates a pulsed output similar to that of the spin scan seeker. However as the target maneuver or move, the signal output of the InSb detector is a FM signal. The frequency of the modulated signal is directly proportional to the amount of target displacement from the boresight of the seeker. Thus, the lack of error response when the target is near the center of the seeker FOV at spin scan seeker is removed at con-scan seeker.[10]

Stinger Basic, FN-6, SA-14, SA-16, AA-8, AIM-9L, SA-13 (IR mode), AA-7, AA-10, and AIM-9M are some examples of con-scan seeker IR guided missiles [1], [17], [18].

2.1.2.3 Pseudo-Imaging Seekers

In the light of seeking better methods for discriminating ECM techniques, pseudo-imaging seekers are developed. This type seeker is the first seeker without reticle optical materials. Instead of reticle, there are two mirrors or prisms at rosette scan which is the basic pattern of

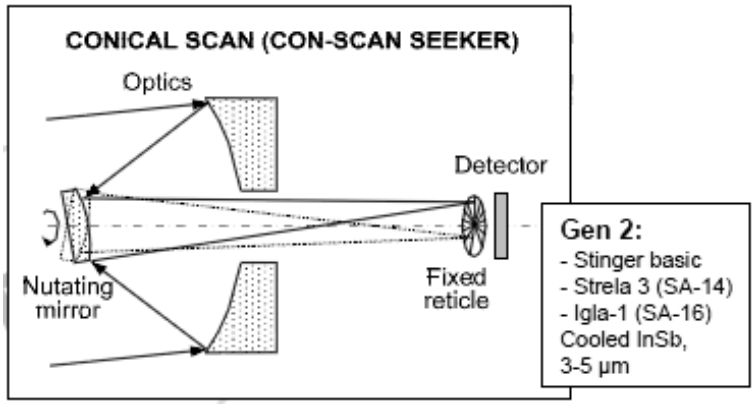

Figure 2.7: Con-Scan Seekers [1]

pseudo-imagers as shown Figure 2.8. For rosette pattern generation, there are two counter-rotated mirrors or prisms which has different rotation frequencies. Tracking is established with one or more detectors which have IFOV as a small part of scene seen by missile seeker (total FOV). Detector scans total FOV due to optical mirrors or prisms and generates signals. These signals represent the instantaneous position of detector within the total FOV. Then processor measures the exact position of target. [19]

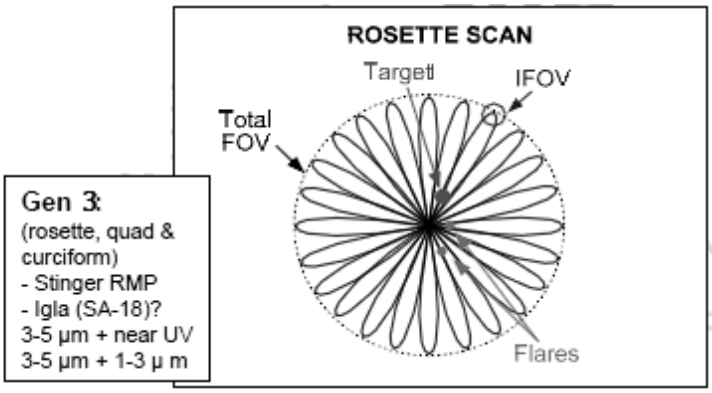

Figure 2.8: Pseudo-Imaging Seekers [1]

So as to enhance the performance, advanced pseudo-imagers are developed in 80's/90's. Advanced pseudo-imaging seekers may include dual detector whose spectral response near UV/MWIR or MWIR/SWIR bands as shown Figure 2.8. Penguin, Stinger RMP, SA-18, Mistral, AA-11, and Magic 2 are the examples of IR missiles with pseudo-imaging seeker. [17], [1]

2.1.2.4 Imaging Seekers

The fourth and the last generated seeker type is imaging seekers (Figure 2.9) having detector array which produce image of target in FOV of seeker instead of reticle based modulated sig-

nal generation. Because of more information having about scene thanks to produced image, imaging seeker can discriminate background, ECM techniques such as flare, IRCM Jammer etc. Despite more robust and effective seeker system against ECM techniques, imaging seekers are very expensive systems. Image size and power consumption are also critical problems which affect performance of missile seeker. [9],[20]

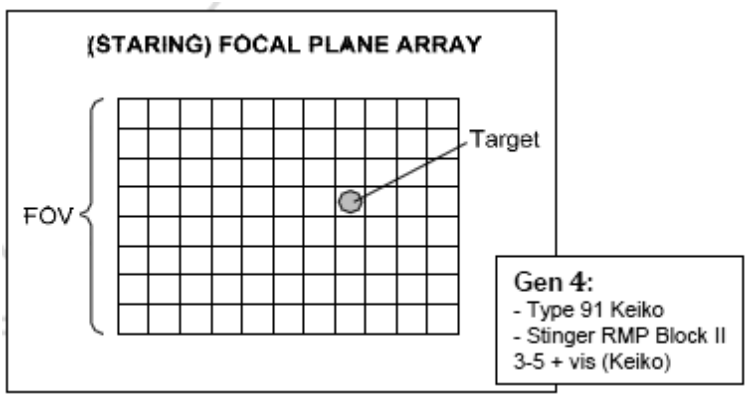

Figure 2.9: Imaging Seekers [1]

Imaging detectors create image from scene into two ways. These are scanning and staring (FPA) detectors. Scanning detector array images only a portion of the FOV and scans this IFOV about to cover the total FOV and generates image data a relatively small number of detectors as shown Figure 2.10. Systems that image the total FOV on the FPA operate in a staring mode (Figure 2.11) which focuses the entire scene optically on a two-dimensional array and samples each element electronically by using a raster scan to produce scene images.

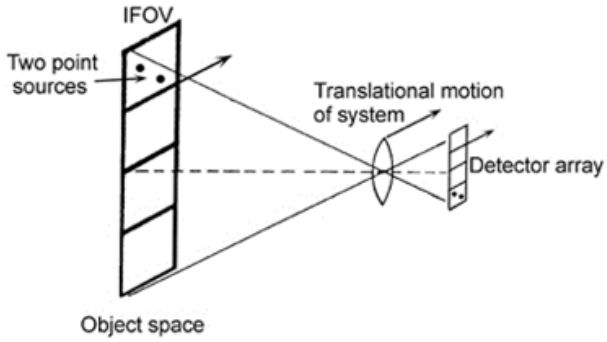

Figure 2.10: Scanning Imaging IR Seeker

On the purpose of enhancing the performance of resistance to decoy and other ECM techniques, more accurate systems have been developing since 2000's as shown Figure 2.5 [18]. These systems may have dual band (multi-color) detector and/or advanced ECCM techniques such as kinematic, spectral, spatial and intensity level. Dual band (spectral imaging) seekers with multiple cooled detectors have been already produced [17]. However, dual band seekers

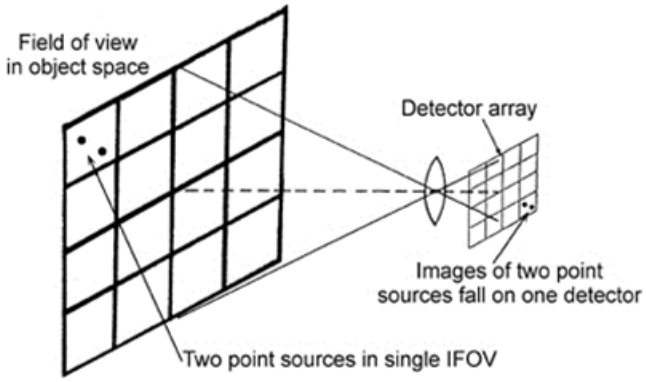

Figure 2.11: Staring Imaging IR Seeker

only with one detector with arrange their spectral responses are almost developed. Dual band detector operates in MWIR, MWIR/UV, MWIR/SWIR, or MWIR/LWIR bands [17], [9].

The basic examples of imaging seekers are AGM-65F/G (Maverick), Walleye, Keiko (Toshiba Type 9/Kin), NSM (Naval Strike Missile) and Stinger RMP Block II. [17], [1].

2.2 IR Seeker Model

IR seekers are classified into four categories as declared above. In this study, gimbaled imaging IR seeker is modeled. Modeled imaging seeker has advanced dual band (spectral imaging) detector technology. Spectral responses of these detectors are MWIR and LWIR bands. In addition, modeled IR seeker has advanced ECCM techniques. Denomination, track gate, sector strengthening, area, kinematic and dual band ratio ECCM techniques are modeled within this study. Modeled gimbal has two perpendicular azimuth and elevation axes with angular limit $\pm 60^o$.

Because of comprehending the IR seeker model of guided IR missile, IR sources seen by seeker on IR scene, atmospheric effect, dual band detector, processor, ECCM techniques and gimbal model are explained in detail at the following sections respectively.

2.2.1 IR Sources

Imaging IR surface-to-air missiles are launched from ground so as to destroy air targets. Air targets are the main IR sources from viewpoint of surface-to-air missile seeker. For military applications, air targets may be helicopters, aircrafts, fast jets, transport aircrafts etc. ECM ammunitions, which are dispensed for deceiving seeker, are IR sources for IR seeker as well. These sources are man-made sources. At the same time, there are natural IR sources such as sun, moon, cloud, sky light and starlight and atmospheric effects etc. To satisfy high fidelity modeling conditions, all these sources ought to be included in simulator which evaluates the performance of modeled IR seeker. [9]

In this study, 3D F-16 aircraft target model, spectral and MTV flare are modeled in high detail level. The models of target and ECM will be explained in detail at Chapter 4 and Chapter 5 respectively. In addition to these, atmospheric effects are added to scene modeling. Atmospheric transmission, path radiance and sky radiance are the components of atmospheric effects. All artificial scenarios are assumed to be realized at day light. Thus, atmospheric effect model includes sky light effects and ignores moon effects. However sun, cloud and starlight IR signatures are not modeled in this study. Because of the fact that, the main purpose of this work is to measure and interpret the performance of imaging IR seeker equipped with ECCM techniques against ECM techniques such as flare and evasive maneuver. So as to realize this purpose; only target, ECM and atmospheric effect models are sufficient. Atmospheric effect model is detailed in the following section.

2.2.2 Modeling of Atmosphere Effect

Atmospheric effects over radiation of sources are critical performance criteria. In this study, the atmospheric effect model contains air transmittance with respect to spectral band, path radiance, which contains emitting radiation of particles along the path in missile LOS between missile and source, and sky radiance, which is radiation of background without any objects and source except day light and air. There are too many atmospheric effect calculation codes in the literature. LOWTRAN, MODTRAN, HITRAN and FASCODE are the popular atmospheric effect calculation codes. Within this study, all these atmospheric effects are calculated by MODTRAN. For more information about MODTRAN, references [21], [22] are sufficient sources to understand the usage of program and how to calculate these effects.

Atmospheric effects are dependent on weather conditions (rainy, sunny, cloudy and foggy etc.), date and season of year, hour of day, latitude, longitude and altitude information of terrain as listed Table 2.2. Within this study, 3 type atmosphere conditions are used for atmospheric effect calculations. These are good, typical and rainy conditions. Input parameters of MODTRAN with respect to selected air condition are given at Table 2.2 as well. In addition to these, missile source engagement is important parameter which alters atmospheric effect. Range between missile and source, altitude from sea-level of missile and source (target and ECM ammunitions) information are also scenario dependent input parameters of MODTRAN. At the same time, for each simulation step, these 3 parameters are updated and in the light of these new input parameters, new atmospheric effects are calculated. Output of MODTRAN is spectral air transmission, spectral path radiance and spectral sky-radiance.

Spectral air transmission is percentage of transmitted IR radiation by atmosphere. Figure 2.12 demonstrates an example which missile altitude is 2250 meters, target altitude 2750 meters and range between them is 500 meters. Good weather condition transmits almost all radiation. However, rainy weather condition absorbs half of radiated energy from source.

Spectral sky-radiance example is shown at Figure 2.13 with respect to altitude in km for good weather conditions. As in seen from figure, altitude and sky-radiance are inversely proportional.

Within this study, atmospheric effects are inserted in simulator. Spectral atmospheric transmission ($\zeta_{atm}(\lambda)$) effect is inserted at gray body Plank's Law radiation calculation of sources as shown equation 1.11.

Table 2.2: MODTRAN Input Parameters for Calculation Atmospheric Effects

Atmospheric Information	Good	Typical	Rainy
Model Atmosphere	1976 USA	1976 USA	1976 USA
Type of Atmospheric Path	Slant path	Slant path	Slant path
Aerosol Model	No aerosol	23 km visibility	5 km visibility
Cloud/Rain Aerosol Extension	No cloud or rain	No cloud or rain	Cumulus Clouds
Rain rate ($^{mm}/_{hour}$)	-	-	2
Ground altitude from sea level (m)	800	800	800
Latitude	32:52	32:52	32:52
Longitude	39:56	39:56	39:56
Season	Summer	Summer	Summer
Date ($day/month/year$)	01/06/2013	01/06/2013	01/06/2013
Hour	13:00	13:00	13:00
Type of ground	Grass	Grass	Grass
Ground reflection	Active	Active	Active

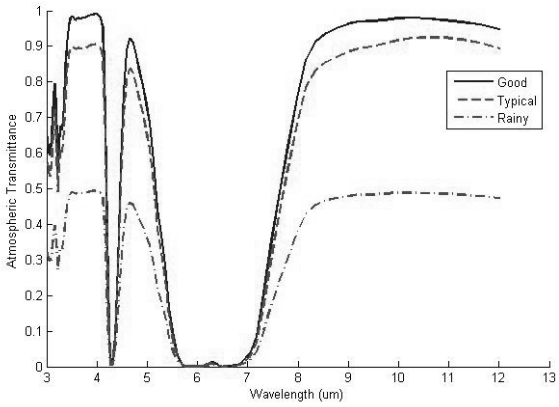

Figure 2.12: Atmospheric Transmission

Atmospheric path radiance contains emitting radiation of particles along the path in missile LOS between missile and source. Thus, path radiance component is added over radiation of source on scene. For aircraft, total radiation calculation is equal to summation of integrated spectral path radiance and integrated spectral radiance values. Integrated radiance value calculations are shown at equation 2.1. The intervals of integration are determined by dual band detector spectral responses. Equation 2.2 shows that the total radiation of aircraft ($L_{A_{Total}}$). $L_{path-radiance}$ indicates integrates spectral path radiance output of MODTRAN. However, for total flare radiation calculation, there are some difference because of flare radiation depends on time function which will be explain in detail at Chapter 4. The total flare radiation is shown at equation 2.3. Where, $L_F(t)$ is radiance value of flare with a given time and $L_{F_{Total}}$ is total

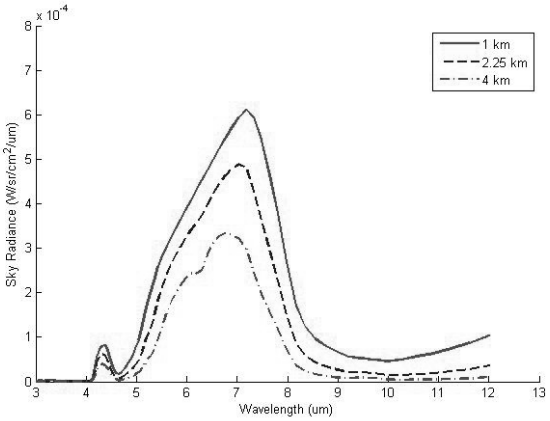

Figure 2.13: Spectral Sky-radiance

radiance of flare.

$$L = \int_{\lambda_1}^{\lambda_2} L(\lambda, T)\mathrm{d}t \tag{2.1}$$

$$L_{A_{Total}} = L_A + L_{path-radiance} \tag{2.2}$$

$$L_{F_{Total}} = L_F(t) + L_{path-radiance} \tag{2.3}$$

Background radiation of IR image is determined by spectral sky-radiance output of atmospheric effects. Thanks to equation 2.1, spectral sky-radiance is integrated. Then, integrated spectral sky-radiance value is equalized the background radiation of IR image as shown equation 2.4. Where, L_B is background radiation and $L_{sky-radiance}$ is integrated spectral sky-radiance output of MODTRAN.

$$L_B = L_{sky-radiance} \tag{2.4}$$

In addition to these, all these total radiation and background radiation are calculated for MWIR ($3-5\ \mu m$) and LWIR ($8-12\ \mu m$) spectral bands which are spectral responses of dual band of detector.

2.2.3 E/O Block

E/O block of IR seeker contains dome, lenses, mirrors and filters. Dome protects IR seeker and collect IR energy over lenses or mirrors. Collected IR energy is directed on IR filters thanks to optic lenses or mirrors. Because of dual band technology, there are two filters which suppress IR energy of wavelengths are required. These wavelengths determine the spectral

responses of dual band detector. E/O block is assumed ideal which means that there is no loss incoming light of IR energy in this study.

2.2.4 IR Detector Model

IR detector converts radiation energy to electrical energy with respect to its spectral responsivity characteristic. In this study, dual band FPA detector is modeled for staring type imaging seeker design. Spectral responses of modeled detector are MWIR and LWIR as mentioned at Section 1.2.1.1. IR detector has pixel array whose resolution can be arranged by user. However, resolution of detector is set to $256X256$ pixels. This resolution value is optimum because of computation restrictions and performance of seeker. The higher resolution causes computational complexity but provides better performance. On the contrary, performance of seeker with lower resolution detector is worse but processing of detector output signal is faster.

So as to calculate power received by detector, spectral responsivity, NEP, SNR, FOV, solid angle and spectral transmission characteristics of detector are required [9]. There is an assumption in this study that, detector is modeled as processing an IR image formed with received radiation from scene. Thus, only FOV of detector and radiation values of all pixels are required to create an IR images. The order of creating IR images is numerated below and detailed in following sections.

- Calculate IR radiation values of background, aircraft and ECM ammunitions for dual band as mention 2.2.2, Chapter 4 and Chapter 5 respectively.
- Add atmospheric effects over calculated IR radiation of sources as detailed in Section 2.2.2.
- Convert radiation values to RGB colors in order to create an IR image.
- Calculate LOS direction of seeker so as to determine scene within FOV of seeker.
- Capture the scene and create an IR image for dual band thanks to MATLAB Camera Toolbox.
- Send both MWIR and LWIR band images to processor.

2.2.4.1 Conversion Radiation to RGB Colors

The purpose of creating IR image, it is necessary to convert radiation values of sources to RGB colors. Conversion is satisfied with MATLAB *colormap* function which generates RGB color matrix at selected color map. In this study, MATLAB's *Jet* and *HSV* color maps (as shown Figure 2.14) with 4096 different colors are chosen to create an IR image of scene. Figure 2.15 and Figure 2.16 indicates *HSV* and *Jet* color map at viewpoint of missile seeker.

Radiations of sources are calculated with Plank Law as shown equation 1.3. Plank Law has dependency 5^{th} order of wavelength and exponential of temperature and wavelength of sources as seen equation 1.11. Even temperature of sources have a small difference, their radiations cause huge difference. Thus, not only there are not linear relationships between selected *colormap* and radiation values of sources but also hot source and other sources cannot be seen at the same image. To overcome this problem, the new idea is proposed which compresses

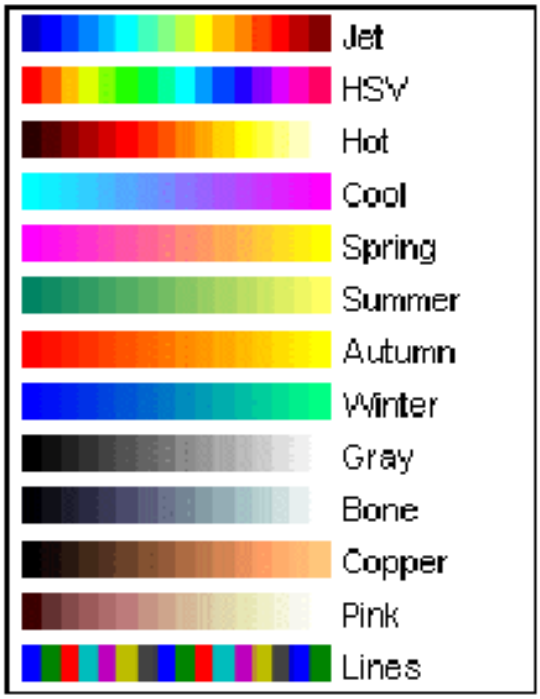

Figure 2.14: Color Maps of MATLAB

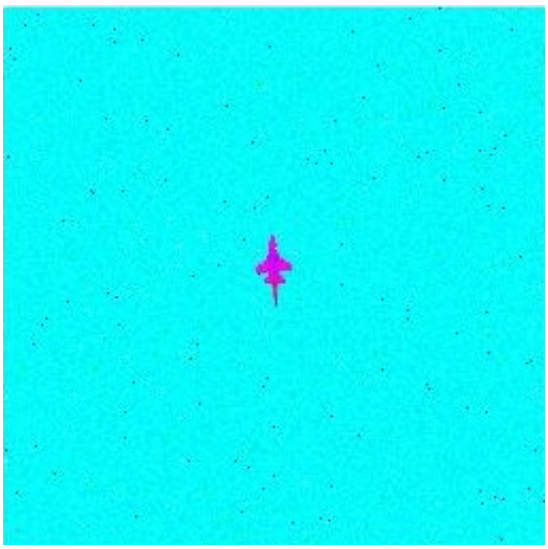

Figure 2.15: *HSV* Colormap

the radiation values of sources and determines appropriate RGB color. The color index is calculated with equation 2.5. Where, $L_{D_{Max}}$, $L_{D_{Min}}$ and L_{Source} are maximum detectable radiance, minimum detectable radiance of detector and source radiance.

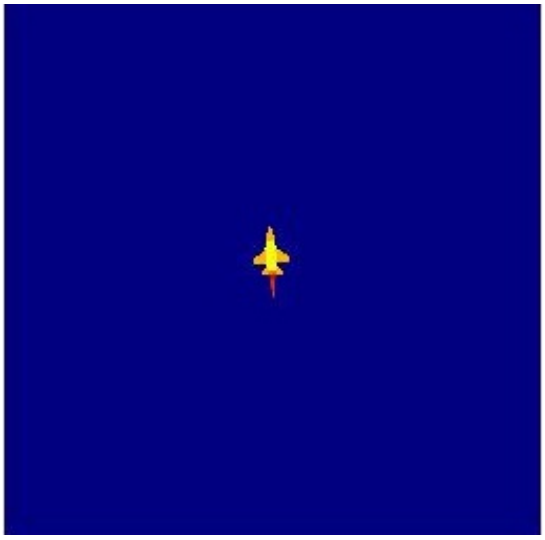

Figure 2.16: *Jet* Colormap

$$Color\ Index = floor(\frac{(log(L_{Source})^3 - log(L_{D_{Max}})^3).4095}{log(L_{D_{Max}})^3 - log(L_{D_{Min}})^3} + 4096) \tag{2.5}$$

Compression method is dependent on minimum and maximum detectable radiance values of detector as illustrated at Table 2.3. These values are determined with respect to background for detection of minimum detectable radiance and flare radiation for detection of maximum detectable radiance of detector scope of this study. Color matrix size is $4096X3$ RGB values. These 4096 different colors are matched with source radiation which ranges from minimum and maximum detectable radiance values of detector.

Table 2.3: Detector Maximum and Minimum Detectable Radiance Values

Detector Band	Minimum Detectable Radiance ($\frac{W}{sr.cm^2}$)	Maximum Detectable Radiance ($\frac{W}{sr.cm^2}$)
MWIR	10^{-5}	4
LWIR	$3\ 10^{-4}$	0.5

There is an example shown at Table 2.4. $280\ K$ and $350\ K$ radiance of source ratio is quite smaller than ratio of $350\ K$ and $1000\ K$ radiation of sources. Thus, background and $280\ K$ source may have same color index. Hot sources cause the other source seen as background unless compressed radiation. After compression, background and other sources can be easily discriminated by detector. Table 2.4 indicates that, compressed radiance value is color matrix index at the same time.

Table 2.4: Temperature and Color Index

Temperature (K)	Radiance ($\frac{W}{sr.cm^2}$)	Compressed Radiance (Color Index)
Background	$5.23\ 10^{-5}$	761
280	$21\ 10^{-5}$	1235
350	$50\ 10^{-5}$	1455
1000	$204\ 10^{-3}$	2039

2.2.4.2 Calculation of LOS

Calculation of LOS is crucial for both IR image creation and guidance law of missile. Due to LOS is a straight line along missile seeker boresight view, missile seeker LOS determines the scene on detector. In this study, LOS angle is identical to summation of missile rotation and gimbal rotation as shown equation 2.6.

$$\begin{aligned} \lambda_{az} &= \psi_M + \psi_G \\ \lambda_{el} &= \theta_M + \theta_G \end{aligned} \tag{2.6}$$

2.2.4.3 Create an IR Image

The final step for detector model is creating an IR images. To create an image, MATLAB Camera Toolbox and *fill3* function are used. Initially, all scene sources are plotted with *fill3* function. This function requires 3D vertice coordinates with appropriate order and color of polygons. The detailed IR signature and 3D models of target and flare will be explained in Chapter 4 and Chapter 5. Colors are generated with respect to radiation values of model at Section 2.2.4.1 with radiation values of sources. Then, MATLAB Camera functions *campos*, *camva*, and *camtarget* are used. *camva* function arranges missile FOV in degree. In this study, missile FOV is chosen 6^o. *campos* requires the missile seeker 3D position and *camtarget* requires LOS direction of missile. Inputs of *campos* and *camva* functions are known by missile. However, *camtarget* is not exactly known. The approach to measure target position, LOS angle of seeker is used. [23], [24]

The calculation of target position with LOS angle is related with earth-fixed position of gimbal. Because, missile seeker is mounted on gimbal. Rotation of earth-fixed coordinate of gimbal position with LOS angles as shown equation 2.6 gives the direction of LOS of missile seeker. Equation 2.7 indicates transformation of missile seeker position from body-coordinate to earth-fixed coordinate. Where, P_{EM} is missile earth-fixed coordinate, P_{BG} is gimbal body-coordinate position, T_{EB_G} is transformation matrix filled with Euler angles of missile and P_{EG} is earth-fixed position of missile gimbal and seeker. Then, missile gimbal earth-fixed position is rotated with LOS angles gives the LOS direction.

$$P_{EG} = T_{EB_G}.P_{BG} + P_{EM}$$

$$P_{LOS} = \begin{bmatrix} cos(\lambda_{az})cos(\lambda_{el}) & -sin(\lambda_{az}) & cos(\lambda_{az})sin(\lambda_{el}) \\ sin(\lambda_{az})cos(\lambda_{el}) & cos(\lambda_{az}) & sin(\lambda_{az})sin(\lambda_{el}) \\ -sin(\lambda_{el}) & 0 & cos(\lambda_{el}) \end{bmatrix} .P_{EG} \tag{2.7}$$

Thanks to MATLAB Camera Toolbox, scene 3D images are created. Finally, these images are captured. After capture, blurring effect and salt-pepper noises are added on images. MATLAB *imnoise* and *imfilter* functions are used to add noise on image. Inputs such as density, mean and variance of generated noises are determined with respect to weather condition. If it is rainy, the noisiest image is captured. The captured noisy image is illustrated at Figure 2.15. After noise addition, captured MWIR and LWIR noisy images are sent to processor model.

2.2.5 Processor Model

Processor model which takes IR images of dual band detectors and extracts features of all sources in FOV of missile seeker. In the following sections first, background subtraction step is detailed. Then, thresholding and feature extraction are detailed respectively.

2.2.5.1 Background Subtraction

Background subtraction method eliminates background noise that is under background threshold level. Background threshold level is related with radiation of source as detailed in Section 2.2.4.1 . For determination of this level, MATLAB Image Toolbox is used. First, RGB images are converted gray scaled image thanks to MATLAB *rgb2gray* function as shown equation 2.8. Where, I_{Gray} is gray scaled image and I_{RGB} is RGB images. Pixel values of gray scaled image are normalized range from 0 to 255 gray scale levels with respect to radiation level of RGB images.

$$I_{Gray} = rgb2gray(I_{RGB}) \tag{2.8}$$

To subtract background noise, background threshold is determined with *graythresh* function which computes a normalized background threshold that lies in the range [0, 1]. Then this background threshold level is used in gray scaled image to convert binary image by thresholding. *im2bw* MATLAB function is used for this purpose as shown equation 2.9. Where, $level_{BTh}$ is background threshold level and I_{Binary} is binary image. [24]

$$\begin{aligned} level_{BTh} &= graythresh(I_{Gray}) \\ I_{Binary} &= im2bw(I_{Gray}, level_{BTh}) \end{aligned} \tag{2.9}$$

Figure 2.17 which is an example summarizes all these background subtraction process.

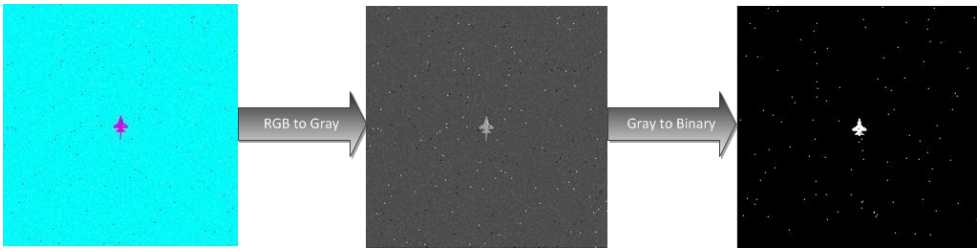

Figure 2.17: Background Subtraction

2.2.5.2 Feature Extraction

Feature extraction model extracts candidate of targets feature vector sets which include angular position with respect to missile seeker FOV, area on detector and spectral ratio. Aiming to extract features of binary image created after background subtraction, MATLAB morphological operation *bwmorph*, *bwlabel* and *regionprops* functions are used.

bwmorph function shown at equation 2.11, applies morphological operations on binary images and filters the binary images with respect to desired operations. This function may be used for different operations on pixels of binary image. In this study, *'clean'* operation is selected because of eliminating pixel whose value is one surrounded by pixels whose values are zero as shown Figure 2.18. Thanks to this operation, one pixel noises are eliminated as shown Figure 2.19.

$$I_{BW_{morph}} = bwmorph(I_{Binary},' clean') \tag{2.10}$$

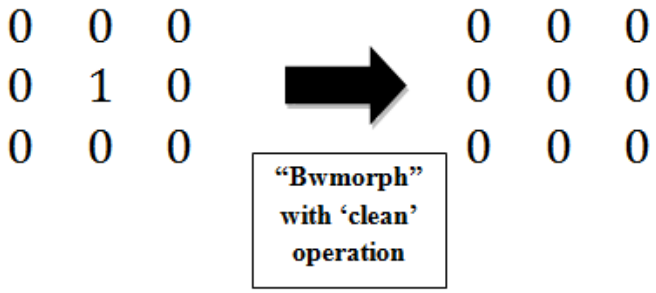

Figure 2.18: *'clean'* Operation at *bwmorph* Function

bwlabel function labels the connected objects on 2D images which is output of *bwmorph* function as illustrated at equation 2.11. Labeled image $I_{BW_{Labeled}}$ is $256X256$ matrix containing labels for the connected objects in $I_{BW_{Morph}}$ binary and filtered morphological image. *'number'* parameter which may either 4 or 8 determines the orientation of connected neighbor pixels of object.

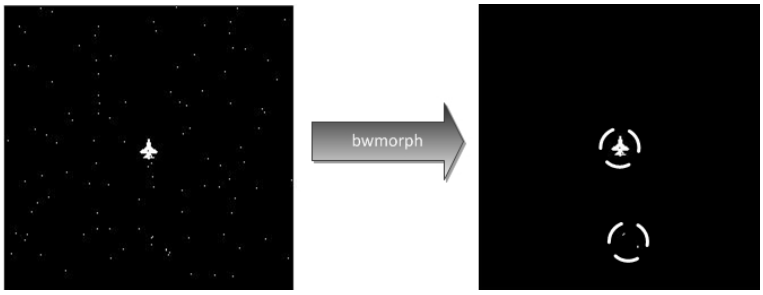

Figure 2.19: *bwmorph* Function

$$I_{BW_{Labeled}} = bwlabel(I_{BW_{Morph}}, number) \tag{2.11}$$

The last function is to extract feature vector is *regionprops* function which measures and extracts features of all connected objects on labeled image which is output of *bwlabel* function. The measured features are area, pixel centroid, pixel list etc. In this study, area, pixel centroid and pixel list are sufficient for each connected objects.

Filtered output of *bwmorph* function binary image which is shown at Figure 2.19 is given to *bwlabel* and *regionprops*, the output images and features are shown at Figure 2.20.

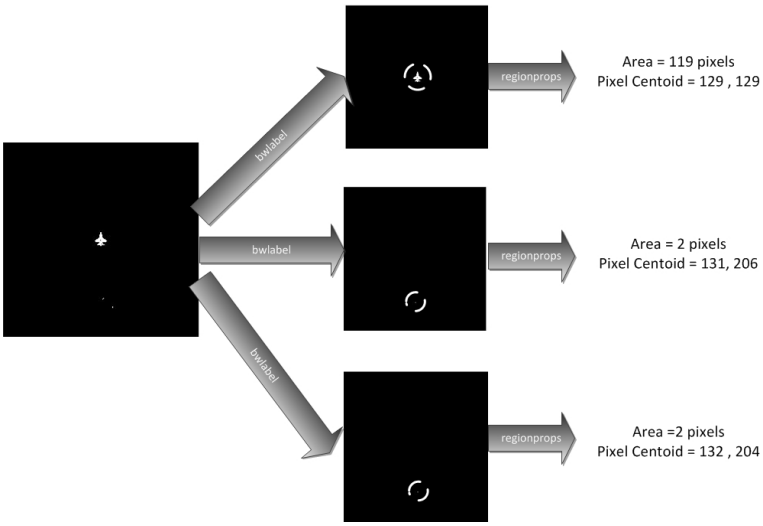

Figure 2.20: *bwlabel* and *regionprops* Functions

Area Threshold: is used for cleaning features of objects whose area is under area threshold level. In this study area threshold in pixel is set to 20 pixels for resolution $256X256$ detectors. Figure 2.21 shows an example that second and third objects are cleaned because of area thresholding.

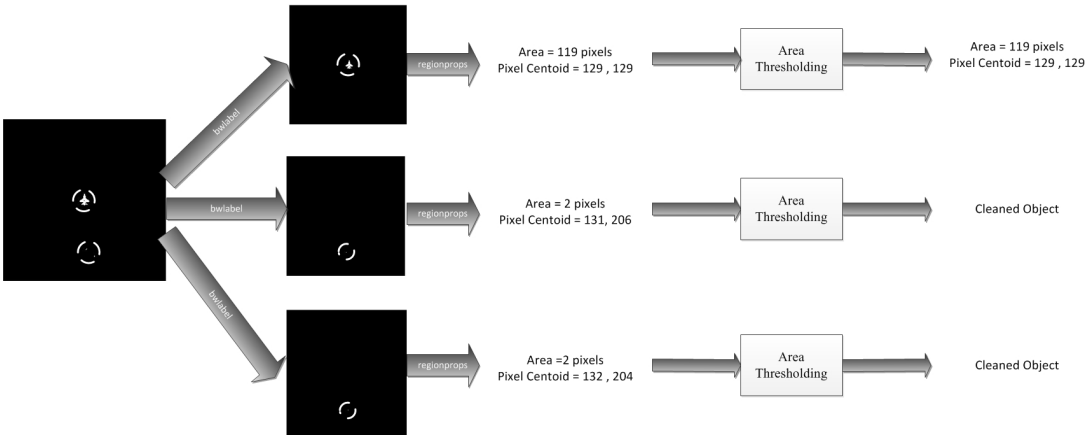

Figure 2.21: Area Thresholding

Centroid Detection: After determination of all objects' features, centroid detection is applied to calculate position of target with respect to FOV of missile seeker. For this purpose, initially pixel centroid of objects should be determined. In this study, there are two methods in order to calculate centroids of objects. These are binary centroid and intensity centroid detections.

Binary Centroid Detection: Binary centroid detection detects objects position with respect to binary image values range from 0 and 1. For binary centroid detection, *regionprops* function centroid output is used. Thus, instead of binary centroid detection, *regionprops* function centroid output is chosen to calculate object centroid.

Intensity Centroid Detection: Intensity centroid detection detects object position with respect to gray image values range from 0 to 255 as shown equation 2.14. Where, i is selected object index, M is total object number on scene, X is horizontal pixel position, Y is vertical pixel position, I is selected pixel intensity value j is pixel list number of selected object, N is total pixel list of selected object, $X_{C_{intensity}}$ is X axis center of selected objects with intensity and $Y_{C_{intensity}}$ is Y axis center of selected objects with intensity.

Vertical and horizontal position of pixels of selected object is weighted with pixel gray intensity value. Then, these weighted positions are divided total intensity of pixels. As a result, intensity centroid pixel positions of selected objects are derived. [9]

$$
\begin{aligned}
X_{C_{intensity}} &= \frac{\sum_{j=1}^{N_i}(X_j.\ I_{X_{i=1:M,j=1:N_i},Y_{i=1:M,j=1:N_i}})}{\sum_{j=1}^{N_i} I_{X_{i=1:M,j=1:N_i},Y_{i=1:M,j=1:N_i}})} \\
Y_{C_{intensity}} &= \frac{\sum_{j=1}^{N_i}(Y_j.\ I_{X_{i=1:M,j=1:N_i},Y_{i=1:M,j=1:N_i}})}{\sum_{j=1}^{N_i} I_{X_{i=1:M,j=1:N_i},Y_{i=1:M,j=1:N_i}})}
\end{aligned}
\tag{2.12}
$$

There is an example illustrated at Figure 2.22. There are two objects in FOV of missile seeker.

Their pixels intensity values are given in pixel boxes. Horizontal positions of pixels are shown as $X1$, $X2$, and $X3$. Equation 2.13 gives the horizontal intensity centroid of selected object as seen Figure 2.22.

$$X_{C_{intensity}} = \frac{92.X_1 + 150.X_2 + ...}{92 + 150 + ...} \tag{2.13}$$

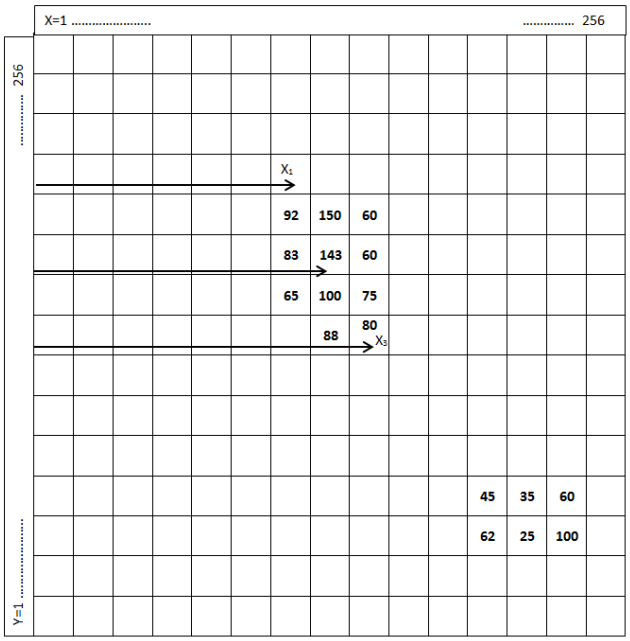

Figure 2.22: Intensity Centroid Detection

Pixel to Angular Position Conversion: The final step for centroid detection is to convert pixel position to angular position with respect to missile seeker and FOV angle. So as to calculate angular position of all objects on scene, equation 2.14 are used. Where, ϵ_M is error angle which is shown at Figure 2.23. At the same time ϵ_M is angular position of target with respect to missile seeker, FOV is missile seeker FOV angle which is arranged 6^o, X_D and Y_D are resolution of detector which are $256X256$ in this study and X_C, Y_C centroid of object on scene.

$$\begin{aligned} \epsilon_{M_{az}} &= FOV.\ \frac{0.5X_D - X_{C_{i=1:M}}}{X_D} \\ \epsilon_{M_{el}} &= FOV.\ \frac{Y_{C_{i=1:M}} - 0.5Y_D}{Y_D} \end{aligned} \tag{2.14}$$

Spectral Ratio: Spectral ratio means ratio between LWIR radiation values and MWIR radiation values of dual band detector at missile seeker. Then, this ratio will be used in spectral ECCM techniques so as to discriminate flare and aircraft. So as to calculate spectral ratio of

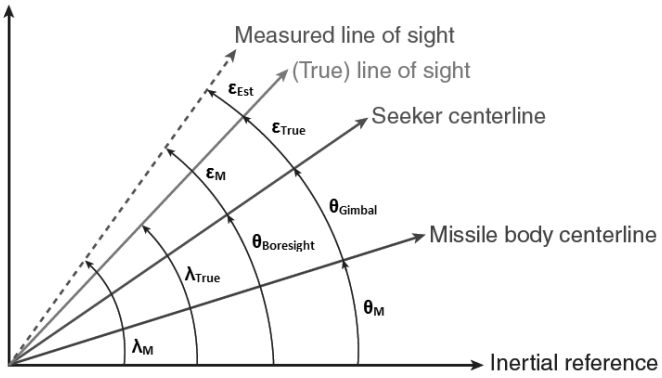

Figure 2.23: Missile Seeker Angular Geometry

all objects on scene, radiation values of all pixels of objects are required. As similar with radiation to RGB color conversion detailed at Section 2.2.4.1, RGB color to radiation conversion is applied for all pixels. Pixel list feature and RGB color index are required to calculate radiation values with RGB color to radiation conversion as shown equation 2.15. Where, f is function of conversion from RGB color to radiation values and L is radiation of object. The first column of pixel list gives the X pixel number and second column of pixel list gives Y number for selected object pixel list on binary image.

$$\begin{aligned} L^{MWIR}_{X_{i=1:M,j=1:N_i},Y_{i=1:M,j=1:N_i}} &= f(RGB_{X_{i=1:M,j=1:N_i},Y_{i=1:M,j=1:N_i}}) \\ L^{LWIR}_{X_{i=1:M,j=1:N_i},Y_{i=1:M,j=1:N_i}} &= f(RGB_{X_{i=1:M,j=1:N_i},Y_{i=1:M,j=1:N_i}}) \end{aligned} \tag{2.15}$$

After conversion RGB color to radiation for all objects, ratios of pixel radiation values are determined with given equation 2.16. Where, R is ratio of LWIR and MWIR radiation level of selected pixel of object.

$$R_{X_{i=1:M,j=1:N_i},Y_{i=1:M,j=1:N_i}} = \frac{L^{LWIR}_{X_{i=1:M,j=1:N_i},Y_{i=1:M,j=1:N_i}}}{L^{MWIR}_{X_{i=1:M,j=1:N_i},Y_{i=1:M,j=1:N_i}}} \tag{2.16}$$

Next, this ratio level is compared with threshold which is arranged that target radiation ratio is only exceeding this threshold. In this study, this ratio is set to 0.5. Equation 2.17 demonstrates that, thresholding function is applied for all pixels of selected object. Where, T_R refers thresholded ratio value of selected pixel of object.

$$\begin{aligned} if\ R_{X_{i=1:M,j=1:N_i},Y_{i=1:M,j=1:N_i}} > 0.5 \Rightarrow T_{R_{X_{i=1:M,j=1:N_i},Y_{i=1:M,j=1:N_i}}} = 1 \\ else\ T_{R_{X_{i=1:M,j=1:N_i},Y_{i=1:M,j=1:N_i}}} = 0 \end{aligned} \tag{2.17}$$

The final step is to determine total number pixels of objects which exceeds the threshold.

For this purpose equation 2.18 is used. Where, T_{SR} refers total pixel number which exceed threshold 0.5.

$$T_{SR_{i=1:M}} = \sum_{i=1}^{M} \sum_{j=1}^{N_i} T_{R_{X_{i,j},Y_{i,j}}} \tag{2.18}$$

Spectral ECCM of objects is set to 1, if T_{SR} total number of number of pixels which exceeds the threshold of selected object is bigger than 65% selected objects pixel area in equation 2.19. Where, A is pixel area of selected object, $ECCM_{M_{spectral}}$, $ECCM_{I_{spectral}}$ are matching and identification spectral ECCM values of objects.

$$\begin{gathered} if\ \frac{T_{SR_{i=1:M}}}{A_{i=1:M}} > 0.65 \Rightarrow ECCM_{M_{spectral_{i=1:M}}} = ECCM_{I_{spectral_{i=1:M}}} = 1 \\ else\ ECCM_{M_{spectral_{i=1:M}}} = ECCM_{I_{spectral_{i=1:M}}} = 0 \end{gathered} \tag{2.19}$$

2.2.6 ECCM Model

Basis aims of ECM techniques are to deceive missile seeker and break lock of missile. However, advanced missile seeker can distinguish target and ECM due to ECCM techniques. IIR seeker extracts more detailed information from scene rather than elder IR seeker. This crucial advance provides missile to identify sources on scene thanks to trajectory, kinematic motion, instantaneous separation rate, IR signature characteristics, intensity rise-time, and area of sources.[9], [20]

Scope of this study; denomination, area, spectral (dual band ratio), sector strengthening, track gate and kinematic ECCM techniques are developed. These advanced techniques are applied at matching block, identification block or gimbal model as shown Table 4.6. Matching block, identification block and gimbal will be detailed in following sections. At the same time, all these ECCM techniques and their applications at matching and identification blocks are detailed in the following section.

Table 2.5: Advanced ECCM Techniques

ECCM Technique	Matching Block	Identification Block	Gimbal Model
Area	√	√	-
Spectral	√	√	-
Kinematic	√	√	-
Sector Strengthening	-	√	-
Denomination	-	√	-
Target Track Gate	-	-	√

2.2.6.1 Area ECCM Technique

Area ECCM controls instantaneous area change of sources. This ECCM is applied at matching and identification block. Matching block matches sources seen present time with sources occurred at previous time. Previous time occurred sources' track histories are stored at memory to compare with present sources.

To compare the areas of sources, previous time sources' areas are estimated in present time with Kalman Filter. Estimated areas of sources with respect to area histories are compared with areas of present time sources. Area ECCM has an area gate to control instantaneous area change. This gate is percentage of estimated area. Present time source area must be inside of this gate, if matching is occurred. The approach of area ECCM is shown at equation 2.20. Where, $ECCM_{M_{AreaGate}}$ is matching area gate percentage between 0 and 1, $ECCM_{M_{area}}$ is matching area ECCM values of source, K is total number of one sample previous seen sources, M is total number of present time seen sources, $A^{\sim}$ is estimated area, A is area of sources at present time and t is time of simulation.

$$\begin{aligned} if\ (1 - ECCM_{M_{AreaGate}}).A^{\sim}_{j=1:K,t-1} \ &< \ A_{i=1:M,t} \\ < (1 + ECCM_{M_{AreaGate}}).A^{\sim}_{j=1:K,t-1} \ &\Rightarrow \ ECCM_{M_{area_{i=1:M}}} = 1 \\ else\ ECCM_{M_{area_{i=1:M}}} &= 0 \end{aligned} \tag{2.20}$$

If area ECCM is triggered, the matching weight of sources is added with matching area ECCM weight which is 20%.

Similarly, area ECCM is also used at identification block which identify sources on scene as *"T"*, *"F"* or *"N"* which indicate target, flare and non-defined objects respectively. Equation 2.21 demonstrates area ECCM control at identification block. Where, $ECCM_{I_{AreaGate}}$ is area gate percentage of identification block and $ECCM_{I_{area}}$ is identification area ECCM values of source. In this study, the weight of area ECCM at identification block is set to 20% as well.

$$\begin{aligned} if\ ((1 - ECCM_{I_{AreaGate}}).A^{\sim}_{j=1:K,t-1} \ &< \ A_{i=1:M,t} \\ < (1 + ECCM_{I_{AreaGate}}).A^{\sim}_{j=1:K,t-1} \ &\Rightarrow \ ECCM_{I_{area_{i=1:M}}} = 1 \\ else\ ECCM_{I_{area_{i=1:M}}} &= 0 \end{aligned} \tag{2.21}$$

For example, there are 3 previous sources whose estimated area are 250, 100 and 300 pixels in Figure 2.24. At the same time, there is a present time source whose area is 280 pixels. If, area gate is assumed 10%. Only third source provides the area gate and its area ECCM is set to 1.

2.2.6.2 Spectral (Dual Band Spectral Ratio) ECCM Technique

The main reason why the modeled IR detector is dual band in this study is to apply spectral ECCM technique. Dual band detector compares these dual band radiations of each source on scene. If ratio of MWIR to LWIR is exceeded spectral threshold, spectral ECCM is triggered.

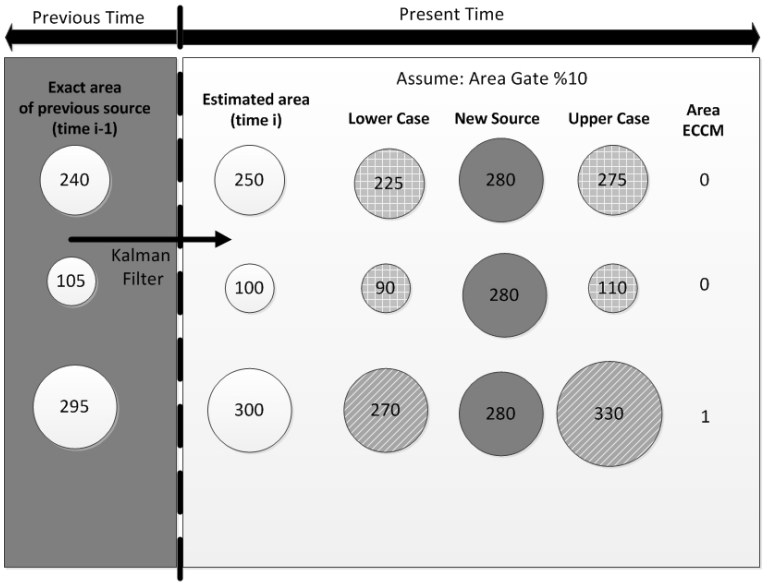

Figure 2.24: Algorithm of Area ECCM Technique

Calculation methods and methodology of concept is detailed at spectral ratio paragraph at Section 2.2.5.2.

Spectral ECCM is used both matching and identification blocks. However, their weight values are different. Because of that, the main purpose of spectral ECCM is to discriminate flare ECM ammunitions. Thus, spectral ECCM is more important for identification block than matching block. In this study, matching spectral ECCM weight is set to 30%. However, identification spectral ECCM weight is 35%.

2.2.6.3 Kinematic ECCM Technique

Kinematic ECCM technique estimates sources' one step ahead kinematic motions to match present time occurred sources with sources occurred at previous time. At the same time, kinematic ECCM technique is used at identification block as well.

In this study, motions of sources are estimated with Kalman Filter thanks to position history of tracked sources. Due to estimated angular azimuth and elevation positions of sources, kinematic position gate is formed. If present time seen source is in this gate, the weight of kinematic ECCM is summed with total weight of source. The weight of kinematic ECCM at matching block is 50%. However, this weight is diminished to 25% at identification block. Because, identification block profits from 4 different ECCM techniques unlike matching block which uses only 3 ECCM techniques as shown at Table 4.6. Moreover, kinematic ECCM is more important ECCM technique for matching sources than identification of sources.

There is an example at Figure 2.25, where two sources at track history and one sources at present time. First, sources' present time positions are estimated with Kalman Filter. Then

kinematic gate is formed with given kinematic gate parameter which is assumed $^{FOV}/_{25}$. After that, present time source's position is compared either inside gate or outside. If it is inside the gate, kinematic ECCM is set to 1 and weight of present time source is summed with kinematic ECCM weight.

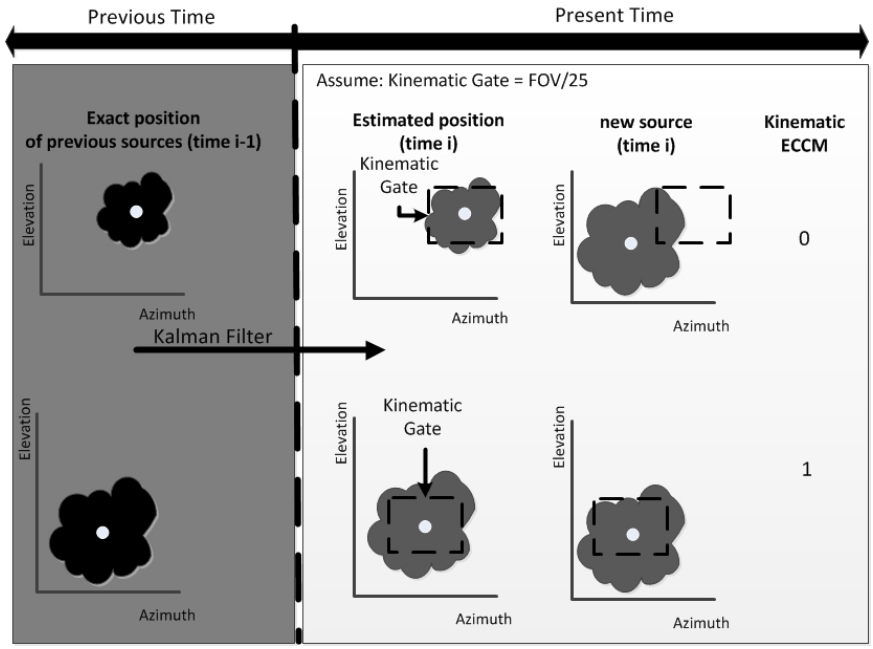

Figure 2.25: Algorithm of Kinematic ECCM Technique

2.2.6.4 Sector Strengthening ECCM Technique

Sector strengthening ECCM attenuates out of gate where target is not expected. Determination of sector strengthening gate where target is expected is the crucial parameter of this technique. Scope of this study, this gate is formed with respect to previous frame decided target position. Decided target position means that, gimbal locks on this target and sends its angular position to guidance law so as to generate commanded acceleration. Thus, target is stuck on gate. Instantaneous movements are detected and new target candidates are eleminated so as to avoid locking of ECM ammunitions.

This technique is only used at identification block so as to identify target. On the contrary of other ECCM techniques detailed, sector strengthening ECCM has not weight. Unless present time source is inside the sector strengthening gate, that source will not be identified as *"T"*. To summarize, any source is identified as *"T"*, it is inside the sector strengthening gate.

There is an example as demonstrated at Figure 2.26 where there are two different scenarios. One of them has flare and target on scene. Target is decided and tracked by gimbal of missile. Then, strengthening gate is formed. Next, present time source is inside this gate. Thus, sector strengthening ECCM is set to 1. However, second scenario's present time seen source is not inside strengthening gate. Thus ECCM is set to zero.

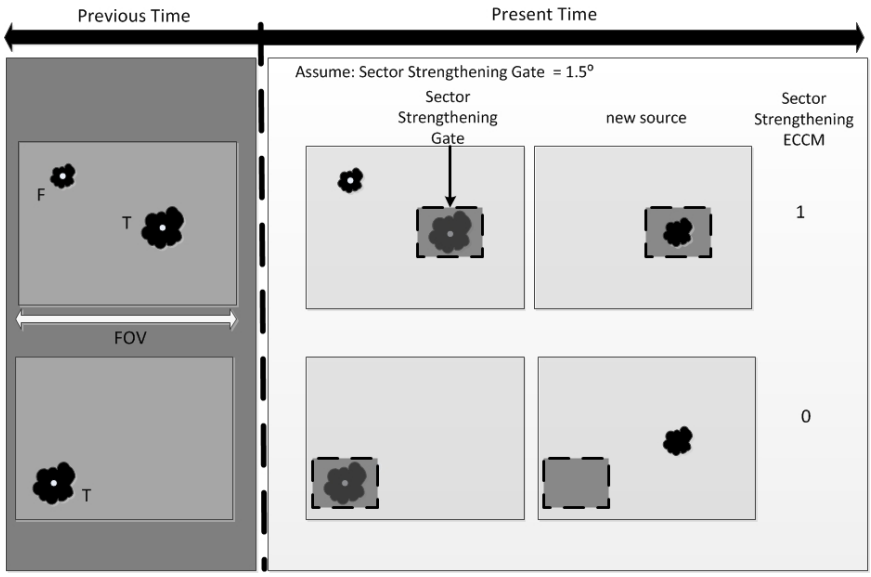

Figure 2.26: Algorithm of Sector Strengthening ECCM Technique

2.2.6.5 Denomination ECCM Technique

Denomination ECCM technique depends on naming of sources in FOV of missile. It is only applied at identification block which denominates sources at present simulation time with denomination of matched source seen at previous simulation steps. The denomination of sources are *"F"*, *"T"*, and *"N"* which are indicates flare, target and non-defined respectively.

Denomination ECCM is activated for source seen present time, when denomination of matched source seen previous time is *"T"* in equation 2.22. In this equation, j^{th} source among K sources seen previous time is matched with i^{th} source among M sources seen present. Where, $ECCM_{I_{denomination}}$ is denomination ECCM values of sources and $Name$ is name strings of one step before seen sources.

$$\begin{aligned} if\ Name_{j=1:K,t-1} == 'T' \Rightarrow ECCM_{I_{denomination}{}_{i=1:M}} = 1 \\ else\ ECCM_{I_{denomination}{}_{i=1:M}} = 0 \end{aligned} \tag{2.22}$$

If denomination ECCM is activated for any source, its weight of identification is summed with denomination ECCM weight which is arranged 20% normalized value in this study. The example of denomination ECCM application is shown at Figure 2.27.

2.2.6.6 Target Track Gate ECCM Technique

IR guided gimbaled missile seeker must hold the target in FOV. Because IR guided missiles are fire-and-forget type missile. If target leaves from FOV of missile, missile cannot response it and its track may be broken. So as to hold the target in FOV, target track gate is used. This ECCM technique is only used at gimbal model which directs missile seeker so as to

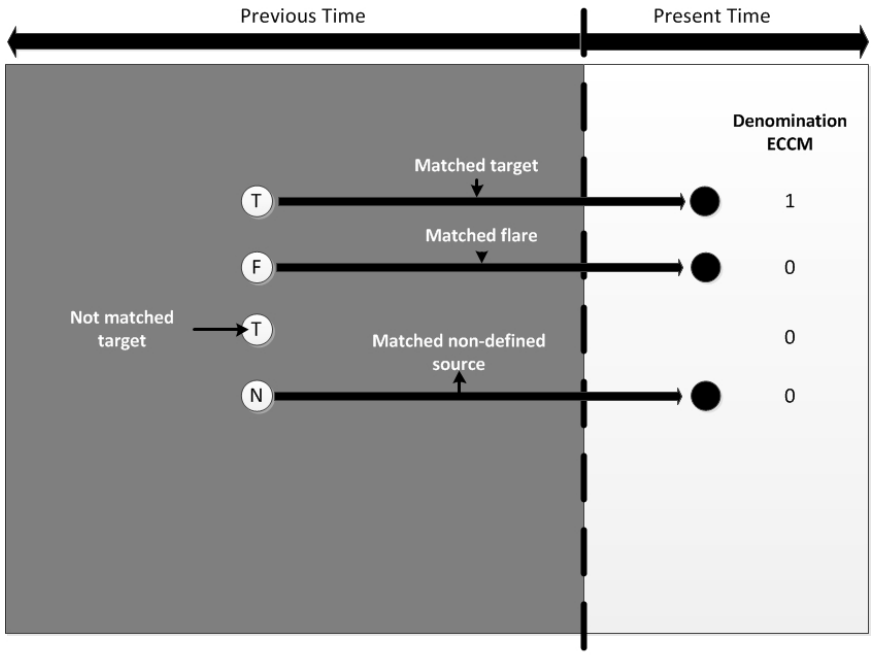

Figure 2.27: Algorithm of Denomination ECCM Technique

hold identified as *"T"* and decided target on FOV of seeker. This ECCM technique makes this decision that which *"T"* identified source will be tracked by gimbal. The reason why this ECCM model is developed that there would be more than one target identified as *"T"* on FOV of seeker. In this condition, gimbal model cannot make a decision to select one target and track it. This ECCM removes this problem by means of helping gimbal to make a decision.

Target track gate size determination is depending on centering of target position which is identified and decided at previous simulation step. This position information is carried present time so as to form target track gate as shown Figure 2.28. Where, target track gate is formed at one simulation step before seen *"T"* source's center. Then, new sources are compared whether or not they are inside this gate.

2.2.6.7 Matching Block

Matching block matches sources with track history sources due to weighted resemblance characteristics. Matching block uses area, spectral and kinematic ECCM so as to match sources. These three ECCM techniques have individual weight as listed Table 2.6. Kinematic ECCM is the most critical technique for matching block. Thus, its weight is higher than others.

The proposal matching algorithm working principle is as shown at flow chart Figure 2.29. Inputs of matching algorithm are present sources' features and track histories. These features include area, angular position and spectral ECCM values. Similarly, these track histories include area, angular position and spectral ECCM values of previously seen sources.

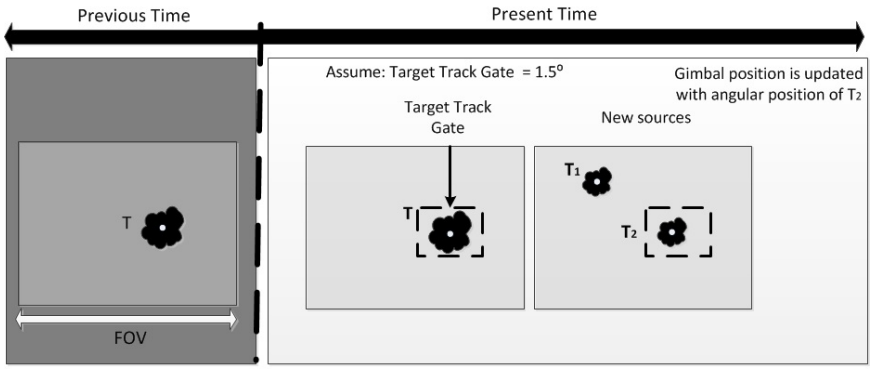

Figure 2.28: Algorithm of Target Track Gate ECCM Technique

Table 2.6: ECCM Weights on Matching Block

ECCM Technique	Symbol	Weight
Area	W_{M_a}	20%
Spectral	W_{M_s}	30%
Kinematic	W_{M_k}	50%

Outputs of matching algorithm are error and total weight for each matching candidates. Error and total weight calculations are shown at equation 2.23. Where, A_P is angular position of comparing sources. Angular position is generated at IR missile seeker, weights of matching block values are defined at Table 2.6. T_{M_W} is total weight of present seen sources.

$$
\begin{aligned}
error_{kinematic} &= W_{M_k}(A_{P_{i,t}} - A_{P_{j,t-1}})^2 \\
error_{spectral} &= W_{M_s}(ECCM_{M_{spectral_{i,t}}} - ECCM_{M_{spectral_{i,t-1}}})^2 \\
error_{area} &= W_{M_a}(A_{i,t} - A_{j,t-1})^2 \\
error_{i,j} &= error_{kinematic} + error_{spectral} + error_{area} \\
T_{M_{W_{i,j}}} &= W_{M_k} ECCM_{M_{kinematic_{i,t}}} \\
&+ W_{M_s} ECCM_{M_{spectral_{i,t}}} + W_{M_a} ECCM_{M_{area_{i,t}}}
\end{aligned}
\tag{2.23}
$$

Whether $T_{M_{W_{i=1:M,j=1:N}}} > 51\%$ and $error_{i=1:M,j=1:N}$ is minimum; i^{th} present seen source and j^{th} previously seen source are matched. Then, all track history data of j^{th} previously seen source are updated with i^{th} present seen source. However, for each present seen target must only match with one source. Thus, there would be un-matched sources. If un-matched source is present seen source, this source is new source and new track is occurred for this source. However un-matched source is previously seen source, its track history updated with Kalman Filter and its tracking is aged. If tracking age is bigger than 3, this track history is deleted.

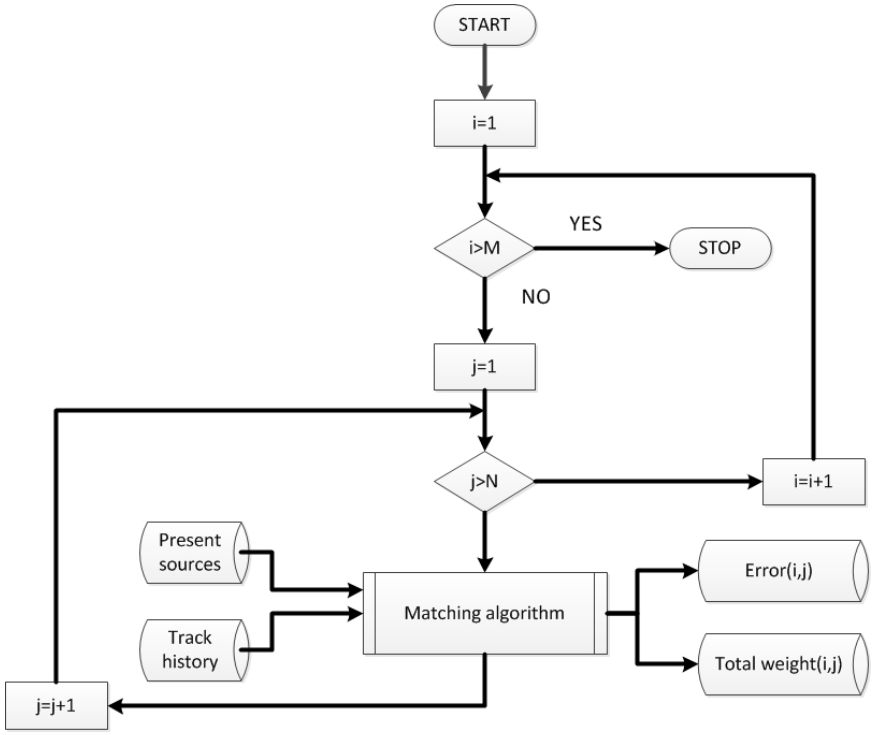

Figure 2.29: Algorithm of Matching Block

2.2.6.8 Identification Block

Identification block identifies and labels all sources with *"T"*, *"F"*, or *"N"*. This block uses denomination, area, spectral and kinematic ECCM. All ECCM techniques have its own weights as shown Table 2.7. At the same time, sector strengthening ECCM technique is used to hold target inside the strengthening gate. Spectral ECCM is the most important ECCM techniques for discriminating flare and target sources as seen at weight of identification block weights.

Table 2.7: ECCM Weights on Identification Block

ECCM Technique	Symbol	Weight
Area	W_{I_a}	20%
Spectral	W_{I_s}	35%
Kinematic	W_{I_k}	25%
Denomination	W_{I_d}	20%

Our approach for identification block is described in flow chart Figure 2.30. Where, t is simulation time step, $newsource$, $un-matched$ source information are given from matching block and T_{I_W} is identification total weight of present time seen source as derived at equation 2.24.

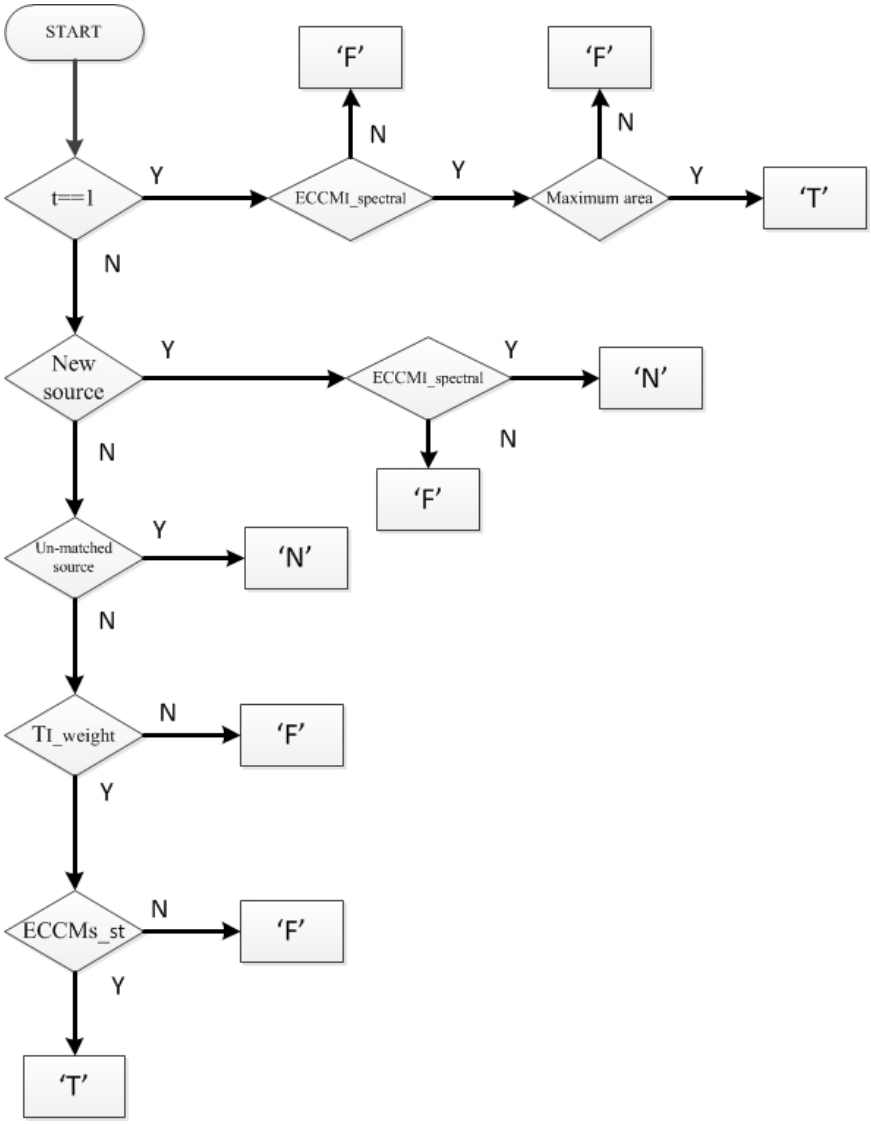

Figure 2.30: Algorithm of Identification Block

$$T_{I_{W_{i,j}}} = W_{I_k} ECCM_{I_{kinematic_{i,t}}} + W_{I_s} ECCM_{I_{spectral_{i,t}}} + W_{I_a} ECCM_{I_{area_{i,t}}} + W_{I_d} ECCM_{I_{denomination_{i,t}}} \tag{2.24}$$

Maximum area information is necessary for initializing of simulation. When simulation begins, there is no track history. Thus matching and identification blocks are nonfunctional. Due to solve this problem, spectral ECCM and area of sources on detector parameters are used to identify sources at the beginning of simulation. So as to identify the sources, T_{I_W} of each source must be bigger than 70% and sector strengthening ECCM must be triggered. Unless one of them is not provided, source is identified with *"F"* as shown flow chart.

2.2.7 Gimbal Model

Because of narrow FOV of seeker, gimbal is modeled not to break track lock of missile. Moreover, gimbal drives seeker towards direction of moving target [10]. It has two perpendicular and independent axes which are azimuth and elevation axes. It is driven by two servo-motors for these axes. The limit angles of servo motors are determined by gimbal FOR angle [2]. Gimbal rotation is independent of missile body rotation as shown Figure 2.23 unless reaching limit angles of servo motors.

In this study, modeled gimbal FOR angle is $\pm 60^o$. At the same time, modeled gimbal is ideal which means that gimbal directly rotates its axes towards target angular position, unless the total gimbal angles with respect to reference frame are equal or bigger than limit angles of gimbal. Total gimbal angle are updated for each simulation step with summation target angular position with respect to missile seeker and gimbal rotation in equation 2.25.

$$\begin{aligned} \psi_G(t+1) &= \epsilon_{M_{az}} + \psi_G(t) \\ \theta_G(t+1) &= \epsilon_{M_{el}} + \theta_G(t) \end{aligned} \tag{2.25}$$

As mention before, gimbal drives seeker towards target which is identified and labeled as *"T"* with identification block. However, identification block may label more sources as *"T"*. If there are two or more *"T"* identified sources on scene, gimbal cannot choice which identified sources will be tracked. That is why target track gate ECCM is developed as detailed in Section 2.2.6.6. Thanks to this technique, chosen source by gimbal will be tracked. Our approach is to gain this capability is shown at Figure 2.31.

Initialization of gimbal rotation is set to zero when there is no source detected by detector or there is no source labeled as *"T"* by identification block. However, gimbal rotation initialization is set to *"T"* identified source angular position while there is only source labeled as *"T"*. Whether there are more *"T"* labeled sources, gimbal rotation is set to *"T"* labeled source angular position which has maximum area among M sources. After initialization for each simulation step t, number of source is controlled. If number of source is identical to zero, gimbal rotation is set to linear extrapolation value of gimbal rotation vector which is filled at each simulation step. Yet, number of source is not equal to zero; number of labeled *"T"* sources is checked. If *"T"* number is zero; gimbal rotation is set to linear extrapolation value. If there is only one *"T"* labeled source; target track gate ECCM is controlled. As a result, gimbal rotation is set to either *"T"* labeled source angular position or previous gimbal rotation. The last, if number of *"T"* is more than one; for each *"T"* labeled source error term is calculated as show equation 2.26. Where, $\psi_G^{\sim}$ and $\theta_G^{\sim}$ are estimated gimbal angular position with linear extrapolation method and t is simulation time step. Then, target tracking gate ECCM is controlled for each sources with minimum error. If all conditions are satisfied for selected source, gimbal rotation is set to this target angular position. Otherwise, gimbal rotation is set to its previous rotation.

$$error(i) = (\epsilon_{M_{az_{i=1:K}}} - (\psi_{G_t}^{\sim} - \psi_{G_{t-1}}))^2 + (\epsilon_{M_{el_{i=1:K}}} - (\theta_{G_t}^{\sim} - \theta_{G_{t-1}}))^2 \tag{2.26}$$

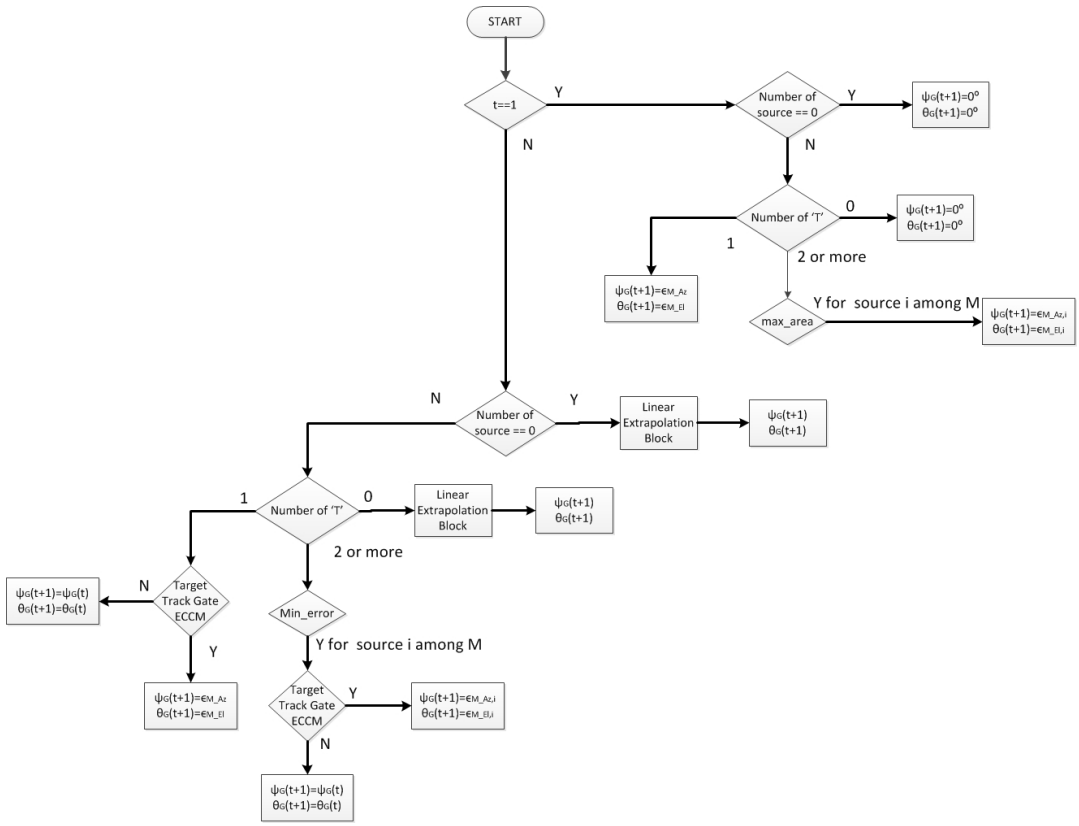

Figure 2.31: Algorithm of Gimbal Model

CHAPTER 3

MISSILE GUIDANCE LAW AND KINEMATIC MOTION MODEL

3.1 Introduction

A guided missile system is defined as a group of components that measures the position of its target and changes the missile flight path towards it in accordance with a guidance law. A guided missile system consists of a seeker, a guidance law, an autopilot and airframe subsystems as shown in Figure 3.1. First of all, the seeker measures the position (LOS angle or LOS angle rate) of the target. Then, the guidance law generates desired acceleration commands and sends this information to the autopilot. Next, the autopilot generates, in accordance with the chosen autopilot type, actual fin deflections or actual accelerations while maintaining the stability of the missile. Thanks to the information generated by the autopilot, missile airframe moves towards target to achieve its main purpose which is hitting the target [25], [26], [5], [27].

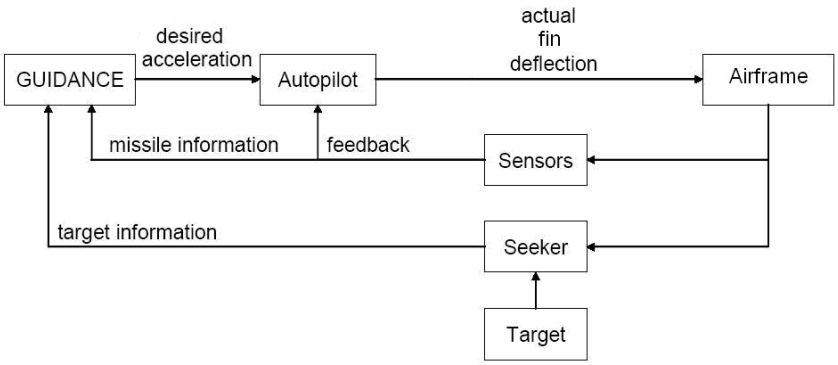

Figure 3.1: Components of IR Guided Missile

In this study, an IIR seeker model, that is the main component of the missile, has been discussed in Chapter 2. Using the IIR seeker, angular position of the target is determined in azimuth and elevation angles, and this information is sent to the guidance law block. Required acceleration commands are sent to the mathematical model of the missile in the simulator. In the simulator, the missile has only a kinematic model with the point mass assumption. All these models will

be explained in detail in the following sections in this chapter. However, coordinate systems and general 6-DOF equations of motion are explained in first, because of comprehending the modeling of not only the missile but also the target is important which is also described here Chapter 4.

3.2 General 6-DOF Equations of Motion

In this study, target has dynamic motion and missile has kinematic motion. Thus, it is requirement to derive equations of motion which describe the behavior of system in terms of rotational and translational motion with respect to time.

3.2.1 Coordinate Systems

There are too many coordinate systems to define vehicle translational and rotational information. The basic coordinate systems are body-coordinate, earth-fixed coordinate, stability-coordinate and wind-coordinate systems. All these reference coordinate systems are right handed and have orthogonal axes as shown in Figure 3.2 [2], [28].

3.2.1.1 Body-Coordinate System

The origin of the body-coordinate system is center of mass of vehicle. X_B axis is called roll axis and points forward through the nose of the vehicle. Y_B axis is called pitch axis and points through the right wing of the vehicle. Finally, Z_B axis is called yaw axis and points downwards. The entire system rotates and moves with the vehicle [28].

3.2.1.2 Earth-Fixed Coordinate System

In earth-fixed coordinate system, Z_E axis points to the center of earth, Y_E axis points to the North. Thanks to the right hand rule, Y_E axis points towards East. This coordinate system is useful for translation and rotation of vehicles [27].

3.2.1.3 Stability-Coordinate System

Usually, the direction of the nose (X_B axis) of the vehicle does not align with the direction of the oncoming air when the vehicle is moving. The difference between the angle of nose of the vehicle and oncoming air is called the angle of attack (α). Thus, there is no change at Y_B and Y_S axes. However, because of the definition of angle of attack, there are perturbations at X_B - Z_B plane with respect to the stability flight axis X_S - Z_S of the vehicle. The stability-coordinate system is used to get the X_B axis aligned with the oncoming flow direction [29].

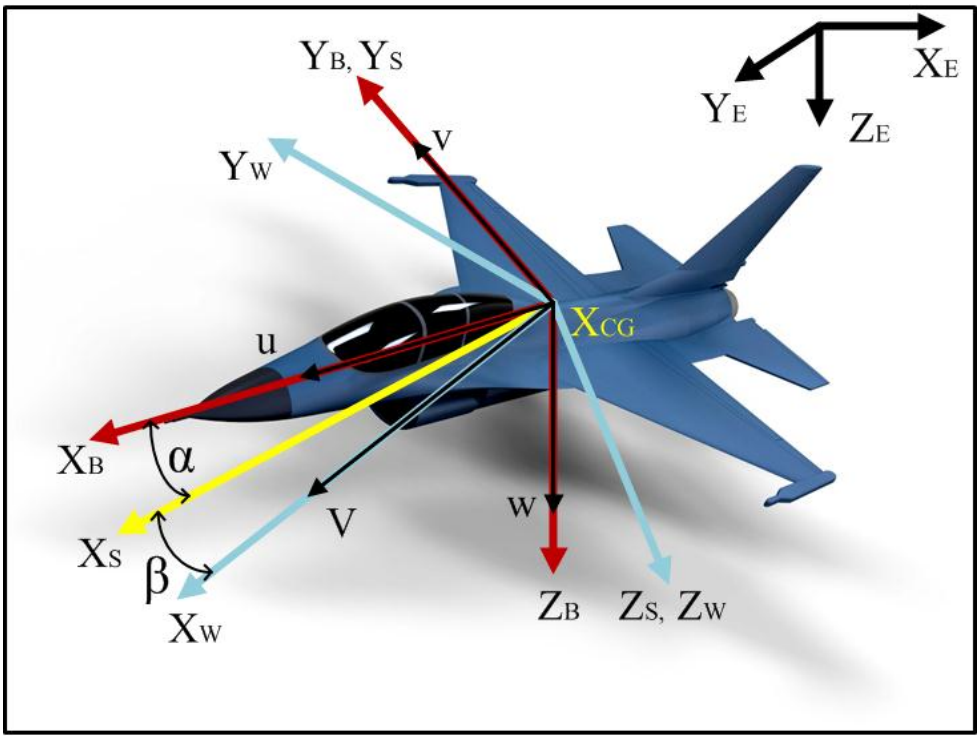

Figure 3.2: Coordinate Systems

3.2.1.4 Wind-Coordinate System

Wind-coordinate system is defined rotation around Z_S axis because of lift, drag and side forces effects over vehicle. This rotation angle is called side-slip angle (β).

3.2.2 Transformations between Coordinate Systems

The vehicle orientation with respect to the earth-fixed coordinate system is defined by yaw (ψ), pitch (θ), roll (ϕ), i.e., the Euler angles. Transformation from earth-fixed coordinate to body-coordinate is constructed with these angles. This transformation is shown by equation 3.1, where, T_B and T_E, T_{BE} refer to body-coordinate, earth-fixed coordinate and transformation matrix from earth-fixed coordinate to body coordinate respectively [27].

$$T_\phi = \begin{bmatrix} 1 & 0 & 0 \\ 0 & cos(\phi) & sin(\phi) \\ 0 & -sin(\phi) & cos(\phi) \end{bmatrix}$$

$$T_\theta = \begin{bmatrix} cos(\theta) & 0 & -sin(\theta) \\ 0 & 1 & 0 \\ sin(\theta) & 0 & cos(\theta) \end{bmatrix}$$

$$T_\psi = \begin{bmatrix} cos(\psi) & sin(\psi) & 0 \\ -sin(\psi) & cos(\psi) & 0 \\ 0 & 0 & 1 \end{bmatrix} \tag{3.1}$$

$$T_{BE} = T_\phi . T_\theta . T_\psi$$

$$T_B = T_{BE} . T_E$$

Transformation from earth-fixed coordinate to body coordinate is completed at three steps. Firstly, earth-fixed information transformed with yaw angle. This transform causes rotation towards right side at Z_E. Secondly, pitch angle transformation causes rotation upper side at new Y_E axis. Finally, roll angle transformation is occurred. This transformation causes rotation at new X_E. [27], [26]

Transformation between body-coordinate and stability-coordinate frames is realized by using the angle of attack (α). The final transformation is from stability-coordinate to wind-coordinate frame which utilizes the side-slip angle (β). T_S, T_W, T_{SB} and T_{WS} refer to stability-coordinate, wind-coordinate, transformation matrix from body-coordinate to stability-coordinate and transformation matrix from stability-coordinate to wind-coordinate. Transformations are illustrated in equation 3.2 [27].

$$T_{SB} = \begin{bmatrix} cos(\alpha) & 0 & sin(\alpha) \\ 0 & 1 & 0 \\ -sin(\alpha) & 0 & cos(\alpha) \end{bmatrix}$$

$$T_S = T_{SB} . T_B$$

$$T_{WS} = \begin{bmatrix} cos(\beta) & sin(\beta) & 0 \\ -sin(\beta) & cos(\beta) & 0 \\ 0 & 0 & 1 \end{bmatrix} \tag{3.2}$$

$$T_W = T_{WS} . T_S$$

All these transformation matrices are orthogonal. Thus, their transposes are equal to their inverses. Due to inverse of transformation matrix, sequence of transformation is exchanged as shown equation 3.3 [30].

$$T_{SW} = (T_{WS})^T$$
$$T_{EB} = (T_{BE})^T \tag{3.3}$$
$$T_{BS} = (T_{SB})^T$$

Due to atmospheric and aerodynamic moment effects, angle of attack and side-slip angle deviate from zero degree. Angle of attack and side-slip angles are related with the speed of the vehicle as shown on Figure 3.3. Speed of the vehicle is found as indicated in equation 3.4. Not only the angle of attack, but also the side-slip angle cause perturbations at X_B, Y_B axes, when calculating the velocity component associated with these axis. However, Z_B axis is only affected by the side-slip angle. Calculation of perturbation is shown in equation 3.5. Because of this equation, the angle of attack and the side-slip angle can be calculated whether body-coordinate and velocity of the vehicle are known [3].

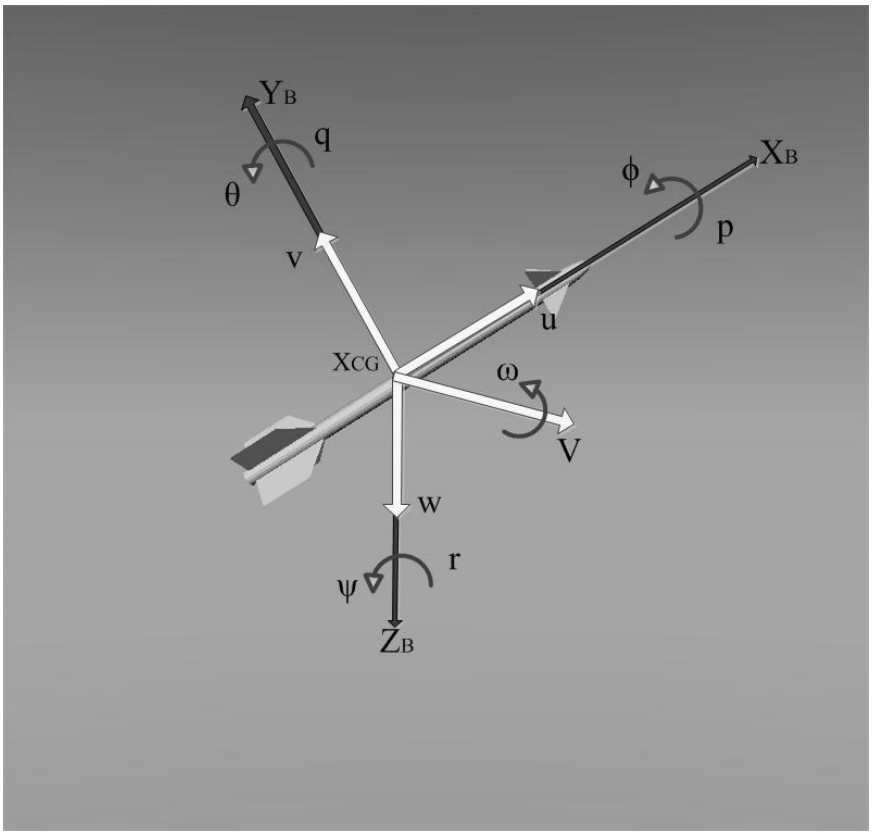

Figure 3.3: Body-coordinate Velocity Components

$$V = \sqrt{u^2 + v^2 + w^2} \tag{3.4}$$

$$\alpha = \frac{w}{u}$$
$$\beta = \frac{v}{V} \tag{3.5}$$

3.2.3 Equation of Motion

Dynamic equations can be derived with Newton's 2^{nd} law. The basic equations (equation 3.6) of this law are the linear momentum and angular momentum equations expressed in the earth-fixed coordinate frame, where, F is the external force, M is the external moment, $\vec{V}$ is the velocity vector in $^{m}/_{sec}$, m is the mass of the vehicle in kg, and h is the angular momentum matrix about the center of gravity in $^{kgm^2}/_{sec}$. When transformating these equations from earth-fixed coordinate frame to the body-coordinate frame, equation 3.7 is obtained, where, ω is the angular velocity vector in $^{rad}/_{sec}$ [26].

$$F = \frac{d}{dt}(m\vec{V})$$
$$M = \frac{d}{dt}(h) \tag{3.6}$$

$$F = \frac{\delta}{\delta t}(m\vec{V}) + \omega \times (m\vec{V})$$
$$M = \frac{\delta}{\delta t}(h) + \omega \times h \tag{3.7}$$

These derivations are performed using some assumptions.
Assumption 1 The vehicle is assumed as a rigid body. Thus, the mass, the size and the shape are all constant during simulations.
Assumption 2 The vehicle is assumed to be symmetric at X_B - Z_B axis. As a result, I_{YZ} and I_{XY} cross products of inertias are equal to zero.
Assumption 3 External applied moments are not affected by gravity because of uniform gravity over the vehicle. At the same time, center of gravity and center of mass are coincident.
Assumption 4 Thrust force is only along X_B axis. Thus, there is no nozzle control in the missile model.

Velocity and angular velocity in equation 3.7 can be expressed as in equation 3.8, where, u, v and w are body velocity and p, q and r angular velocities at body-coordinate. When these velocity and angular velocity equations are substituted at the force equation (equation 3.7), thanks to **Assumption 1**, equation 3.9 is obtained. F_X, F_Y and F_Z indicate the external applied forces. Similarly, angular momentum matrix, which is shown in equation 3.10, is substituted at the momentum equation (equation 3.7) with **Assumption 2**. As a result, equation 3.11 is obtained, where, h_{eng} is the engine angular momentum effect. M_X, M_Y and M_Z indicate the external applied moments [27], [26].

$$\vec{V} = u\vec{i} + v\vec{j} + w\vec{k}$$
$$\vec{\omega} = p\vec{i} + q\vec{j} + r\vec{k} \tag{3.8}$$

$$
\begin{aligned}
F_X &= m(\dot{u} + qw - rv) \\
F_Y &= m(\dot{v} + ru - pw) \\
F_Z &= m(\dot{w} + pv - qu)
\end{aligned} \tag{3.9}
$$

$$
h = \begin{bmatrix} I_X & 0 & -I_{XZ} \\ 0 & I_Y & 0 \\ -I_{XZ} & 0 & I_Z \end{bmatrix} \omega + \begin{bmatrix} h_{eng} \\ 0 \\ 0 \end{bmatrix} \tag{3.10}
$$

$$
\begin{aligned}
M_X &= \dot{p}I_X - \dot{r}I_{XZ} + qr(I_Z - I_Y) - pqI_{XZ} \\
M_Y &= \dot{q}I_Y - pr(I_X - I_Z) + (p^2 - r^2)I_{XZ} + rh_{eng} \\
M_Z &= \dot{r}I_Z - \dot{p}I_{XZ} + pq(I_Y - I_X) + qrI_{XZ} - qh_{eng}
\end{aligned} \tag{3.11}
$$

Total external applied forces over the vehicle are gravity, thrust and aerodynamic forces. Because of **Assumption 4**, thrust is only effective along X_B axis. The total external forces are shown in equation 3.12, where, T is the thrust force in Newton, s is the maximum cross-sectional wing area of the vehicle, $\bar{q}$ is the dynamic pressure, g is te gravity, C_X, C_Y, C_Z are aerodynamic coefficients of F_X, F_Y, F_Z forces, ψ, θ and ϕ are yaw, pitch and roll angles, respectively [26].

$$
\begin{aligned}
F_X &= \bar{q}sC_X - mgsin(\theta) + T \\
F_Y &= \bar{q}sC_Y + mgcos(\theta)sin(\phi) \\
F_Z &= \bar{q}sC_Z + mgcos(\theta)cos(\phi)
\end{aligned} \tag{3.12}
$$

The total applied momentum over the vehicle consists of only the aerodynamic moments. Because, there is no thrust effect on the vehicle due to **Assumption 4**. The total external momentums are shown in equation 3.13, where, c is aerodynamic reference chord, b is the reference wing span, C_l, C_m and C_n are aerodynamic coefficient of moments [26].

$$
\begin{aligned}
M_X &= \bar{q}sbC_l \\
M_Y &= \bar{q}scC_m \\
M_Z &= \bar{q}sbC_n
\end{aligned} \tag{3.13}
$$

The rates of Euler angles are related to the body-coordinate angular velocities. These relationships are shown in equation 3.14 [31].

$$\dot{\phi} = p + qtan(\theta)sin(\phi) + rtan(\theta)cos(\phi)$$

$$\dot{\theta} = qcos(\phi) - rsin(\phi) \tag{3.14}$$

$$\dot{\psi} = rcos(\phi)sec(\theta) + qsin(\phi)sec(\theta)$$

The equation 3.9 and the equation 3.12 demonstrate that, there are equivalences about external applied forces. At the same time, there are also equivalences between equation 3.11 and equation 3.13. As a result, combining these equations, motion equations are obtained as given in equation 3.15. Integrating the rate of body-coordinate velocities with respect to time, body-coordinate velocities can be calculated. Similarly, body angular velocity can be calculated by integrating rate of body angular velocities. Then these angular velocity values will be substituted in equation 3.14. Finally, Euler angles are calculated by integrating their rates.

$$\begin{gathered}
\dot{u} = \frac{\bar{q}sC_X}{m} - qw + rv - gsin(\theta) + \frac{T}{m} \\
\dot{v} = \frac{\bar{q}sC_Y}{m} - ru + pw + gsin(\phi)cos(\theta) \\
\dot{w} = \frac{\bar{q}sC_Z}{m} - pv + qu + gscos(\phi)cos(\theta) \\
\dot{p}I_X - \dot{r}I_{XZ} = \bar{q}sbC_l - qr(I_Z - I_Y) + pqI_{XZ} \\
\dot{q}I_Y = \bar{q}sbC_m - rp(I_X - I_Z) - (p^2 - r^2)I_{XZ} - rh_{eng} \\
\dot{r}I_Z = \bar{q}sbC_n - pq(I_Y - I_X) - qrI_{XZ} + qh_{eng}
\end{gathered} \tag{3.15}$$

3.2.4 Dynamic Pressure

Dynamic pressure is an important part of aerodynamic force and moment equations. Dynamic pressure is proportional with velocity and air density as shown in equation 3.16. Where, ρ and V refer to air density and velocity of vehicles. Air density is a function of altitude (H) of the vehicle. ρ_0 refers to sea level air density, which is $1.223\ {}^{kg}/_{m^3}$ [3].

$$\bar{q} = \frac{\rho V^2}{2}$$

$$\begin{gathered}
if\ H \leq 10000meters \Longrightarrow \rho = \rho_0(1 - 00002256H)^{4.256} \\
if\ H > 10000meters \Longrightarrow \rho = 0.412e^{-0.000151(H-10000)}
\end{gathered} \tag{3.16}$$

3.3 Missile Guidance Law

Purpose of guidance is to generate appropriate reference accelerations to the missile autopilot for the purpose of steering or be steered to a target. Missile guidance can be done using two different approaches for guidance. In the first approach, a missile has its own guidance system.

This system contains the seeker so as to measure the target position. Missiles having this type of guidance are called fire-and-forget type. Usually, Proportional Navigation Guidance (PNG) and its derivatives are chosen as the guidance method for these type of missiles. In the second approach, guidance method is the command type at which missile needs the position of the target and in some cases its own position or guidance commands so as to track the target. This system does not contain a seeker. Information about the position of the missile is supplied by off-board systems such as launcher, illuminator. Because of requiring off-board systems, this type guidance law is not effective for long-range missiles. The main examples of this type guidance are CLOS, commanded guidance, beam ridings and 3-points guidance [5], [32].

Due to fact that PNG type guidance law is used, it is explained in short detail. For the other guidance laws you may refer to references [5], [32].

3.3.1 Proportional Navigation Guidance Law

The most widely known and used guidance law is the classical proportional navigation guidance. In this method, the guidance commands are generated as acceleration commands which are directly proportional with the LOS rate and the closing velocity between the missile and the target. Mathematically, PNG can be expressed as in equation 3.17 [33], where, N is a navigation constant which is arranged to be bigger than 2 [5], or it ranges from 3 to 5 [33], so as to obtain acceptable miss distance. V_C is the closing velocity of the missile to the target and $\dot{\lambda}_M$ is the LOS rate of the missile as shown in Figure 2.23. [34]

$$a_c = NV_C\dot{\lambda}_M \tag{3.17}$$

The main purpose of the PNG law is to take the LOS rate identical to zero, which means that the target is on the boresight of the missile. When LOS rate is zero, there is no lateral and longitudinal acceleration and the missile direcly moves towards the target. In Figure 3.4, there is a artificial scenario which includes a missile equiped with the PNG guidance, and a non-maneuvering target. Sight lines indicate LOS angles. After missile completes its maneuver, LOS rate is identical to zero while target is on the boresight of the missile. As a result, homing missile completes its maneuver towards target quickly and reaches the target in a shorter time than other type of missiles which are not equipped with PNG or its derivatives.

PNG can be classified with respect to direction of generated acceleration commands. If the generated acceleration command is perpendicular to LOS direction, this guidance is named as Pure PNG. However, if the generated acceleration command is perpendicular to the velocity direction of the missile, this derivative PNG guidance is named as the True PNG as shown in Figure 3.5 [35].

LOS rate can be measured by the seeker of tactical radar guided missile and IR guided missile. In addition, closing velocity component can also be measured by a radar guided missile thanks to Doppler radar. IR guided missile cannot measure closing velocity. In some IR guided missile seeker applications, closing velocity is estimated [36] or taken as constant [27],[30].

Within the scope of this study, V_C is taken as constant, 200 $^m/_{sec}$. The reason of why this value is chosen is that modeled target maneuvers at 150 $^m/_{sec}$; at the same time modeled missile's average velocity is approximately 500 $^m/_{sec}$ in 12 seconds flight. However, the

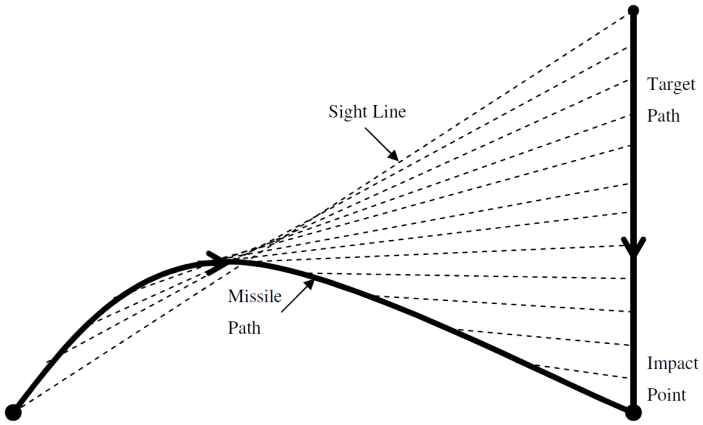

Figure 3.4: Proportional Navigation Guidance Law

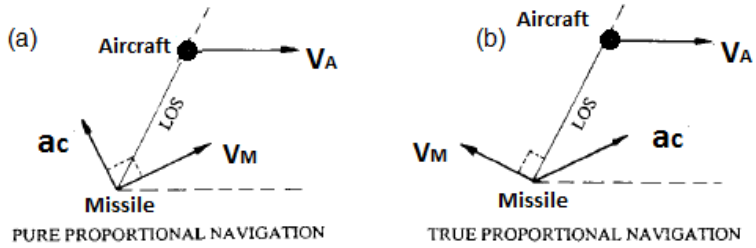

Figure 3.5: PNG Derivatives (a) Pure PNG, (b) TPNG

most of the artificial scenarios last 5 or 6 seconds with respect to maneuvers of the target and initial positions of target and missile. The mean velocity of the missile in this time interval is approximately equal to 315 $^{m}/_{sec.}$ The difference between target and missile velocity is approximately identical to 200 $^{m}/_{sec.}$

Modeled IR seeker outputs are azimuth and elevation angular positions of the tracked target with respect to seeker boresight line. Then, these angular error values (ϵ_M at Figure 2.23) are summed with seeker boresight angles ($\theta_{boresight}$ as shown in Figure 2.23). As a result, LOS angles of missile (λ_M) are determined. The rates of LOS angles for both vertical ($\dot{\lambda}_{M_{el}}$) and horizontal ($\dot{\lambda}_{M_{az}}$) axes are computed numerically.

Equation 3.18 shows the horizontal and vertical acceleration commands generated by 3D guidance law [37]. N navigation constant is set to 3.1 in this study because of minimum miss distance among different N values. At the same time, G level of the missile is also limited by $\pm 50G$.

$$a_H = NV_C\dot{\lambda}_{M_{az}}$$
$$a_V = NV_C\dot{\lambda}_{M_{el}} \tag{3.18}$$

In addition to these, pure PNG law is chosen in this study. Thus, generated horizontal and vertical acceleration commands are perpendicular to missile velocity. To calculate 3D accelerometer components, azimuth and elevation angles of missile velocity vector are required. Essentially, missile velocity vector azimuth and elevation angles are measured by sensors. In this study, angular information about the velocity of the missile is calculated trigonometrically as shown in equation 3.19, where, $\psi_{M_{velocity}}$ is azimuth angle of missile total velocity in radians, $\theta_{M_{velocity}}$ is elevation angle of missile total velocity in radians, $V_{M_{Xtotal}}$, $V_{M_{Ytotal}}$ and $V_{M_{Ztotal}}$ are total velocity components of the missile in $^{m}/_{secs}$.

$$\psi_{M_{velocity}} = tan^{-1}\frac{V_{M_{Xtotal}}}{V_{M_{Ytotal}}}$$
$$\theta_{M_{velocity}} = tan^{-1}\frac{V_{M_{Ztotal}}}{\sqrt{V^2_{M_{Xtotal}}+V_{M_{Ytotal}}}^2} \tag{3.19}$$

Azimuth and elevation angles of the missile are identical to launching angles of the missile, while missile is launched. There is a restriction that missile launching elevation angular is limited with maximum 60^o as well. 3D accelerometer components are calculated with given acceleration commands and azimuth and elevation angles of the missile velocity as shown in equation 3.20, where, a_{M_X}, a_{M_Y} and a_{M_Z} are acceleration components generated by the guidance law in $^{m}/_{sec^2}$.

$$a_{M_X} = a_H sin(\psi M_{velocity})$$
$$a_{M_Y} = a_H cos(\psi M_{velocity}) \tag{3.20}$$
$$a_{M_Z} = -a_V cos(\theta M_{velocity})$$

3.4 Missile Kinematic Motion Model

Missile kinematic motion model, which moves the missile towards a target with given inputs, is just as important as the seeker and the guidance models of the missile. Kinematic model of a point mass missile is discussed in this study. Thus, there is no aerodynamic effects on the missile. At the same time, there is no perturbations along axes. Angle of attack (α) and side slip angle (β) are identical to zero because of this assumption.

The inputs of 3D kinematic motions are accelerations generated by the guidance law, total velocity component of missile and position of missile. In addition to these inputs, thrust vector which propels the missile is required. However, instead of the thrust force, velocity profile with respect to time is generated. Generated profile provides some conditions. These are:

- Missile initial launched velocity is 25 $^{m}/_{sec}$,

- Maximum reachable velocity of missile 800 $^{m}/_{sec}$,
- Mean velocity of missile is 580 m/sec and
- Thrust force accelerates the missile only for 8 seconds. After this time, missile slows down.

In the light of these conditions, generated velocity profile is shown on Figure 3.6. Velocity profile consists of only the magnitude of the velocity with respect to time. 3D components of velocity profile are also calculated with azimuth and elevation angles of the velocity. The calculation of 3D component velocities generated by thrust force are shown in equation 3.21 respectively, where, V_p is the velocity generated by the thrust force in $^{m}/_{sec}$, t is the simulation time in secs and V_{M_X}, V_{M_Y} and V_{M_Z} are velocity components generated by the thrust force in $^{m}/_{sec}$.

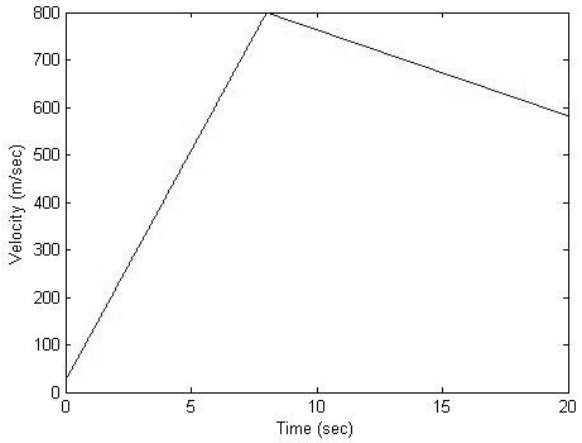

Figure 3.6: Velocity Profile of Missile

$$
\begin{aligned}
V_{M_X} &= V_p(t)cos(\psi_{M_{velocity}})cos(\theta_{M_{velocity}}) \\
V_{M_Y} &= V_p(t)sin(\psi_{M_{velocity}})cos(\theta_{M_{velocity}}) \\
V_{M_Z} &= -V_p(t)cos(\theta_{M_{velocity}})
\end{aligned}
\tag{3.21}
$$

Total velocity includes velocity generated by thrust force and velocity generated by the guidance law. The sum of these velocities gives the total velocity as shown in equation 3.22, where, dt is the simulation step time in sec.

$$
\begin{aligned}
V_{M_{Xtotal}} &= V_{M_X} + a_{M_X}dt \\
V_{M_{Ytotal}} &= V_{M_Y} + a_{M_Y}dt \\
V_{M_{Ztotal}} &= V_{M_Z} + a_{M_Z}dt
\end{aligned}
\tag{3.22}
$$

The last step for motion model of the missile is to calculate the position of the missile as shown in equation 3.23.

$$\begin{aligned} X_M(t+1) &= X_M(t) + V_{M_{Xtotal}} dt \\ Y_M(t+1) &= Y_M(t) + V_{M_{Ytotal}} dt \\ Z_M(t+1) &= Z_M(t) + V_{M_{Ztotal}} dt \end{aligned} \tag{3.23}$$

CHAPTER 4

TARGET MODEL

4.1 Introduction

In this chapter, 6-DOF non-linear dynamic model of the target and 3D IR signature of the target model are explained. To analyze and test surface-to-air IIR missile with an FPA detector in performance, a simulator is required to represent the maneuvers of the aircraft and the 3D infrared signature model. The F-16 fighting falcon aircraft is chosen for the target model. To satisfy higher model fidelity of the simulator and artificial scenarios, a 6-DOF non-linear dynamic model of the F-16 aircraft is customized and constructed. In order to obtain its IR signature, the F-16 aircraft is divided into sub-targets which have different temperature zones and radiometric properties.

4.2 6-DOF Non-linear Dynamic Target Model

For the target model, MATLAB - SIMULINK based 6-DOF F-16 fighter aircraft is obtained. The given mathematical aircraft model uses the NASA-Langley wind-tunnel tests wind-tunnel data on a scale model of an F-16 airplane. The data is applied to the speed up to 1 Mach, and were used in simulations to obtain the maneuvering and stall/post-stall characteristics of a relaxed static-stability airplane. F-16 mass and geometric model, which is used at this target model, is given on Table 4.1 [28].

4.2.1 State and Control Surface Parameters

The non-linear model of the aircraft requires four control surfaces and 13 state parameters to calculate the trimmed output for states and control surfaces. The trimmed state and control values are fed to the F-16 SIMULINK model and 19 different state and flight data are generated during aircraft flight. Input states and control surface parameters are shown at the Table 4.2 and Table 4.3 respectively. Throttle setting is in the range from 453.6 - 8620 kg. As the output of the model, derivatives of input states, normal acceleration (a_n), lateral acceleration (a_{Lat}), dynamic pressure ($\bar{q}$), mach number of aircraft ($M_{aircraft}$), pitch rate (q), angle of attack (α) and velocities referenced at earth-fixed coordinate are calculated [38].

In this study, to satisfy the requirements of the target model, aircraft had better maneuver more than once. For the first maneuver, user gives initial state parameters and control surface pa-

Table 4.1: Mass and Geometric Model of F-16 Aircraft

Parameter	Symbol	Value
Aircraft Mass (kg)	m	9295.44
Reference Wing Span (m)	b	9.144
Maximum Crosssectional Reference Wing Area (m^2)	s	27.87
Roll Moment of Inertia (kgm^2)	I_X	12874.8
Pitch Moment of Inertia (kgm^2)	I_Y	75673.6
Yaw Moment of Inertia (kgm^2)	I_Z	85552.1
Cross Product Moment of Inertia (kgm^2)	I_{XZ}	1331.4
Cross Product Moment of Inertia (kgm^2)	I_{YZ}	0
Cross Product Moment of Inertia (kgm^2)	I_{XY}	0
Cross Product Moment of Inertia (kgm^2)	I_{XY}	0
Center of Gravity Location (m)	X_{CG}	0.3c
Reference Center of Gravity Location (m)	X_{CG_r}	0.35c
Engine Angular Momentum (kgm^2/sn)	H_{eng}	216.9

Table 4.2: Input - State Parameters

Symbol	Description	Unit
V	True velocity	($^m/_{sec}$)
α	Angle of Attack	(rad)
β	Side-slip angle	(rad)
ϕ	Roll angle	(rad)
θ	Pitch angle	(rad)
ψ	Yaw angle	(rad)
p	Roll rate	($^{rad}/_{sec}$)
q	Pitch rate	($^{rad}/_{sec}$)
r	Yaw rate	($^{rad}/_{sec}$)
X_E	North displacement	(m)
Y_E	East displacement	(m)
Z_E	Altitude displacement	(m)
P_W	Power	- ($percentage$)

Table 4.3: Position and Rotation of Dispensers

ID	Description	Unit	Min	Max
δ_t	Throttle Setting	($-$)	0	1
δ_a	Aileron	(deg)	-21.5	21.5
δ_e	Elevator	(deg)	-25	25
δ_r	Rudder	(deg)	-30	30

rameters. As the initial states for the first maneuver, altitude and velocity values are sufficient to obtain the flight data. For the input state of the next maneuver, output state of the last maneuver, which is already completed, is used by turns. However, all the control surface values should be specified by user for all maneuvers. For this reason, a maneuver vector is created which contains aileron, rudder, elevator and throttle setting parameters for all maneuvers, separately. Thanks to these modifications over the model, aircraft can be maneuver more than once. Thus, aircraft may perform powerful evasive maneuvers against threats.

4.2.2 Trimming State and Control Surface Parameters

The 6-DOF non-linear model requires control surface parameters and initial states so as to obtain flight data for maneuvering the aircraft. First of all, the given parameters should be trimmed for steady-state flight within the of capability of aircraft.

In this model, function of trimming is used to create the steady-state flight for the F-16 aircraft. Free control surface parameters are trimmed so as to supply initial states specified by user. Before initial states are supplied, trimming function is run. For each run, free parameters are adjusted and cost function which is the difference between desired initial state and output state values of trimming function is calculated. To stop the iteration, either the cost function should be minimized to a desirable level or the maximum number of iterations which is 5000, should be reached. In order to converge quickly to the initial state parameters, trim function must be started with a well-chosen initial guess of free parameters. This well–chosen initial guess values are $4700\ kg$ for throttle setting, -1 degree for aileron, the other initial guess free parameters are set to zero. These initial free parameters are sufficient to converge to an equilibrium point quickly. The weighted cost function with respect to significance of state parameters associated with the final point of trimming function is shown in equation 4.1.

$$J(\dot{\tilde{x}}) = w_1\dot{V}^2 + w_2\dot{\alpha}^2 + w_3\dot{\beta}^2 + w_4\dot{p}^2 + w_5\dot{q}^2 + w_6\dot{r}^2 \tag{4.1}$$

Throughout the minimization, weight coefficients w_1 to w_6 are chosen as 1, 100, 100, 10, 10 and 10 respectively [38], [27].

4.2.3 Dynamic Equations of F-16 Aircraft

After trimming the initial state parameters, response control surface parameters of the model are generated. These parameters are input for 6-DOF non-linear dynamic motion, which is mentioned at Section 3.2.3, F-16 aircraft model which is modeled by using a SIMULINK and an S-FUNCTION block.

4.2.3.1 Control Surface Parameters

6-DOF non-linear model allows user to control aircraft maneuvers. To accomplish this job, there are four control inputs for each maneuver. These are throttle, aileron, rudder and elevator. Thrust, which is only effective along X_B axis, is controlled by the throttle value which

is between 0 and 1. Thrust force value ranges from $456.3\ kg$ to $8620\ kg$. For the other control surface parameters, the positive deflection causes negative angular rate. Positive aileron causes negative roll rate. Similarly, positive rudder gives negative yaw rate and positive elevator causes negative pitch rate as shown in Figure 4.1 and Table 4.4 [38].

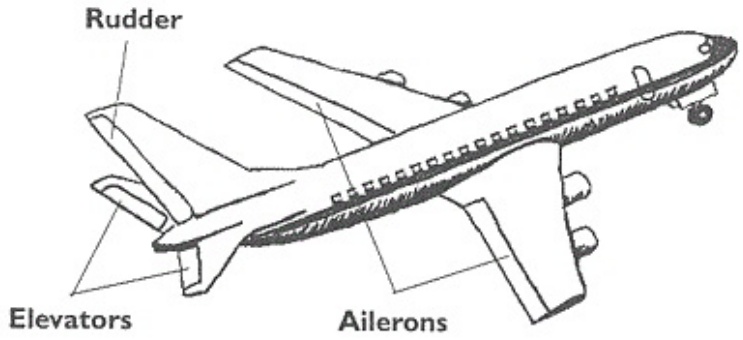

Figure 4.1: Control Surfaces of Aircraft

Aileron, rudder and elevator are controlled by first-order transfer functions. For example, to get the derivative at the sampling instant, elevator input is subtracted from transfer function output. Then subtracted value is multiplied by gain. After, trim value of the elevator value is added to the integration of this derivative of elevator. Each controller has a limiting rate change and a limiting value as shown in Figure 4.2 and Table 4.4 [27].

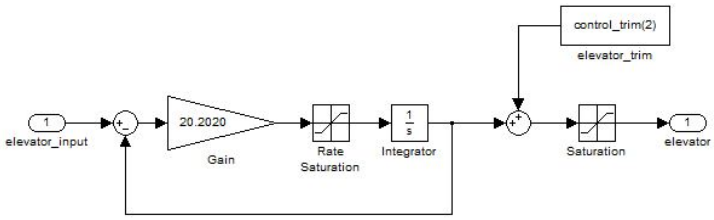

Figure 4.2: Controller of Aircraft Model

Table 4.4: Control Surface Parameters

Symbol	Name	Deflection Limit	Rate Limit	Time Constant	Effect
δ_e	Elevators	$\pm 25\ (deg)$	60 ($^{deg}/_{sec}$)	$0.0495\ (sec)$	Pitch Rate
δ_a	Ailerons	$\pm 21.5\ (deg)$	60 ($^{deg}/_{sec}$)	$0.0495\ (sec)$	Roll Rate
δ_r	Rudders	$\pm 30\ (deg)$	60 ($^{deg}/_{sec}$)	$0.0495\ (sec)$	Yaw Rate

4.2.3.2 Aerodynamic Coefficient and Aerodynamic Model

To calculate total external force and total momentum, aerodynamic coefficients are the critical parameters. These parameters are dependent on not only control surface parameters but also state values. Aerodynamic coefficients are non-dimensional and depend on flow angles (angle of attack (α) and side-slip angle (β)), velocity of aircraft (V), air density (ρ), aircraft angular velocity (p, q and r), control surface deflection angles (δ_t, δ_a, δ_e and δ_r), center of gravity position (X_{CG}) and dimensions of the aircraft (b, s and c). Due to these dependencies, calculation of aerodynamic coefficients is nonlinear and quite complex. To reduce these complex calculations, there are some non-critical assumptions such as ignoring second order effects, independence of longitudinal aerodynamic forces on side-slip angle, rigid body, ignoring angle of attack and side-slip angle rate values, etc. In addition, some parameters are limited. These parameters and their limiting values are shown at the Table 4.5 [27], [28].

Table 4.5: Limited Parameter for Calculation Aerodynamic Coefficient

Symbol	Description	Unit	Min	Max
δ_t	Throttle setting	(kg)	453.6	8620
δ_a	Aileron	(deg)	-21.5	21.5
δ_e	Elevator	(deg)	-25	25
δ_r	Rudder	(deg)	-30	30
α	Angle of Attack	(deg)	-10	45
β	Side-slip angle	(deg)	-30	30
V	Velocity	$(Mach)$	0	1
H	Altitude	$(meter)$	0	15200

In the lights of these information and assumptions there are functions for each force and moment. Aerodynamic coefficients are determined with respect to dependent parameters so that aircraft behavior will be as closly imitated as possible. References [39], [28] explain in detail about calculating the aerodynamic coefficients for the F-16 aircraft.

4.2.3.3 Engine Model

The total external applied force along X body-coordinate axis (equation 3.12) is dependent on the thrust vector which is generated by a single afterburning turbofan jet engine. Engine has also angular momentum effects over the aircraft and this effect is added on angular velocities as shown in equation 3.15. In the F-16 aircraft engine model, engine angular momentum is assumed to be constant; (H_{eng} is set to 216.9 $^{kgm^2}/_{sec}$) and only effects along the X body-coordinate axis [39], [28].

Engine commanded power (P_c) is normalized between 0 and 100. This calculation is related with the throttle setting (δ_t), which is normalized between 0 and 1. Equation 4.2 shows the relationship between commanded power of engine and throttle setting. Commanded power term is the percentage ($0 - 100$) of total power of F-16 aircraft [39], [28].

$$
\begin{aligned}
if\ \delta_t \leq 0.77 \implies P_C(\delta_t) = 64.94\delta_t \\
if\ \delta_t > 0.77 \implies P_C(\delta_t) = 217.38\delta_t - 117.38
\end{aligned}
\tag{4.2}
$$

Engine power level dynamic response is modeled using a first order lag with the time constant (ζ_{eng}) computed by equation 4.3. Actual engine power derivatives ($\dot{P_A}$) are calculated using the difference between commanded power and actual engine power (P_A) with respect to time constant as shown in equation 4.4. Actual power term is given as the percentage of total power as well [39], [28].

$$
\begin{aligned}
if\ P_C \geq 50\ and\ P_A \geq 50 \implies {}^{1}/_{\zeta_{eng}} = 5 \\
if\ P_C \geq 50\ and\ P_A < 50 \implies {}^{1}/_{\zeta_{eng}} = {}^{1}/_{\zeta_{eng}}{}^{\star} \\
if\ P_C < 50\ and\ P_A \geq 50 \implies {}^{1}/_{\zeta_{eng}} = 5 \\
if\ P_C < 50\ and\ P_A < 50 \implies {}^{1}/_{\zeta_{eng}} = {}^{1}/_{\zeta_{eng}}{}^{\star} \\
if\ (P_C - P_A) \leq 25 \implies {}^{1}/_{\zeta_{eng}}{}^{\star} = 1 \\
if\ (P_C - P_A) \geq 50 \implies {}^{1}/_{\zeta_{eng}}{}^{\star} = 0.1 \\
if\ 25 < (P_C - P_A) < 50 \implies {}^{1}/_{\zeta_{eng}}{}^{\star} = 1.9 - 0.036(P_C - P_A)
\end{aligned}
\tag{4.3}
$$

$$
\begin{aligned}
\dot{P_A} = \tfrac{1}{\zeta_{eng}}(P_C - P_A) \\
if\ P_C \geq 50\ and\ P_A \geq 50 \implies P_C = P_C \\
if\ P_C \geq 50\ and\ P_A < 50 \implies P_C = 60 \\
if\ P_C < 50\ and\ P_A \geq 50 \implies P_C = 40 \\
if\ P_C < 50\ and\ P_A < 50 \implies P_C = P_C
\end{aligned}
\tag{4.4}
$$

4.2.3.4 Atmospheric Model

Altitude range of F-16 model used in this study is from sea level to 12 km. Speed of sound is related with temperature and temperature is affected by the altitude of the aircraft. Thus, for the high-fidelity model, altitude effects over temperature, air density and speed of sound should be taken into account. For the given altitude (H in meter) of the aircraft from the sea level, air temperature (T in Kelvin), air density (ρ in ${}^{kg}/_{m^3}$) and speed of sound (c_{light} in ${}^{m}/_{sn}$) can be calculated as shown in equation 4.5, where, T_0 is 288.15 K is the temperature, and ρ $1.223{}^{kg}/_{m^3}$ is the air density at he sea level, respectively and g_H is is the gravitational acceleration at height H [3].

$$T = T_0 0.0065h$$

$$\rho = \rho_0 e^{\frac{g}{287.05T}H} \tag{4.5}$$

$$c_{light} = \sqrt{(401.87)T}$$

At the same time, gravity of earth (g_H) which is dependent on altitude level, is calculated with regards to equation 4.6, where, r_e is the mean radius of earth, g_0 is the standard gravitational acceleration and g_H is the gravitational acceleration at height H. Mean radius of earth is $6371\ km$ and standard gravitational acceleration is $9.976\ {}^{m}/_{sec^2}$.

$$g_H = g_0(\frac{r_e}{r_e + H})^2 \tag{4.6}$$

As a result, external applied force and external momentum can be calculated. Then, body-coordinate velocities ($u, v\ and\ w$), body-coordinate roll rate, yaw rate and pitch rate can be calculated as regards to equation sets in Section 3.2.3. Thanks to equation 3.14, Euler angle rates are calculated. Finally, all these rate values are integrated with respect to time using SIMULINK. If necessary, body-coordinate flight data are transformed to earth-fixed coordinates.

Translation and rotation flight data are used at the 3D target model. At the same time, power constant is used to create the 3D model of afterburner of F-16 aircraft.

In order to explain the model more clearly, an example is given below. F-16 aircraft changes 3 different control surface parameters during each maneuvering time. Throttle parameter is set to 0.8 for all maneuvers. Similarly, there are no aileron and elevator deflections. Aircraft maneuvers around the yaw axis with the rudder deflection angle as given in the control surface vector. This maneuver may be titled as the S-maneuver. The earth-fixed coordinate translation of aircraft is shown in Figure 4.3.

$$Maneuver\ Timing\ Vector = M_{TV} = [1\ 3\ 5]\ seconds$$

$$Control\ Surface\ Vector = \begin{bmatrix} 0.8 & 0.8 & 0.8 \\ 0 & 0 & 0 \\ 0 & 0 & 0 \\ -20 & 20 & -20 \end{bmatrix} \tag{4.7}$$

4.3 3D Infrared Signature Model of Target

Military targets, for instance helicopter, aircraft, tanks and ships are made up of different combination of materials. These materials have specific surface temperatures because of aerodynamic effects and positions at body-coordinates. At the same time, all materials have different physical characteristic. While calculating IR radiation emitted from materials, the most crucial parameters are surface temperature and physical characteristic of materials. Physical characteristic of materials are emissivity, reflectivity and transmittance coefficients. These

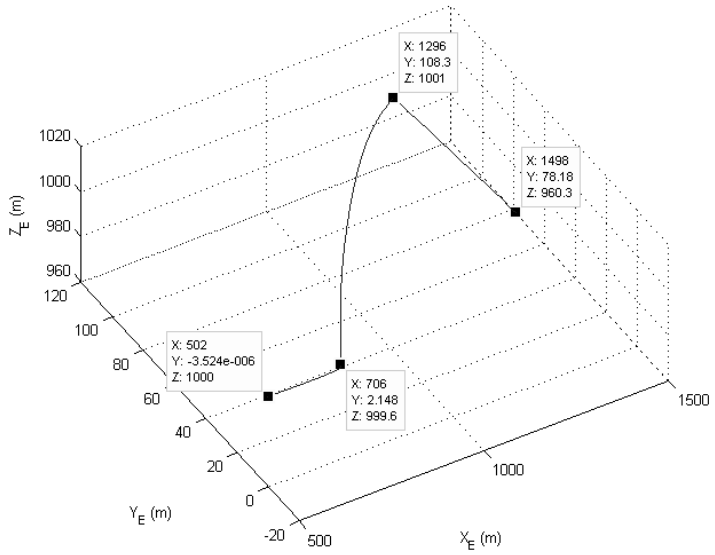

Figure 4.3: S-Maneuver

parameters differ for each material. For this reason, in order to have higher fidelity modeling, 3D IR signature model of the target has different surface temperature zone and all these zones, which are called sub-targets, may have different physical characteristic.

In our case, for the F-16 aircraft, 3D IR signature model has 20 different sub-targets whose actual model development is outside the scope of this study. All sub-targets have (usually) different physical characteristics and temperature zones. In addition, for the 3D design of each sub-target, vertices and polygons are created. Each polygon has three vertices and each vertice has a position with respect to the the center of gravity of the body-coordinate system. Vertices and their positions are fed to the VRML Toolbox of MATLAB, which animates the 3D interactive vector graphics synchronously in cooperation with SIMULINK. IR radiation of each sub-target is calculated with equation 1.3. All translations of sub-targets are represented at body-coordinates, whose origin is the center mass of the aircraft. Euler angles are zero without any rotation at the beginning. Then, using the output of 6-DOF non-linear F-16 dynamic model, translational and rotational information is gathered which is used to transform the 3D IR model at IR scene with respect to the earth-fixed coordinate system.

In the following sections, description, surface temperature and physical characteristics of 20 sub-targets will be examined in some detail, at first. After that, the detailed explanation about how to take vertices and their positions from VRML Toolbox to MATLAB for each sub-target of F-16 aircraft is discussed. Then, emitted radiation of all sub-targets with atmospheric effects will be explained in detail, as well. Finally, transformation of 3D model from body-coordinates to earth-fixed coordinates will be explained.

4.3.1 Information about Sub-Targets

In this study, target is modeled as a combination of sub-target models to satisfy high fidelity model design. In summary, there are 20 different sub-targets; each one has specific physical characteristics and different surface temperatures due to airflow as portrayed in Figure 4.4. Description, emissivity and surface temperatures are explained at Table 4.6. Due to this information, emitted IR radiation of each sub-target is calculated and 3D IR signature of F-16 aircraft is created [9].

Table 4.6: Physical Characteristics and Surface Temperatures of Sub-targets

Description	$\tau(\lambda)$	$\rho(\lambda)(notmodeled)$	$\epsilon(\lambda)$	T (Kelvin)
Left wing under side	0	0.1	0.9	350
Right wing under side	0	0.1	0.9	350
Left wing upper side	0	0.1	0.9	350
Right wing upper side	0	0.1	0.9	350
Right nose	0	0.1	0.9	350
Left nose	0	0.1	0.9	350
Left cockpit	0	0.1	0.9	320
Right cockpit	0	0.1	0.9	320
Right body	0	0.1	0.9	320
Left body	0	0.1	0.9	320
Body inside	0	0.1	0.9	320
Left engine (nozzle)	0	0.1	0.9	400
Right engine (nozzle)	0	0.1	0.9	400
Right vertical stabilizer	0	0.1	0.9	350
Left vertical stabilizer	0	0.1	0.9	350
Vertical stabilizer underline	0	0.1	0.9	350
Left stabilator	0	0.1	0.9	350
Right stabilator	0	0.1	0.9	350
Inner afterburner	0.5	0	0.5	1000
Outer afterburner	0.5	0	0.5	500

Afterburner is a component to sustain high thrust power for mostly supersonic aircraft with a jet engine motor. Pilot can activate or inactivate afterburner in order to takeoff, supersonic flight and combat flight situations. While pilot activates afterburner, afterburner burns a lot of fuel and throws mass into one direction and aircraft accelerates in the opposite direction. Because of hot-burning, afterburner generates plume with high radiation. In this study, afterburner plume is modeled in two steps which are inner and outer plume of afterburner. Inner afterburner plume ($1000\ K$) is much hotter than outer afterburner plume ($500\ K$). Their transmittance and emissivity coefficients are both 0.5. The activation of afterburner is triggered with respect to the percentage power of aircraft motor (P_a). Afterburner radiation level is directly proportional with P_a value. When P_a is identical to zero, there is no radiation emitted by inner and outer plume of afterburner. On the other hand, whether P_a is hundred percent or not, radiation level of afterburner is equal to its maximal value which is calculated with gray body Plank Law as shown in equation 1.3. Linear interpolation is used to calculate the actual power percentages (between zero and hundred percentages). IR signature of afterburner is

created on the IR scene as shown in Figure 4.5 [9].

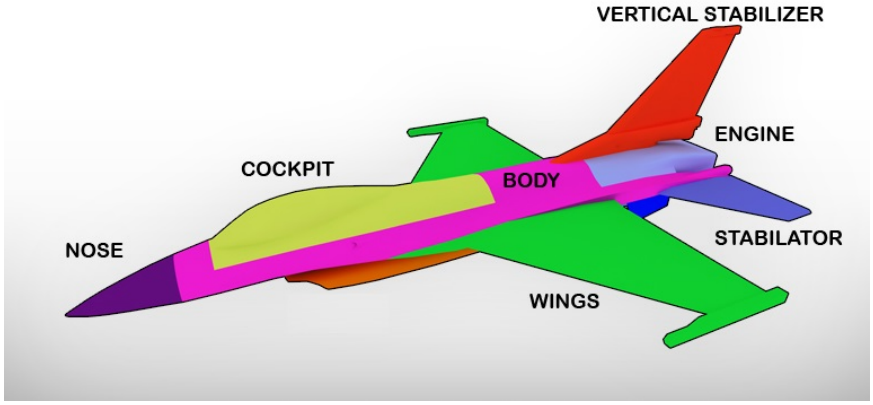

Figure 4.4: Different Surface Temperature Zones of F-16 Aircraft

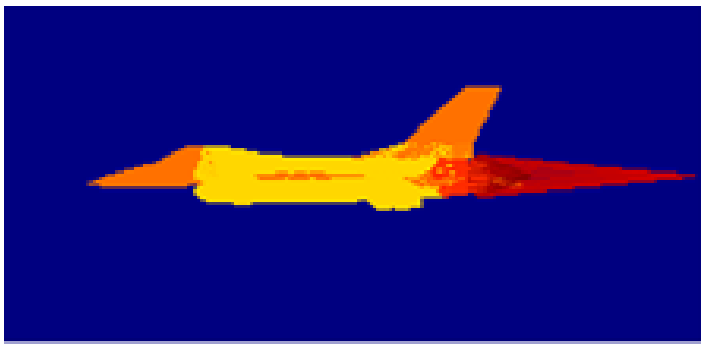

Figure 4.5: IR Signature of Afterburner

3D IR signature model of the target is obtained in terms of surface temperature, transmittance and emissivity values. However, there is an assumption that any sub-target is not a reflective surface. The reason of this is that, modeled IR seeker has a dual-band detector. Spectral bands of detector are $3-5\ \mu m$ MWIR and $8-12\ \mu m$ LWIR band intervals. Even so, the main channel of detector is $8-12\ \mu m$ LWIR. All image processing to estimate position of target candidates, tracking, matching and identification are carried out at $8-12\ \mu m$ spectral band intervals. $3-5\ \mu m$ MWIR is only used for spectral ECCM to determine the radiation ratio. Dominant part of radiation at LWIR band is emissivity. Reflectivity component of radiation is much less than its emissivity component. For these reasons, radiation composed by reflectance may be negligible and modeling of reflectivity for 3D IR signature is not required for $8-12\ \mu m$ LWIR band intervals.

4.3.2 3D Design of F-16 Aircraft

To generate the 3D IR scene from the viewpoint of missile seeker, all scene object's 3D geometries should be modeled. For this purpose, aircraft 3D physical geometry model is generated.

Modeled 3D aircraft is composed of 20 sub-targets, all of whom have different physical characteristics and surface temperatures because of aerodynamic effects as shown at the Table 4.6. As a result of the combination of these sub-targets which has different physical geometries, aircraft 3D model is generated.

For 3D modeling of the F-16 aircraft, VRML Toolbox of MATLAB can be used, which is commonly used for visualization of physical world. It has been selected because of free resource, compatible with MATLAB and SIMULINK. 3D model of F-16 aircraft has been downloaded from Internet. The downloaded files format which is compatible with VRML Toolbox is given in *.wrl* data file. This formatted 3D model file contains indices of vertices which constitute polygons, position of vertices of each polygon with respect to its center of gravity, color and physical characteristics of polygons, translation and rotation information of the model with respect to the earth-fixed coordinates, etc. The downloaded F-16 model composed by 20 sub-targets has too many polygons (Polygons are triangle.) with three vertices. So as to create the 3D model of F-16 aircraft using MATLAB, only the position and indices of vertices are sufficient. However, for MATLAB *fill3* function, this format of model data is not compatible. This problem is solved with a script which converts data from VRML vertice information data format to MATLAB *fill3* function data format. This script is developed as shown Figure 4.6 [40].

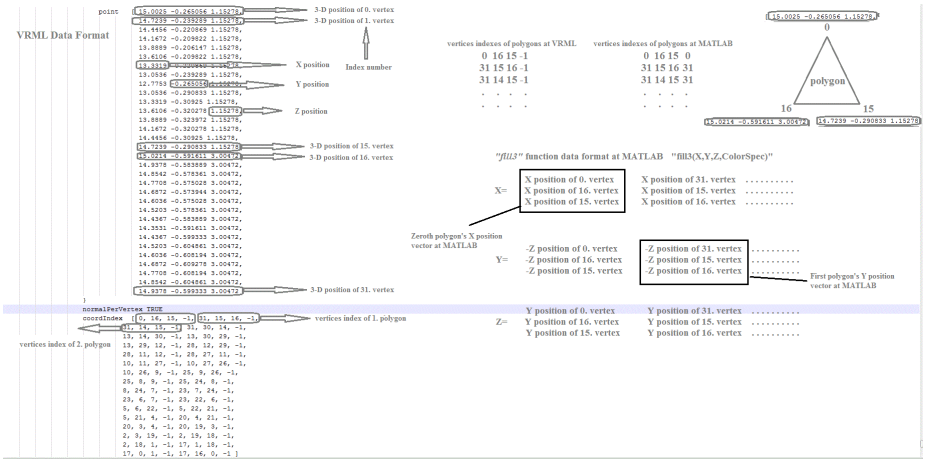

Figure 4.6: VRML *.wrl* File to MATLAB *.m* File Conversion

First of all, vertices' indices of polygons for the chosen sub-target at VRML are converted to MATLAB matrix format by changing -1 at VRML format values with the first value of that row for MATLAB format. Row number of this matrix is equal to the total number of polygons. After that, polygons' vertices and 3D position of vertices are determined. Then, X, Y, Z matrices which include position of each polygon's vertices are created. Total row numbers of X, Y and Z matrices are equal to 3. At the same time, column numbers are equal to total number of polygons for chosen sub-targets. The key part of generating these matrices is that, because of the inconsistency of VRML and MATLAB coordinate systems, Y matrix is filled with –Z position of polygons. Similarly, for the Z matrix, Y values are used. After generating X, Y, Z matrices, interior of 3D polygons are filled with the given color due to *fill3* function. As a result, the 3D F-16 aircraft model geometry is constituted. As stated above, *fill3* function needs the color of polygons to fill as well.

4.3.3 IR Signature of Aircraft

To calculate the total spectral radiance ($L(\lambda, T)$) of F-16 aircraft model, spectral radiation of all sub-targets must be calculated. Plank Law which is given in equation 1.11, is used for the calculation of sub-targets spectral radiance with a given spectral atmospheric transmittance ($\zeta_{atm}(\lambda)$) with respect to missile - aircraft engagement as explained in Section 2.2.2, emissivity coefficient ($\epsilon(\lambda)$) of aircraft and surface temperature (T). Surface temperature and gray body object emissivity coefficient ($\epsilon(\lambda)$) of each sub-target are shown at the Table 4.6.

After the calculation of spectral radiance of each sub-target, in order to color sub-targets with respect to their radiance values, spectral radiance is integrated over given IR spectral band intervals for missile dual-band as shown in equation 2.1, where, L is the radiance values with unit $^{W}/_{sr.cm^2}$, and $(\lambda_1 - \lambda_2)$ are spectral interval bands with unit μm. These bands are taken $8 - 12\ \mu m$ LWIR and $3 - 5\ \mu m$ MWIR because of dual detector spectral responsivities. Our approach to color sub-targets has been explained in detail at IR missile seeker in Section 2.2.4.1. There is an example that demonstrates the 3D IR signature model of the aircraft from the viewpoint of missile seeker as shown in the Figure 4.7.

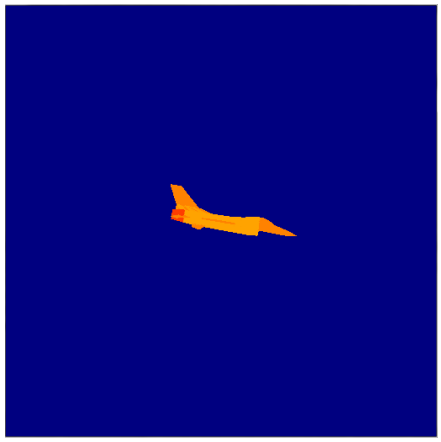

Figure 4.7: 3D IR Signature Model from Viewpoint of Missile Seeker

4.3.4 Transformation of 3D Aircraft Model from Body-Coordinates to Earth-Fixed Coordinates

After the calculation of radiance of sub-models, to generate 3D IR aircraft model from the viewpoint of missile seeker, this model needs to be transformed from body-coordinates to earth-fixed coordinates. Inasmuch as the 3D signature of the aircraft is initially generated at the origin (center of mass of aircraft) of the body-coordinates as shown in Figure 4.8. For this purpose, Euler angles and earth-fixed translation information of the aircraft, which are taken from the F-16 dynamic model, are needed.

Euler angles and earth-fixed position of the aircraft are used to determine the vertices of each sub-target to transform the 3D aircraft from body-coordinates to earth-fixed coordinates. F-16 aircraft has 20 sub-targets and each sub-target has a lot of polygons and vertices. These

transformations must be done for each vertice of polygons of sub-targets.

Transformation of all vertices has 3 steps. First of all, body-coordinate positions of chosen polygons should be transformed with T_{EB} transformation matrix as shown in Figure 4.9. Then, earth-fixed position of the aircraft is added over it to translate polygons to earth-fixed coordinates. Finally, transformed earth-fixed positions of vertice matrices are given to the *fill3* function to generate IR scene as shown in Figure 4.10. All these steps are summarized in the wquation 4.8, where, $k = 1 : 20$ is sub-target number, $j = 1$ to the total polygons number for the chosen sub-target, $i = 1 : 3$ indice number of polygon's vertices. The maximum value is 3 because of triangle polygons, ψ_A is the yaw angle of the aircraft in degrees, θ_A is the pitch angle of the aircraft in degrees, ϕ_A is the roll angle of the aircraft in degrees, T_{EB} is the transformation matrix from body-coordinates to earth-fixed coordinates, X_{BA_v} is vertices positions from center of body-coordinate system along X-axis in meters, Y_{BA_v} is vertices positions from center of body-coordinate system along Y-axis in meters, Z_{BA_v} is vertices positions from center of body-coordinate system along Z-axis in meters, P_{EA} is earth-fixed 3D position of aircraft in meters, X_{EA_v} is earth-fixed position of vertices along X-axis in meters, Y_{EA_v} is earth-fixed position of vertices along Y-axis in meters and Z_{EA_v} is earth-fixed position of vertices along Z-axis in meters.

$$
\begin{aligned}
T_{\psi_A} &= \begin{bmatrix} cos(\psi_A) & -sin(\psi_A) & 0 \\ sin(\psi_A) & cos(\psi_A) & 0 \\ 0 & 0 & 1 \end{bmatrix} \\
T_{\theta_A} &= \begin{bmatrix} cos(\theta_A) & 0 & sin(\theta_A) \\ 0 & 1 & 0 \\ -sin(\theta_A) & 0 & cos(\theta_A) \end{bmatrix} \\
T_{\phi_A} &= \begin{bmatrix} 1 & 0 & 0 \\ 0 & cos(\phi_A) & -sin(\phi_A) \\ 0 & sin(\phi_A) & cos(\phi_A) \end{bmatrix} \\
T_{EB_A} &= T_{\psi_A}.T_{\theta_A}.T_{\phi_A} \\
\begin{bmatrix} X_{EA_v}(i,j,k) \\ Y_{EA_v}(i,j,k) \\ Z_{EA_v}(i,j,k) \end{bmatrix} &= T_{EB_A}. \begin{bmatrix} X_{BA_v}(i,j,k) \\ Y_{BA_v}(i,j,k) \\ Z_{BA_v}(i,j,k) \end{bmatrix} + P_{EA}
\end{aligned}
\tag{4.8}
$$

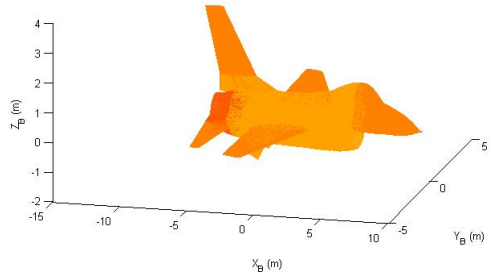

Figure 4.8: Initial Position of 3D IR Signature Model at Body-Coordinate

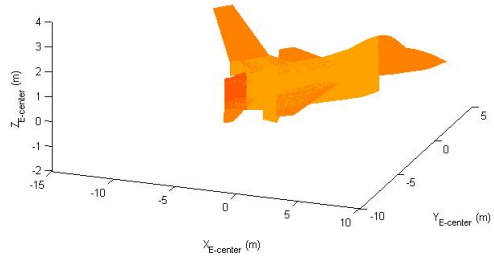

Figure 4.9: Rotated 3D IR Signature Model at Body-Coordinate

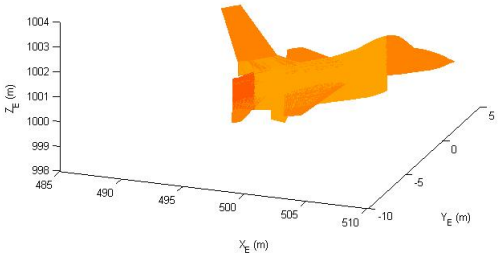

Figure 4.10: 3D IR Signature Model at Earth-Fixed Coordinate

CHAPTER 5

IR ELECTRONIC COUNTERMEASURE

5.1 Introduction

Presently, the prime threat to aircrafts is the IR missile. The majority of deployed missiles use a relatively simple IR seeker, which is able to extract angular information from the received IR signal radiated by an aircraft. However, missiles can be defeated by the selection of appropriate ECM techniques [9].

There are several ways for an IR ECM to defeat an IR missile. In general ECM techniques can be divided into some subcategories such as the pre-launch and the post-launch techniques. Pre-launch ECM techniques are applied before flight. The examples of pre-launch ECM techniques are IR signature suppression, evasive maneuvers, moving fast and using terrain or sea-level to avoid being tracked. IR signature suppression is used for decreasing IR radiation of aircraft. Suppressing heat sources and reducing emissivity of the aircraft by polishing the metal or using coatings are the basic examples of IR signature suppression [9].

After launching the missile towards the aircraft, active and passive ECM techniques are used for post-launch defense. Active ECM techniques, for instance IRCM jammer as shown in Figure 5.1 and directed IRCM as shown in Figure 5.2, are used for breaking the lock of the missile by adding coded and modulated signals to the IR signature of the aircraft so as to jam the seeker of the missile or hard killing the guided missile seeker by transmitting directed high energy signal respectively [7]. AN/AAQ-8, AN-ALQ-144A, AN/ALQ-157, AN-ALQ-204(V) MATADOR and QRC 84-02A are the basic examples of IRCM which are effectively being used at war platforms currently. AN/AAQ-24(V) NEMESIS is an example for directed IRCM [41].

Passive ECM known as flares are dispensed from an aircraft which is the most frequently used aerial ECM to counter IR missiles. Flares are commonly composed of a pyrotechnic composition based on magnesium or another hot-burning metal; with burning temperature equal to or hotter than engine exhaust of the aircraft so as to emit higher radiance than the aircraft. As a result of this action, first and/or second generation IR missiles which have the capability of detecting and estimating target position using AM or FM modulated signals, locks on flares because of its higher radiation on scene [15], [42].

Military aircrafts have a system to dispense flares. This system, which is called CMDS, is also crucial for applying effective ECM techniques because, it is possible to dispense flares from desired dispensers which are located all around the platform and at desired angles. The user

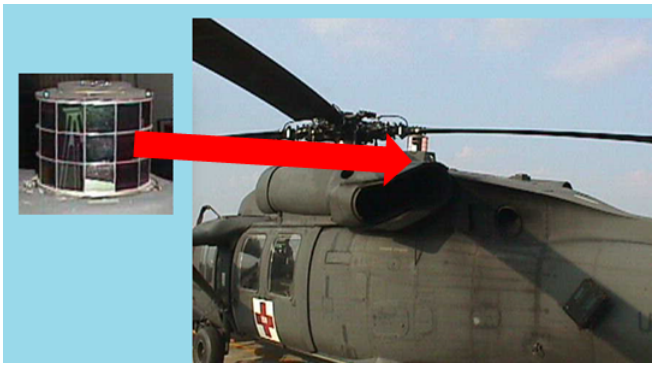

Figure 5.1: IRCM Jammer

Figure 5.2: Directed IRCM

defines the dispensing program which includes dispensing time of flares, choosing a particular dispenser and dispensing velocity in CMDS. Thus, CMDS dispenses flares at an appropriate time with an appropriate dispensing velocity from appropriate dispensers. In general, air platforms have four CMDS dispensers on the platform. All these dispensers are located at the vertices of an aircraft with fixed angle. While flare is dispensed from one of the dispensers, the dispensing angle of the flare and body-coordinate position of the dispensed flare with respect to the target are defined. Thanks to this information, flare motion characteristics can be updated.

In this study, to deceive the IIR missile seeker, MTV and spectral flares are modeled. These flare models contain kinematic motion of flare with gravitation and drag force effects instead of free-fall trajectory. Among the more effective ECM techniques are, flare 3D IR signature and CMDS which has a lot of features such as adjustable dispensing angle, user-defined dispenser

positions, applying flare dispensing programs, simultaneous flare dispensing and decision of flare dispensing time etc. IR signature of flare is time dependent because of limited flare burning time and rising time. To realize this dependency, time function of flare burning and emitting radiation is generated.

5.2 Flares

Flares are initially developed by U.S.A. for protection aircrafts and helicopters from anti-aircraft IR seeker guided missiles which were used at Vietnam War in the 1960s [18]. Flares are inexpensive when compared to other ECM techniques and they are very effective especially with advanced flare technology against IR missiles [9]. In the light of these reasons, flare can be considered as the most effective ECM technique against IR guided missile.

Flares are contained in cartridges at dispensers on aircraft. When they are dispensed, thanks to fire squib of the flare, they can sustain radiance for a few seconds, higher than that of the protected platform [15]. Although the flare is much smaller than the aircraft it is protecting, it radiates significantly more IR energy. As shown in Figure 5.3, the missile tracker tracks the centroid of all of the IR energy within its field of view. Since the flare has more energy, the energy centroid is closer to the flare. As the flare separates from the protected aircraft, the centroid is pulled away. As a result, the aircraft leaves the tracking field of view of the missile, the missile homes on just the flare [42].

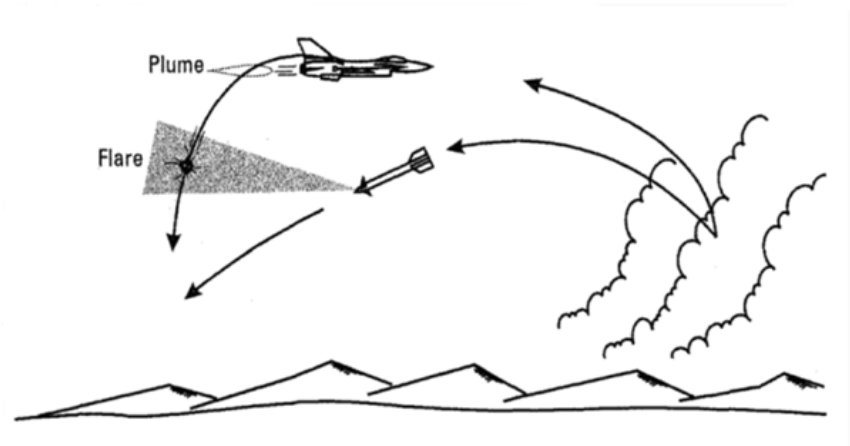

Figure 5.3: Break of Missile Lock

5.2.1 Performance Parameters of Flare

To be effective as an ECM technique, flare must satisfy some requirements. These are;

- Adequately correct aircraft-like signatures to be accepted as target,
- Adequate but balanced intensity to be favored instead of the aircraft,

- Adequately small initial separation to the aircraft,
- Adequately aircraft-like flight-path to be accepted as target,
- Adequate rise-time in order not to activate seeker's rise-time trigger ECCM,
- Adequate coordination with active ECM systems such as IRCM, Directed IRCM,
- Adequate consideration of engagement geometry,
- Adequately long-lived not to require constant ejections,
- Adequate ejection sequence to create optimum effects,
- Adequate size to compete with the target in imaging seekers [18].

At the same time, performance of flare depends on some parameters. These parameters are defined at the beginning phase of flare design as requirement parameters. To deceive a missile, these parameters are highly effective on flare performance. These parameters are explained in the following sections.

5.2.1.1 Emitted Radiance

To break the missile lock on the aircraft, flare should emit higher radiation than the aircraft. As being composed of highly explosive and hot-burning materials, flares radiate higher energy with respect to an aircraft in a limited time duration. However, an advanced missile discriminates flare and an aircraft by comparing the peak radiance values. As a result, even though the main requirement of a flare is to emit higher radiance than an aircraft, there must be a limit on the peak radiance value of flares [9].

5.2.1.2 Rise Time

After dispensed from a moving target, flare trajectory quickly leaves the aicraft. However, flare radiance must reach the required level prior to leaving the missile FOV. At the same time, since flare rise time is very small, flare can damage the aircraft because of its hot-burning metal when it is dispensed from a dispenser. As a result, rise time of a flare should be arranged so that it should be very small to be able to reach its peak before leaving the missile's FOV and not so quick to damage the aircraft [9].

The flare burns longer at higher altitudes; however it takes much time to reach the peak radiance value there. This increase in flare rise time at higher altitudes may increase the effectiveness of the flare.

5.2.1.3 Burn Time

After the ignition of the flare, it continues emitting radiation long enough until it is in missile FOV and to break the track lock of the missile on the aircraft. Ideal minimum burn time is the time elapsed until flare is not within the missile FOV [9].

5.2.1.4 Spectral Response

Spectral characteristics of flare radiation should match with aircraft to deceive missile seeker. Spectral response of conventional flares is not matched with aircraft spectral response. Peak radiance of conventional flare is about $1 - 3\ \mu m$ because of their hot-burning metal (2000 – 2200 K). However, temperature of aircraft surface is approximately 300 K. This means that, peak radiance occurs at $8 - 12\ \mu m$ for the aircraft. As a result, missile with spectral ECCM can discriminate flare and aircraft based on their radiance level ratios [9].

5.2.1.5 Ejection Velocity and Direction

Flare ejection velocity and direction directly affects flare performance. After dispensing, flare should separate from the aircraft not to trigger missile kinematic ECCM. Flare ejection direction affects flare ejection velocity in earth-fixed coordinate directly. At the same time, flare must be dispensed in the optimum direction to be seen by the missile seeker as soon as after the ignition [9].

5.2.1.6 Aerodynamic Effect

Aerodynamic design of flare effects flare separation. Thus, flare must be designed not to separate and not to fall out the missile FOV too rapidly [9].

5.2.2 Types of Flares

Advanced IR threats are capable of flare and target discrimination by applying advanced ECCM techniques, which reduces effectiveness of basic flares. For this reason, advanced flare technology is required to counter with missiles equipped with advanced IR technology. Interestingly, basic flare and advanced flare may show similarities about emitting radiance and motion. At the same time, advanced flares may compose of large radiant cloud and the area of this cloud is supposed to get bigger with time until burn-out time of the flare. Basic and advanced flares are detailed in following sections [20].

5.2.2.1 Conventional Flare

Conventional flares are the first designed as pyrotechnic (pyrotechnic means it is comprised of hot-burning metal and emits visible light). They have been used by U.S.A at Vietnam War to protect helicopters from IR guided missiles [18].

The basic conventional flare is named as MTV such as the M-206 and MJU-7B. MTV flares are pyrotechnic and point source flares. Their peak radiance value, which occurs at $1 - 3\ \mu m$ at IR spectral, is more than that of the host aircraft. They are effective on first generation IR guided missiles such as Redeye and SA-7. First generation guided missile seeker tracks the highest radiation source on scene because of its seeker design. However, for advanced IR missiles, MTV flare may not be an effective ECM technique [9].

MTV flares have some drawbacks as indicated in the literature. These are;

- Point source,
- Hot temperature and higher peak radiance,
- Free-fall or trajectory, slow down quickly and rapidly separate from aircraft,
- Spectral response does not match with its aircraft. [20], [10]

Although MTV flare has disadvantages, it is very cost-effective and expendable. At the same time, with optimum flare dispensing sequence program, MTV flares can be effective against advanced IR missiles.

5.2.2.2 Spectral Flare

Advanced IR missile technology makes missiles not to be deceived by conventional flares. 2^{nd} and 3^{rd} generation IR missiles have advanced seekers with new detectors and new ECCM techniques to make conventional flares obsolete. Underlying of these ECCM is that IR signature of the conventional flare does not match with that of the aircraft IR signature. Thus, advanced ECCM techniques with the help of new seeker technology completely diminishes conventional flare effectiveness [9].

Because of this development of IR missiles, considerable advances in flare technology is required and has been realized. New design flares have their IR signatures matched with aircraft IR signature. At the same time, peak radiance value of the new flare is a little more than aircraft peak emitted radiance. This new design flare is named either as spectral flare or spectral-matched flare. Development of conventional flares depends on advancement at the composition of pyrotechnic materials. Conventional flare has pyrotechnic hot-burning metal reaching temperatures as $2000 - 2200\ K$ while burning. During burning, conventional flare radiates higher energy. Pyrophoric materials are either liquid or solid based materials and ignite instantly upon contact with air. Emitted radiance by pyrophoric materials are less than pyrotechnic material radiation. Some basic examples of pyrophoric materials are compositions based on carbon, boron, silicon, or aluminum. Thanks to these materials, spectral flare radiates similar with target IR signature [9], [43].

For example, the spectral flare of GA9116 has similar relative radiance intensity with that of the aircraft as shown in the Figure 5.4. MTV flare has peak radiant intensity value approximately at $2\ \mu m$. However, spectral bands of aircraft's peak radiant intensities are shown in Figure 5.5. There are no similarities about peak radiant intensity at spectral band between MTV flare and aircraft. Unlike conventional flares, a spectral flare IR signature characteristic is similar with IR signature of the aircraft. Spectral ECCM of 2^{nd} and 3^{rd} generation IR missiles will not trigger with spectral flare.

5.2.2.3 Kinematic Flare

Conventional flares have a significant characteristic such that upon ejection, they rapidly slow down and separate from the aircraft. This rapid motion can be detected by an advanced IR

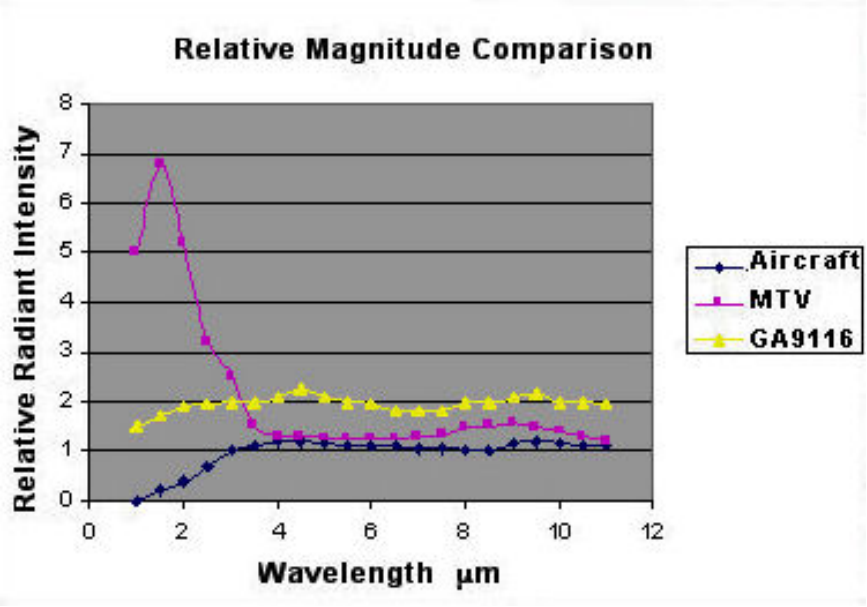

Figure 5.4: Relative Radiant Intensity of Aircraft, GA9116 Spectral Flare and MTV Flare

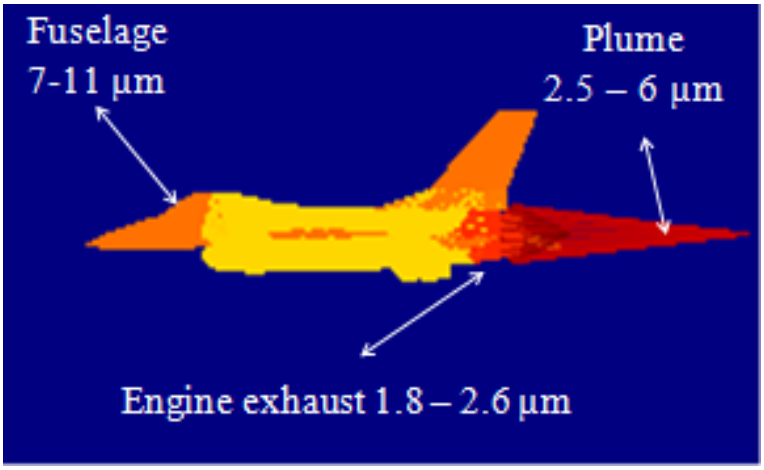

Figure 5.5: Spectral Bands of Peak Radiant Intensities of Aircraft

missile seeker with trajectory discrimination and the missile rejects flare signals. As a result missile lock is not broken. This problem about conventional flares reveals requirement of kinematic flare [20], [10].

Kinematic flares have two varieties. First one has some propellant to direct itself towards the aircraft with applied trust. Second variety has an aerodynamic design to reduce drag force on the flare. Unlike conventional flares, kinematic flares do not rapidly slow down and separate. Thus, kinematic ECCM of missile cannot be triggered by flare motion. The basic example of kinematic flare is MJU-47 which has propellant to simulate the motion of an aircraft [20],

[10] and [43].

5.2.2.4 Spatially Distributed Flares

4^{th} generation IR missiles have seekers with FPA detector arrays. These new technology seekers may discriminate all flares with advanced ECCM techniques such as kinematic, spectral, dual band ratio etc. Conventional, spectral and kinematic flares are not totally effective over 4^{th} generation IR missiles.

The most effective ECM technique for this type of missile is to dazzle or cover its all FOV with large radiating clouds such as spatially distributed flares. For this purpose, spatially distributed flares are developed. The material composition of this new design flares is such that it is a composition of liquid pyrophoric materials which generate much larger radiated area than conventional flares. When dispensing spatially distributed flare, there is a large radiating area thanks to air-stream. If this flare is in missile FOV, missile loses its target and tracking lock of the missile is also broken [20].

5.3 Countermeasure Dispensing System

Countermeasure Dispensing System is necessary for dispensing passive ECM technique flare. This system is constructed as a constitution of some sub-systems. These are safety switch, programmer, control display unit (CDU), sequencer and dispensers as shown in Figure 5.6.

Safety switch provides the safety to prevent the system dispensing flare start working when the aircraft is on the ground. Before taking off, the operator should switch it off. Programmer is the core processor unit and provides the interface between all the related sub-systems. At the same time, programmer receives information from ES system for dispensing flare or applying flare dispensing programs. CDU is on the cockpit and provides an interface to the operator. All input given to system by operators and some outputs for operators are processed at this sub-system. Sequencer applies current for squib to eject the flare. At the same time, sequencer searches for the dispensed flare considering dispensed dispenser, flare type, dispensing time sequences information given by the programmer [44].

Flares are dispensed from same type of dispensers. In general, the capacity of these dispensers is 30 cartridges. All these cartridges can be filled with flare ammunition. Thus, all filled flares have the same geometry. The most common flare and cartridge of dispenser sizes are $2X1X8\,inches$ $(50X25X200\,mm)$ and $1X1X10\,inches$ $(25X25X250\,mm)$ height, width and length respectively [9].

Flare cartridges employ the same type of electrically initiated squib to eject the flare pellet. After ejection, flare is dispensed from the determined dispenser of CMDS. This determination can be programmed with user at the beginning of flight or the system can automatically dispense the flare with respect to the position of threats or maneuvering of the aircraft. After separated from the aircraft, the squib is also used to ignite the flare pellet. After ignition, flare is started to radiate IR energy thanks to hot burning metals such as magnesium which is the main component of conventional MTV flare [15].

AN/ALE-39, AN/ALE-45, AN/ALE-47, ÖZIŞIK CMDSs are some examples which are used

Figure 5.6: AN/ALE-47 CMDS

at aircrafts presently [41].

5.4 IR Electronic Countermeasure Model

In the light of this study, CMDS is modeled with four dispensers which are mounted on the aircraft. At CMDS model, the position and orientation of dispensers can be modified. At the same time, if necessary, user can take out desired dispensers. Another feature of CMDS model is that, there are initiating model for flare dispensing time and initiating model for choosing dispenser. In the following sections, these models will be discussed.

5.4.1 Dispenser Model on CMDS

Flare is the most effective ECM techniques against IR threats, as long as the flare type, dispensing time of flare and dispensing position and orientation should be well chosen. To satisfy these requirements, CMDS dispenser model is developed. In the developed simulator, all these requirements are satisfied thanks to CMDS dispenser model.

F-16 aircraft has need for protection against IR threats. That's why aircraft is equipped with four flare dispensers so as to dispense flare. Properties of dispenser model are specified below.

- Dispensers are located four vertices of aircraft with fixed azimuth and elevation orientation.
- Dispensers have 30 cartridges. Thus, for aircraft, there are totally 120 flare on aircraft.
- Size of cartridges is selected 1X1X10 inches ($25X25X250\ mm$) height, width and length.
- Flare ejection from dispenser has constant initial velocity. Because, electrically initiated squib which initiates flare ejection from cartridges, is same at all flare.

Initial values of parameters at the dispenser model are shown on the Table 5.1, where, X_{BD}, Y_{BD} and Z_{BD} are body-coordinate position of the dispenser, and ψ_{BD} and θ_{BD} are body rotation azimuth and elevation angles of dispenser. However, the user can adjust all these parameters and analyze these effects for performance on artificial scenarios.

In order to apply more effective ECM techniques with flares, there are three major parameters. These are determining the optimum dispensing time sequences, determining the optimum dispenser which is mounted on the aircraft and selection of the dispensed flare types.

Table 5.1: Control and Surface Parameters

Dispenser ID	X_{BD}(m)	Y_{BD}(m)	Z_{BD}(m)	ψ_{BD}	θ_{BD}	Size (mm)
S0 (front-left)	5	-0.75	-0.5	-45^o	-30^o	25X25X200
S1 (front-right)	5	0.75	-0.5	45^o	-30^o	25X25X200
S2 (rear-right)	-4.75	0.75	-0.5	135^o	-30^o	25X25X200
S3 (rear-left)	-4.75	-0.75	-0.5	-135^o	-30^o	25X25X200

5.4.1.1 Flare Dispense Time Selection

In this study, flare dispensing at the desired time is modeled with three different choices. In the basic flare dispensing time model, all time of flare dispensing is given by the operator before the flight simulation. The second model is modeled with respect to aircraft maneuvers timing vector. Flares are dispensed synchronously with maneuver timing vector. The last model depends on the distance between the aircraft and the missile. When this distance is less than a threshold value, flares are dispensed.

Basic Model: In this model, dispensing time sequences of flares are determined with given parameters before the flight simulation. These parameters are initial dispense time, initial delay, burst interval time, burst count, salvo interval time, salvo count and simultaneous dispense. All these parameters are used to generate the flare dispense program which contains total dispensed flare number, all flares' dispense time and dispenser number.

Initial dispense time is the trigger for starting the dispense program. After the dispense program is started, first flare dispense time is delayed by initial delay parameters. Second flare is dispensed after the burst interval time elapses from first flare dispense time. At the first salvo, the burst count time of dispense of flares is recorded. At the end of the first salvo, after the salvo interval time passes, the second salvo is started. At the end of the program, totally dispensed flares are salvo count time burst count. Simultaneous dispense parameter is a Boolean parameter which represents two flare dispenses at the same time synchronously, rather than only one flare dispense at the given time. As a result, with simultaneous dispense totally dispensed flare number is redoubled.

Figure 5.7 shows an example which is about flare dispense program and explanation about associated parameters. Initial dispense time for this example is 0.75 seconds. Similarly, the initial delay is 0.35 seconds. There are 3 salvos 2 burst counts. Simultaneous dispense is true. Thus, there are two similar dispense sub-programs in dispense programs. Salvo interval is set to 1 seconds and burst interval is set to 200 msec. At the end, there is a flare dispense time vector in the second. For this example this vector is:

$$Flare\ Dispense\ Time\ Vector = [1.1\ 1.3\ 2.3\ 2.5\ 3.5\ 3.7\ 1.1\ 1.3\ 2.3\ 2.5\ 3.5\ 3.7] \quad (5.1)$$

Aircraft Maneuver Timing Vector Model: Aircraft maneuvers with a given maneuvers timing vector is a pre-launch ECM technique. This vector contains maneuver starting times.

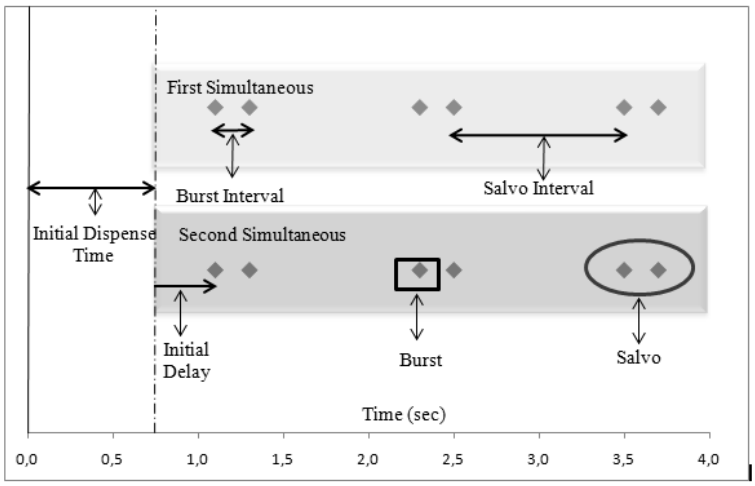

Figure 5.7: Basic Model of Flare Dispenser

Our approach is to combine the effective maneuver and the effective flare dispensing post-launch ECM technique. For this purpose, flare dispense times are arranged with respect to aircraft maneuvers starting time which is in the maneuver timing vector. This model has also some parameters to automatize the flare dispense time determination. These parameters are maneuver timing vector, burst count, burst interval, dispense initiation before maneuver, salvo count, salvo interval and simultaneous dispense. In this model, initial delay, initial dispense time parameters are not used. Unlike the basic model, salvo count and salvo interval is determined with respect to the maneuver timing vector. Salvo count is the size of this vector as shown in equation 5.2. However, salvo interval is determined with respect to dispense initiation before maneuver and maneuver timing vector as shown in equation 5.2. Unlike the basic model, salvo interval is not a constant value. It is a vector which indicates flare dispense time initiations for each maneuver.

$$\begin{gathered} M_{TV} = maneuvers\ timing\ vector \\ Salvo\ Count = size(M_{TV}) \\ t_{DIBM} = dispense\ initiation\ before\ maneuver \\ Salvo\ Interval = [M_{TV}]\text{-}t_{DIBM}.ones(1, Salvo\ Count) \end{gathered} \tag{5.2}$$

Figure 5.8 demonstrates an example, where necessary parameters and their values are shown. Salvo count and salvo interval are calculated with respect to the maneuver. Then, thanks to dispense initiation before maneuver, burst count and burst interval flare dispensing time are determined.

$$
\begin{gathered}
M_{TV} = [1\ 3\ 5] \\
t_{DIBM} = 0.2sec \\
\\
Salvo\ Count = size(M_{TV}) = 3 \\
Salvo\ Interval = [1\ 3\ 5]\text{-}0.2[1\ 1\ 1] = [0.8\ 2.8\ 4.8] \\
Burst\ Count = 2 \\
Burst\ Interval = 0.3sec \\
\\
Flare\ Dispense\ Time\ Vector = [0.8\ 1.1\ 2.8\ 3.1\ 4.8\ 5.1]
\end{gathered}
\tag{5.3}
$$

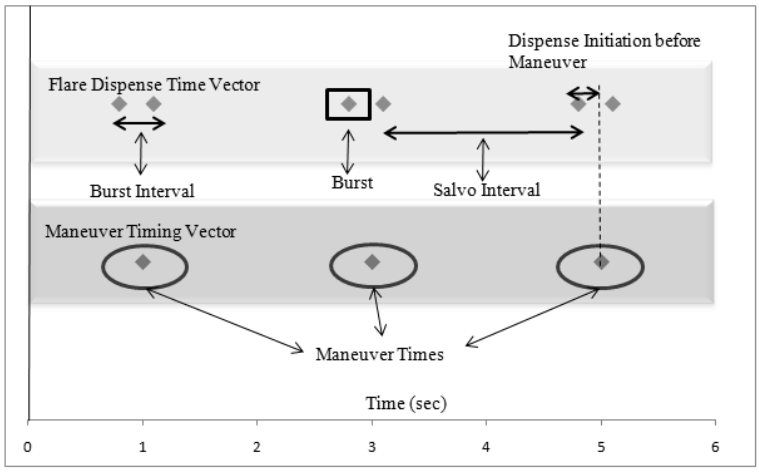

Figure 5.8: Maneuver Timing Vector Model of Flare Dispenser

Distance between Aircraft and Missile Model: The last, flare time selection model is to initiate the flare dispensing with respect to range information between the aircraft and the missile. The main problem here is to measure or calculate the distance information. Most of the IR missile detection systems such as MWS ES system has not the ability to measure the distance information. However, in this study, our assumption is that ES system such as RWR ES supplies this information. This model has only a single parameter different from the basic model. The difference is the initial dispense time parameters. In the basic model, user defines these parameters. However, in this model, the initial dispense time parameter is calculated with respect to the distance between the aircraft and the missile. When range value is smaller than a threshold (T_{Range}), initial dispense time is set. Thus, flare dispense program can adjust as in the basic model except this major difference.

The distance between the aircraft and the missile is calculated with *norm* function of MATLAB as shown in equation 5.4, where, P_{EA} is the 3D position of the aircraft and P_{EM} is the 3D position of the missile in earth-fixed coordinates. If range information is shorter than this range threshold parameter, flare will be dispensed by the dispensing program.

For example, as shown in Figure 5.9, target and missile translation are given and the threshold of range information is set to 245 meters in the simulation ith time. The range between missile

and aircraft is measured as 244.95. Flare dispensing program is initiated because the range is smaller than threshold and initial dispense time (t_{IDT}) is set to 0.75 sec.

$$Distance = norm(P_{EA} - P_{EM}) \tag{5.4}$$

$$\begin{gathered} T_{Range} = 245\ meter \\ P_{EA}(i) = [100\ 200\ 1000] \\ P_{EM}(i) = [0\ 100\ 800] \\ distance(i) = 244.95 \\ \\ time(i) = 0.75sec \\ distance(i)\ <\ T_{Range} \\ t_{IDT} = 0.75\ sec \\ \\ Salvo\ Count = 3 \\ Salvo\ Interval = 1\ sec \\ Burst\ Count = 2 \\ Burst\ Interval = 0.2\ sec \\ Initial\ Delay = 0 \end{gathered} \tag{5.5}$$

$$Flare\ Dispense\ Time\ Vector = [0.75\ 0.95\ 1.95\ 2.15\ 3.15\ 3.35]$$

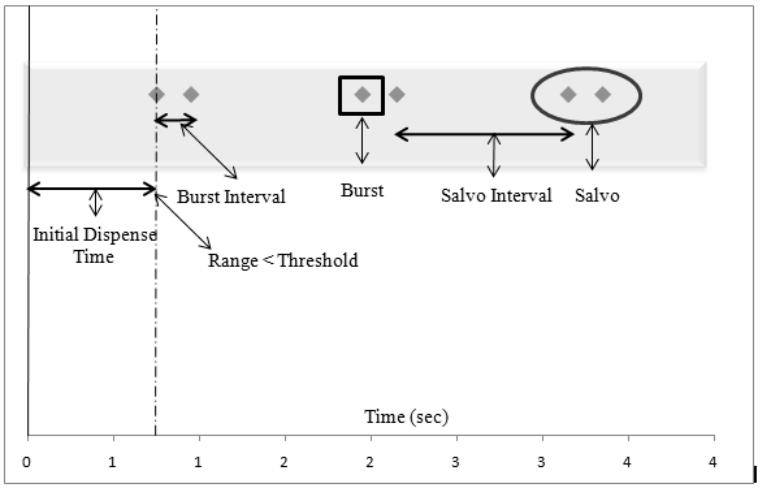

Figure 5.9: Distance Model Model of Flare Dispenser

5.4.1.2 Dispenser Selection

After determining flare dispensing time sequences, the following requirement is to be answered: which dispenser is optimal for dispensing flare question? This question is answered by two choices in the simulator. The first choice is the basic model by which the operator determines the dispenser for each flare in the flare dispenser vector. This determination should

be done before the flight simulation is run. The second model is that, the range between the missile and all dispensers are comparable parameters. Thanks to these parameters, the optimal dispenser can be chosen during the simulation for each time step.

Basic Model: Basic model for dispenser selection is to the determine the dispenser number mounted on the aircraft for each flare at flare dispense time vector which will be generated in Section 5.4.1.1. Here, the most important thing is to determine the flare dispenser vector correctly. Size of this vector must be equal to the size of the flare dispenser time vector. This means that, for all flares, user must define a dispenser correctly.

In this work, to generate the flare dispenser vector, for the selected dispenser, indices of the dispenser ID must be used in this vector. These indices are shown on Table 5.2.

Table 5.2: Flare Dispenser Vector Indices

Dispenser ID	Flare Dispenser Vector Indices
S0	0
S1	1
S2	2
S3	3

For instance, flare dispenser time vector has 8 time values. Thus, flare dispenser vector which is determined by the basic model must have 8 dispenser ID indices.

$$\begin{gathered} Flare\ Dispense\ Time\ Vector = [1.1\ 1.3\ 2.3\ 2.5\ 3.5\ 3.7\ 1.1\ 1.3] \\ Flare\ Dispenser\ Vector : [0\ 0\ 1\ 1\ 2\ 2\ 0\ 0] \end{gathered} \tag{5.6}$$

Distance between Missile and Dispensers Model: Basic model for selection of disperser has some disadvantages. Before simulation, user must define dispensers for each flare. However, aircraft may maneuver and user cannot estimate which dispenser will be closer or the best choice when initiating dispensing of flare because of position and rotation of the aircraft. Thus, a new model is proposed by us to determine the dispenser. Proposed model compares the distance between the missile and dispensers position. The dispenser which is the closest to the aircraft, is selected for the flare when flare dispensing time selection. If this model is selected, determination of dispenser with this calculation is done only once for each flare.

The main problem for this model is that is the necessity for calculation of the position of each dispenser in earth-fixed coordinates. For this purpose, position of each dispenser values at Table 5.1 with respect to body-coordinates is used. Then, this position is transformed to earth-fixed coordinate system using the Euler angles of the aircraft and dispenser rotation angle. Transformation matrix is created with the total rotation angle of the dispenser. Next, earth-fixed position of the aircraft is added on this transformed position. Finally, missile 3D earth-fixed position information is taken by ES system. Distance between the missile and the dispensers are calculated with *norm* function. Dispenser which is the closest to the missile is determined for flare dispensing. The model is explained in detail below by equation 5.7, where, T_{EB_D} is the transformation matrix from body-coordinates to earth-fixed coordinates,

P_{BD} is body-coordinate 3D position of dispensers in meters, P_{ED} is dispenser earth-fixed 3D position in meters, P_{EM} is missile earth-fixed 3D position in meters, ψ_{ED} is total azimuth angle of dispenser in degrees, ψ_{BD} is body rotation azimuth angle of dispenser in degrees, θ_{ED} is total elevation angle of dispenser in degrees, θ_{BD} is body rotation elevation angle of dispenser in degrees, ψ_{ED} is roll angle of dispenser in degrees and i is dispenser ID from 0 to 3.

$$\begin{gathered}
\psi_{ED_i} = \psi_{BD_i} + \psi_A \\
\theta_{ED_i} = \theta_{BD_i} + \theta_A \\
\phi_{ED_i} = \phi_A
\end{gathered}$$

$$T_{\psi_{ED_i}} = \begin{bmatrix} cos(\psi_{ED_i}) & -sin(\psi_{ED_i}) & 0 \\ sin(\psi_{ED_i}) & cos(\psi_{ED_i}) & 0 \\ 0 & 0 & 1 \end{bmatrix}$$

$$T_{\theta_{ED_i}} = \begin{bmatrix} cos(\theta_{ED_i}) & 0 & sin(\theta_{ED_i}) \\ 0 & 1 & 0 \\ -sin(\theta_{ED_i}) & 0 & cos(\theta_{ED_i}) \end{bmatrix}$$

$$T_{\phi_{ED_i}} = \begin{bmatrix} 1 & 0 & 0 \\ 0 & cos(\phi_{ED_i}) & -sin(\phi_{ED_i}) \\ 0 & sin(\phi_{ED_i}) & cos(\phi_{ED_i}) \end{bmatrix} \tag{5.7}$$

$$\begin{gathered}
T_{EB_{ED_i}} = T_{\psi_{ED_i}}.T_{\theta_{ED_i}}.T_{\phi_{ED_i}} \\
P_{ED_i} = T_{EB_{ED_i}}.P_{BD_i} + P_{EA}
\end{gathered}$$

$$\begin{gathered}
Distance(1) = norm(P_{ED_0} - P_{EM}) \\
Distance(2) = norm(P_{ED_1} - P_{EM}) \\
Distance(3) = norm(P_{ED_2} - P_{EM}) \\
Distance(4) = norm(P_{ED_3} - P_{EM})
\end{gathered}$$

$$Choosen\ Dispenser = minimum(Distance)$$

5.4.1.3 Selection of Dispensed Flare Type

To deceive the missile with an appropriate ECM technique, more than one flare types are used in this study. Modeled flare types are MTV and spectral flares. Thus, selection of dispensed flare types is the crucial parameter for performance of ECM techniques. For this purpose, three types of flare dispensing selection mode is generated. These are only MTV flare dispensing, only spectral flare dispensing and dispensing both of them in the flare dispense program as shown below.

- flare Type Selection =1 $\Longrightarrow$ Only MTV flare
- flare Type Selection =2 $\Longrightarrow$ Only spectral flare
- flare Type Selection =3 $\Longrightarrow$ MTV and spectral flares

For instance, assume that 8 flare dispensing programs are created. Flare dispensing time is shown below. If flare type selection mode is identical to 1, only MTV flare is dispensed. $flare\,Type$ vector which shows dispensed flares types, is filled only with *"M"* which indicates an MTV flare. However, if flare type election is set to 2, only spectral flare is dispensed. At the same time, $flare\,Type$ vector is filled only with *"S"* which indicates a spectral flare. The last mode is that when flare type selection is identical to 3, both MTV and spectral flares are simultaneously dispensed as shown in $flare\,Type$ vector.

$$Flare\ Dispense\ Time\ Vector = [1.1\ 1.3\ 2.3\ 2.5\ 3.5\ 3.7\ 1.1\ 1.3]$$

$$\begin{aligned} if\ \ Flare\,Type\,Selection == 1 &\Rightarrow flare\,Type : [M\ M\ M\ M\ M\ M\ M\ M] \\ if\ \ Flare\,Type\,Selection == 2 &\Rightarrow flare\,Type : [S\ S\ S\ S\ S\ S\ S\ S] \\ if\ \ Flare\,Type\,Selection == 3 &\Rightarrow flare\,Type : [S\ M\ S\ M\ S\ M\ S\ M] \end{aligned} \tag{5.8}$$

Briefly, CMDS determines flare dispensing programs. At the same time, flare dispensing time, dispensed dispenser and dispensing flare types are defined by the CMDS model. Flare dispensing velocity and flare initial position information are dependent on CMDS dispenser as well.

5.4.2 Flare Models

MTV flare has some disadvantages as declared Section 5.2.2.1. However it is cost-effective and expendable when compared to advanced flare types. It is in demand for Turkish Airforce Army, as well. MTV flare can be effective against advanced missile seekers, as long as optimum flare dispensing program is applied. To generate high-fidelity model, one flare type is not adequate. Spectral flare is modeled to rule out this deficiency.

In the light of this explanation, MTV and spectral flare models have been generated as part of this study. These models consist of 3D IR signature model and motion model. MTV and spectral flare have similar motion models and 3D models. However, their IR signature models are different, because of the fact that MTV flare radiates more than spectral flares. In the following sections, kinematic motion model and 3D IR signature model of flares are explained in detail, respectively.

5.4.2.1 Kinematic Motion Model of Flares

As mentioned in Section 5.2.2.1, MTV flare has free-fall trajectory. However, in this study, MTV and spectral flare models contain only kinematic motion with gravitation and drag force effects instead of a free-fall trajectory to be a more effective ECM technique. Gravitational and drag force affects on the translational accelerometers, velocity and position components of flares which have not any propellant. Due to these effects, flares slow down quickly and separate from an aircraft rapidly.

Flare dispensing time is determined by CMDS which is explained in detail in Section 5.4.1.1. While simulation is running, flare dispense time vector is controlled for each simulation step

in order to check whether or not that is the time to dispense a flare. Flare motion and 3D IR signature model are generated in due time.

Before dispensing flare, flares are contained in cartridges at the dispenser. Flare position, rotation and velocity components are identical with dispenser position, dispenser rotation which are shown at the Table 5.1, and aircraft velocity, respectively. At the same time, there is no gravitational and drag force effect over flare before dispense.

To dispense a flare, cartridges fires squib to eject the flare from the dispenser. As soon as the flare is dispensed, flare dispensing velocity components are calculated with dispenser rotation which is shown at Table 5.1, constant velocity of dispensing flare, aircraft velocity and aircraft rotation. Flare initial earth-fixed velocity is calculated as shown in equation 5.9, where, V_{DF} is the constant velocity of dispensing flare in m/sec, V_{IF_X} is initial earth-fixed velocity of flare along X- axis in m/sec, V_{IF_Y} is initial earth-fixed velocity of flare along Y- axis in m/sec, V_{IF_Z} is initial earth-fixed velocity of flare along Z- axis in m/sec, V_{EA_X} is earth-fixed velocity of aircraft along X-axis in m/sec, V_{EA_Y} is earth-fixed velocity of aircraft along Y-axis in m/sec, V_{EA_Z} is earth-fixed velocity of aircraft along Z-axis in m/sec, ψ_F is total azimuth rotation of flare in degrees, θ_F is total elevation rotation of flare in degrees, ψ_{BD} is body rotation azimuth angle of dispenser in degrees and θ_{BD} is body rotation elevation angle of dispenser in degrees.

$$V_{DF} = 30 \ \tfrac{m}{sec}$$

$$\begin{aligned} V_{IF_X} &= V_{DF}.cos(\psi_F).cos(\theta_F) + V_{EA_X} \\ V_{IF_Y} &= V_{DF}.cos(\psi_F).sin(\theta_F) + V_{EA_Y} \\ V_{IF_Z} &= V_{DF} * sin(\theta_F) + V_{EA_Z} \end{aligned} \tag{5.9}$$

$$\begin{aligned} \theta_F &= \theta_A + \theta_{BD} \\ \psi_F &= \psi_A + \psi_{BD} \end{aligned}$$

Initial dispensed flare position calculation has similarities to calculation of initial flare velocity. Initial flare position is identical to dispenser earth-fixed position. In other words, transformation from body-coordinates to earth-fixed coordinates of dispenser position is equal to finding the initial position of the flare which is calculated by equation 5.7.

After flare initial velocity and position are calculated, next step is calculation of total force on the flare when flare is separated from the aircraft. For this purpose drag force over dispensed flare and gravitational force are calculated. The gravitational force is only effective along Z_E axis as shown in equation 5.10, where, F_G is the gravitational force in Newtons, g is the gravity of earth in $^m/_{sec^2}$ and m is the mass of the flare in kg. However, gravity of earth depends on altitude of the flare. The calculation method of gravity of earth with respect to flare altitude is explained in Section 4.2.3.4.

$$F_G = \begin{bmatrix} 0 \\ 0 \\ mg \end{bmatrix} \tag{5.10}$$

Drag force depends on the physical shape of the flare, air density, speed of the flare and the reference area parameters. Although flare has a 3D geometry in this study, there is an assump-

tion that flare is 2D geometry and named as reference area for the calculation of drag force to simplify calculations. The common equation for drag force calculation is shown at equation 5.11, where, D is the drag force in Newtons, ρ is the air density in $^{kg}/_{m^3}$ which is detailed on Section 4.2.3.4, V_{EF} earth-coordinate speed of the flare in $^{m}/_{sec}$, $\bar{V}_{EF}$ is earth-coordinate 3D velocity of flare in $^{m}/_{sec}$, s_F reference area in m^2 and C_D is drag coefficient, [45].

$$D = \frac{C_D.s_F.\bar{V}_{EF}.V_{EF}.\rho}{2} \tag{5.11}$$

Drag coefficient is a non-dimensional parameter and the shape effect on the drag coefficient is illustrated in Figure 5.10. In this study, the flare shape is 3D prism. Thus C_D is chosen as 1.14, [46].

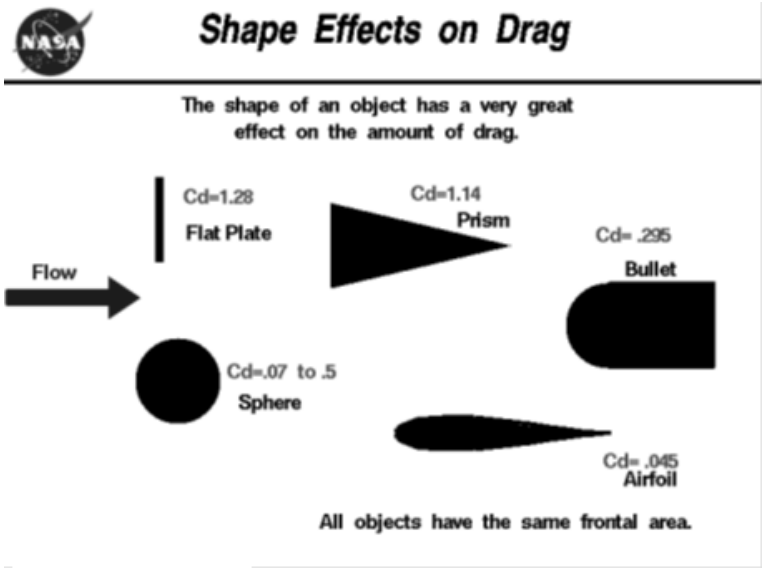

Figure 5.10: Shape Effects on Drag

Total force on the flare is the difference between gravitational force and drag force as shown in equation 5.12, where, F_{TF} shows that total force in Newtons. However the mass of the flare diminishes with burning effect; in this study flare mass is assumed to be constant. Thus, accelerations of the flare can be calculated as shown in equation 5.13, where, a_F is 3D accelerations of the flare in $^{m}/_{sec^2}$ and m_F is the mass of flare in kg.

$$F_{TF} = F_G - D \tag{5.12}$$

$$a_F = \frac{F_{TF}}{m_F} \tag{5.13}$$

The final step for kinematic motion model of the flare is updating velocity and position information of flare which are shown at equation 5.14, where, P_{EF} is 3D earth-fixed position of

flare, P_{IF} is 3D earth-fixed initial dispensed position of flare, dt is step time in sec and i is simulation step.

$$\begin{aligned} V_{EF}(i+1) &= a_F(i+1)\mathrm{d}t + V_{IF} \\ P_{EF}(i+1) &= V_{EF}(i+1)\mathrm{d}t + P_{IF} \end{aligned} \tag{5.14}$$

Initial earth-fixed velocity and initial earth-fixed position components of the flare are calculated only once when the flare has almost been dispensed. After dispensing of the flare, position and velocity update equations are modified as shown in equation 5.15.

$$\begin{aligned} V_{EF}(i+1) &= a_F(i+1)\mathrm{d}t + V_{EF}(i) \\ P_{EF}(i+1) &= V_{EF}(i+1)\mathrm{d}t + P_{EF}(i) \end{aligned} \tag{5.15}$$

There is an example about how the spectral flare is dispensed from an aircraft $S0$ dispenser as shown in Figure 5.11. Aircraft makes level flight; there is no maneuver during simulation. Flare is dispensed at 1.07 sec, thus spectral flare motion is the same with dispenser $S0$ at aircraft until dispense time. When X_E is equal to 715.4 meters, flare is dispensed and separated from the aircraft. Then, because of the drag force, spectral flare slows down and motion is only along the Z axis.

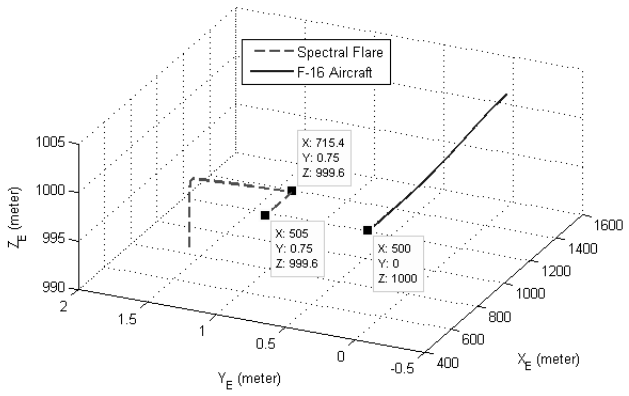

Figure 5.11: Flare Trajectory

5.4.2.2 3D IR Signature Model of Flares

Spectral and MTV flare 3D IR signature are modeled in this study. Although MTV flare is a point source in reality, in this study 3D IR signature of MTV flare is modeled as cone whose height and bottom circle radius can be adjustable by user in order to provide high-fidelity modeling and seen from the viewpoint of IIR missile seeker. Spectral flare 3D model is similarly modeled as MTV flare 3D model even their IR radiation characteristics are not similar.

As described in the 3D IR signature model of the F-16 aircraft, the major parameters used in radiance calculation of IR signature are surface temperature and material physical character-

istics. Moreover, MTV and spectral flare IR signatures are functions of rise and burn time of flares as explained in detail at Sections 5.2.1.2 and 5.2.1.3.

3D Models of Flare: 3D model of spectral and MTV flares are modeled as a cone. Unlike the model of an aircraft, 3D model of flares has only one sub-target which has two major parameters to adjust for the desired geometrical model design. These parameters are height and bottom circle radius. In this study, bottom radius of the cone is chosen as 0.8 meters and the height of the cone is 3 meters as shown in Figure 5.12.

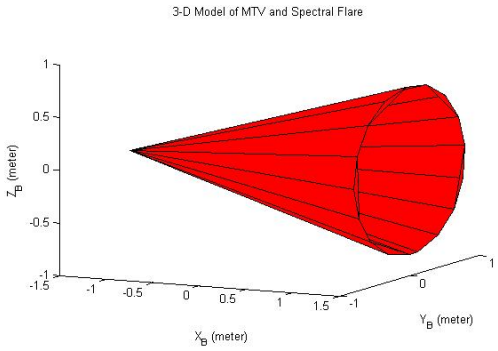

Figure 5.12: 3D Models of Flare

3D cone is modeled by VRML Toolbox with 18 triangle polygons as well. Three vertices of each polygon and 18 polygons information are converted from VRML Toolbox to MATLAB as described in detail at Section 4.3.2.

IR Signature of MTV Flare: Spectral radiance of MTV flare is calculated with Plank Law which is shown at equation 1.11, where, $\zeta_{atm}(\lambda)$ is atmospheric transmission between the missile and MTV flare, $\epsilon(\lambda)$ is the emissivity coefficient of the flare which is 0.9 because of gray-body assumption of MTV flare and T is the surface temperature which is $1800\ K$.

As a reminder, MTV flare is assumed to have an isotropic surface, in other words, a Lambertian surface and of gray body which means that its emissivity coefficient is constant throughout spectral bands. Spectral radiance of MTV flare is integrated to get the total radiance with given IR spectral band intervals. Equation 2.1 is used for this purpose.

Unlike aircraft and background sources, flare IR signature is not permanent. As mentioned before, flare IR signature is a function of time. Thus, temporal response of flare radiation is modeled as dependent on time, which is modeled as having an exponential rise and burn times and their constant values, [9].

Proposed exponential time function model is shown below at equation 5.16, where, t is simulation time in sec, $f(t)$ is the time function, $L(t)$ is the temporal MTV flare radiation in $^{W}/_{cm^2 sr}$, L is the radiation of MTV flare without temporal effect in $^{W}/_{cm^2 sr}$, $t_{dispense}$ is dispensing time of flare in sec which is appended to the flare dispense time vector, $t_{ignition}$ is ignition time of MTV flare in sec which is a little bigger than dispenser time to protect the aircraft from highly explosive effect of the flare. In this study, ignition time of flare is 20 ms

delayed from the dispense time, t_r is the rise time in sec which is the elapsed time to reach a peak radiation value after flare is ignited. Rise time for MTV flare is 200 msec, t_b is the burning time of flare in sec. Burning time for MTV flare is 3.5 sec, τ_b is the burning time constant and which is 6 and τ_r is the rise time constant and its value is 0.1.

$$
\begin{gathered}
t_{ignition} = t_{dispense} + 0.02sec \\
if \;\; t < t_{ignition} \Longrightarrow f(t) = 0 \\
if \;\; t \geq t_{ignition} \; and \; t < t_r + t_{ignition} \Longrightarrow f(t) = 1 - e^{-t/\tau_r} \\
if \;\; t \geq t_r + t_{ignition} \; and \; t < t_r + t_b \Longrightarrow f(t) = e^{-(t - t_r - t_{ignition})/\tau_b} \\
if \;\; t > t_r + t_b \Longrightarrow f(t) = 0 \\
L(t) = L.f(t)
\end{gathered}
\tag{5.16}
$$

In order to enhance the clarity of the model, there is an example which is shown in Figure 5.13. After dispensed from the aircraft at 1.07 sec, flare emitted radiation at 1.09 sec because of 200 msec elapsed time. Then, radiation of flare reaches its maximum value at 1.29 sec. The difference between ignition time and time of reaching maximum point is the rise time. After reaching maximum radiation value which is 3.5 $^{W}/_{cm^2 sr}$, flare begin to decrease until 4.79 sec. This elapsed time is named as burn time of the flare.

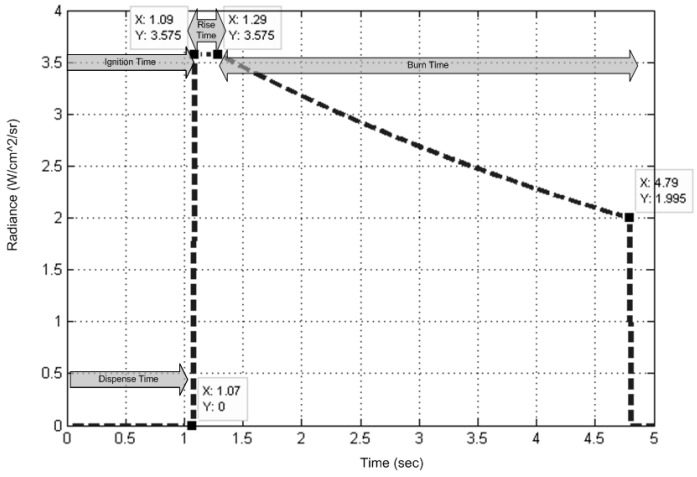

Figure 5.13: MTV Flare Temporal IR Signature

Our approach to color MTV flare with respect to temporal radiance function ($L(t)$) has been explained in detail at IR missile seeker section. However, there is an example that is a demonstration of MTV flare 3D IR signature model from the viewpoint of missile seeker is shown in Figure 5.14.

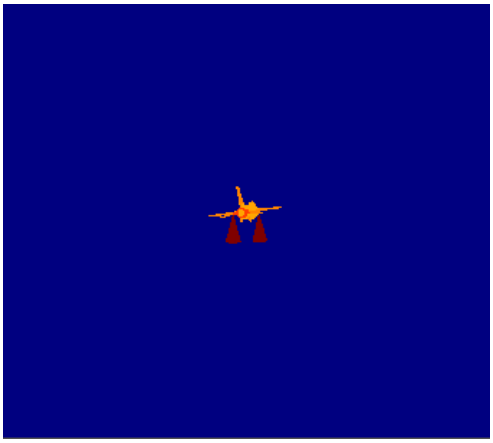

Figure 5.14: Example of Colored MTV Flare

IR Signature of Spectral Flare: Advanced IR missile can discriminate MTV flares with advanced spectral ECCM techniques due to either comparing its radiation with radiation of target or ratio of radiation value of MTV flares at different spectral bands. In this study, dual band detector can easily discriminate MTV flares to compare its emitted radiation values at different spectral bands intervals which are $3-5\ \mu m$ and $8-12\ \mu m$.

Spectral flares have IR signatures matched with the aircraft IR signature because of its chemical components which are pyrophoric materials [9], [43]. Thanks to these specific characteristics, spectral ECCM of advanced IR missiles cannot be triggered easily.

In this study, spectral flares are modeled by adjusting their temperature so that its IR signature matches to that of the aircraft. Temperature of spectral flare is determined with Wien's Displacement Law which tells relationship between wavelength of maximum radiation occurs with given temperature as declared in Section 1.2.1.4. $3-5\ \mu m$ spectral band intervals is one of the channel of modeled IIR missile in this study. Thus, spectral flare IR radiation should peak at $4\ \mu m$. After determination of spectral flare's peak radiance wavelength, temperature of spectral flare is calculated with Wien's Displacement Law as shown in equation 5.17.

$$T = \frac{2897.756}{\lambda_{max}} = \frac{2897.756}{4} = 724.5\ K \tag{5.17}$$

With given temperature, spectral radiance of spectral flare is calculated with equation 5.18, where, G_F is the gain of spectral flare radiation which arranges MTV flares radiation level with spectral flare. Without G_F gain, MTV flare radiation is much higher than spectral flare and their radiance level cannot be comparable. G_F is determined with proportion of peak level of MTV flares radiation. In this study, G_F is taken as 0.85.

$$L(\lambda, T) = \frac{1}{\pi} \frac{G_F\ \epsilon(\lambda)\ \zeta_{atm}(\lambda)\ 3.7418\ 10^4}{\lambda^5 (e^{\frac{14388}{\lambda T}} - 1)} \qquad \frac{W}{sr\ \mu m\ cm^2} \tag{5.18}$$

As similar to MTV flare, spectral flare has gray-body and isotropic surface. Spectral flare

emissivity coefficient is assumed as 0.9. After that, radiation of spectral flare at required wavelength intervals are calculated by taking the integral of spectral radiance as shown in equation 2.1. Time dependency of spectral flare is similar with MTV flare which is explained in detail at Section 5.4.2.2, equation 5.16 and demonstrated at Figure 5.13.

Figure 5.15 demonstrates that, MTV flare reaches its peak level at $1.6\ \mu m$. However, spectral flare maximum point is $4\ \mu m$ because of arrangement with its surface temperature.

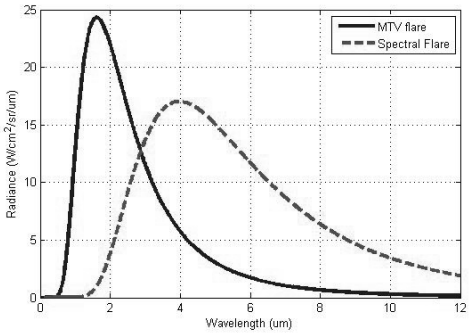

Figure 5.15: MTV and Spectral Flare IR Radiation Levels

Transformation of 3D Flares from Body-Coordinates to Earth-Fixed Coordinates: After creating 3D IR signature model, this model has to be transformed from body-coordinates to earth-fixed coordinates thanks to spectral and MTV flares motion models. 3D geometrical model of flares are constructed in body-coordinates initially. So as to generate IR scene from the viewpoint of the missile seeker, this model must be transformed earth-fixed coordinates. To this end, Euler angles must be calculated with respect to the velocity components of flares. After Euler angles calculation, these angles are used in the transformation. At the end, flares' earth-fixed position which are generated by the motion model are summed with transformed position of flare.

So as to calculate Euler angles with respect to 3D velocity components of flares, *cart2sph* MATLAB function is used. Due to this function, azimuth (ψ_F) and elevation (θ_F) angles of flares are generated with given 3D earth-fixed velocity component. Then, transformation matrix T_{EB_F} is generated with these angles; however there is an assumption that, flare is not rotating along roll axis. This transformation is realized for 18 polygons which constitute 3D cone of flares' model. After transformation of 3D model, earth-fixed positions of flares are added over position of transformed vertices as shown in equation 5.19, where, $k = 1$ is sub-target number (There is only one sub-target which is cone.), $j = 1 : 18$ is polygons number, $i = 1 : 3$ indice number of polygon's vertices, ψ_F is yaw angle of flare in degrees, θ_F is pitch angle of flare in degrees, $\phi_F = 0$ is roll angle of flare in degrees, T_{EB_F} is transformation matrix from body-coordinates to earth-fixed coordinates, X_{BF_v} is vertices positions from center of body-coordinate system along X-axis in meters, Y_{BF_v} is vertices positions from center of body-coordinate system along Y-axis in meters, Z_{BF_v} is vertices positions from center of body-coordinate system along Z-axis in meters, P_{EF} is 3D earth-fixed position of flare in meters, X_{EF_v} is earth-fixed position of vertices along X-axis in meters, Y_{EF_v} is earth-fixed position of vertices along Y-axis in meters and Z_{EF_v} is earth-fixed position of vertices along

Z-axis in meters.

$$T_{\psi_F} = \begin{bmatrix} cos(\psi_F) & -sin(\psi_F) & 0 \\ sin(\psi_F) & cos(\psi_F) & 0 \\ 0 & 0 & 1 \end{bmatrix}$$

$$T_{\theta_F} = \begin{bmatrix} cos(\theta_F) & 0 & sin(\theta_F) \\ 0 & 1 & 0 \\ -sin(\theta_F) & 0 & cos(\theta_F) \end{bmatrix}$$

$$T_{\phi_F} = \begin{bmatrix} 1 & 0 & 0 \\ 0 & cos(\phi_F) & -sin(\phi_F) \\ 0 & sin(\phi_F) & cos(\phi_F) \end{bmatrix} \tag{5.19}$$

$$T_{EB_F} = T_{\psi_F}.T_{\theta_F}.T_{\phi_F}$$

$$\begin{bmatrix} X_{EF_v}(i,j,k) \\ Y_{EF_v}(i,j,k) \\ Z_{EF_v}(i,j,k) \end{bmatrix} = T_{EB_F}. \begin{bmatrix} X_{BF_v}(i,j,k) \\ Y_{BF_v}(i,j,k) \\ Z_{BF_v}(i,j,k) \end{bmatrix} + P_{EF}$$

Transformed vertices position matrices (X_{EF_v}, Y_{EF_v} and Z_{EF_v}) are given *fill3* function of MATLAB to generate IR scene from the viewpoint of missile seeker.

CHAPTER 6

SIMULATION RESULTS

6.1 Introduction

In this chapter, performances of the proposed IIR seeker guided missile model and advanced ECCM techniques are to be evaluated with batch-run simulations. This batch-runs are set to cover all possible scenarios arranged with 8 different major cases. In addition to these, each case has its own differences as minor cases.

6.2 Major Cases

In order to obtain the performance of the missile model, we should deal with 8 major cases. These cases are selected for the purpose of presenting difficulties to the missile seeker. These major cases and number of their minor cases are all listed at the Table 6.1. Major cases associated with the flare dispense program are determined with minor cases with respect to target maneuvers. Thus, there is no increase over the total number of simulations, even though number of minor case flare dispense programs is identical to two. As a result, a total of 1458 different simulations have been performed using the modeled simulator.

Table 6.1: Major Cases and Number of Minor Cases

Major Cases	Number of Minor Cases
Target Maneuver	3
Target - Missile Orientation and Position	3
Weather Condition	2
Kinematic ECCM	3
Area ECCM	3
Sector Strengthening ECCM	3
Flare Dispense Time Selection	3
Flare Dispensing Program	2

Simulation results are compared for all major cases with special regard to their minor cases. The main comparable performance parameter outputs of the simulator are miss distance and missile flight time in seconds. While discussing simulation results later in this chapter, per-

formance of the system will be analyzed based on these output parameters.

Except these major and minor cases, there are common parameters such as simulation time, simulation step time, missile FOV angle etc. Some of these parameters have already been mentioned at previous chapters. Rest of these parameters are listed at the Table 6.2. Each scenario lasts 8 seconds with 10 msec time intervals. However, frame rate is 30 msec, which means that scene image is captured in one-third of the step time. Missile centroid detection mode is set to binary mode. This mode measures 2D center position of the source. However, intensity centroid measures source position close to the hottest part. In order to evaluate the performance of the missile seeker with respect to major cases, binary centroid mode is selected. Terminated frame number means that simulation is terminated when there is no source on scene for 3 frames. The activation of fuze is set to 7 meters. The miss distance (range) between missile and target is calculated with respect to their center of gravity. However F-16 aircraft platform is modeled in 3D using real physical dimensions. When fuze is triggered, there would be less distance than 7 meters between the missile and the target because of 3D model of F-16 aircraft.

Table 6.2: Common Parameters for All Scenarios

Common Parameter	Value
Step Time	10 $(msec)$
Simulation Time	8 (sec)
Frame Rate	30 (Hz)
Ground Altitude	800 $(meters)$
Target X_{CG}	0.35 $(meters)$
Missile Gimbal Angular Limits	$\pm 60^{\circ}$
Missile Gimbal Body Position	[0.3 0 0] $(meters)$
Detector Resolutions	256 X 256
Missile FOV	6°
Missile Centroid Detection	*Binary*
Terminate Frame Number	3
Activation of Fuze	7 $(meters)$

6.2.1 Minor Cases of Target Maneuver

F-16 aircraft has been modeled as a 6-DOF non-linear dynamical system. There are 3 modes for the maneuvers of this model. These maneuvers are *S Maneuver* (horizontal), *Power on Stall* (vertical) and *Both* of them. The input parameters for these maneuvers are given at the Table 6.3. For detailed information of maneuver parameters, Chapter 5 would be helpful.

6.2.2 Minor Cases of Target - Missile Orientation and Position

In a missile and target engagement, initial positions and rotations of them are the most important parameters. First of all, target position must be in the range of the missile. At the same time, there are some constraints on the missile such as missile initial elevation angle,

Table 6.3: Three Cases of Target Maneuvers

Parameters	Both	S Maneuver	Power on Stall
Maneuver Timing Vector	[1 3 8] (sec)	[1 3 8] (sec)	[1 3 8] (sec)
Throttle Vector $(percentage)$	[0.7 0.7 0.7]	[0.8 0.8 0.8]	[0.75 0.75 0.75]
Elevator (deg)	[-5 5 -5]	[0 0 0]	[-5 5 -5]
Aileron (deg)	[0 0 0]	[0 0 0]	[0 0 0]
Rudder (deg)	[-5 5 -5]	[-5 5 -5]	[0 0 0]

initial launching velocity, maximum range and altitude etc. In this study, as constraints on the missile, maximum initial elevation angle, which is 60^o, range of the IR detector which is maximum at $3000\ m$ have been chosen. In the light of these, 3 different minor cases associated with initial position and rotation for target and missile are created. These cases provide tail-chase engagement, head-on engagement and target motion perpendicular to missile velocity vector. With regard to engagements, initial target and missile 3D position velocity and yaw pitch roll rotation angles are given at the Table 6.4, respectively. For tail chase, target is not rotated. However, for head on and perpendicular engagements, target is rotated at yaw axis to provide engagement.

Table 6.4: Three Minor Cases of the Target - Missile Orientation and Position

Parameters	Tail Chase	Head On	Perpendicular
Initial target position $(meters)$	[600 0 800]	[1200 0 1200]	[800 0 600]
Initial target rotation (deg)	[0 0 0]	[180 0 0]	[90 0 0]
Initial target velocity $(^m/_{sn})$	150	150	150
Initial missile position $(meter)$	[0 0 0]	[0 0 0]	[0 0 0]
Initial missile rotation (deg)	[0 53 0]	[0 45 0]	[0 37 0]
Initial velocity of missile $(^m/_{sn})$	25	25	25

6.2.3 Minor Cases of Weather Condition

As mention at Section 2.2.2, there are three weather conditions modeled. These are *Good*, *Typical* and *Rainy* weather. Background radiation, path radiation and air transmission are calculated at MODTRAN and attached simulator. In this study, good and typical air conditions are selected for minor cases of weather condition. The inputs of MODTRAN for selected air conditions are listed at Table 2.2.

6.2.4 Minor Cases of Kinematic ECCM

Matching and identification blocks perform kinematic ECCM with individual weights. Especially the matching block weight of the kinematic ECCM is considerably dominant among other ECCM techniques which are performed by the matching block. Kinematic ECCM is

the crucial performance parameter for evaluating the performance of the advanced IIR seeker. There are 3 minor cases associated with ECCM which are related to the position gate of the kinematic ECCM and arranged with respect to missile FOV angle. Minor cases values are chosen as, $^{FOV}/_{20}$, $^{FOV}/_{25}$ and $^{FOV}/_{30}$.

6.2.5 Minor Cases of Area ECCM

Area ECCM is also performed by not only the matching block but also the identification block. Area gate has three minor cases of which values are arranged as the percentage of difference between compared sources. These minor case percentages are chosen as 15%, 20% and 25%.

6.2.6 Minor Cases of Sector Strengthening ECCM

Sector strengthening ECCM is only performed at the identification block. However, the target candidate does not provide this ECCM; this source is not labeled as *"T"* even when all other ECCM are triggered for this source. Thus this ECCM technique performance is tested with different minor cases. These cases determine the gate of strengthening ECCM as mentioned in Section 2.2.6.4. The gate values are arranged as 1^o, 1.5^o and 2^o for the batch-run.

6.2.7 Minor Cases of Flare Dispense Time Selection

Flare dispensing time is the most crucial parameter for effective post-launch ECM techniques against a missile. Within the scope of this study, 3 different minor cases of flare dispense time models are developed. These are basic model, aircraft maneuver timing vector model and distance between missile and target model. These models are explained in detail at Section 5.4.1.1.

6.2.8 Minor Cases of Flare Dispensing Program

Flare dispensing programs determines flare dispensing time pattern, the number of dispensing flares, their types and dispenser ID. In this study, there are two flare dispensing programs for each flare dispensed time selection major model as described in Section 6.2.7. So, there are totally 6 different flare dispense programs. Moreover, flare dispensing programs for selected flare dispense time cases are determined by selected target maneuver cases. There is a condition that, if selected maneuver is *Power on Stall*, second flare program is selected. However, *Both* or *S Maneuver* minor cases are selected, flare dispensing program may be set first or second program. All these explanations are summarized at Tables 6.5, 6.6 and 6.7.

6.3 Simulation Results

In order to evaluate performances of the modeled IIR seeker under different circumstances, there is a total of 1458 artifical scenarios simulated. For each circumstance, performance is evaluated with respect to miss distance value between the missile and the target, and flight

Table 6.5: Flare Dispensing Programs for Basic Model Flare Dispense Time

Flare Dispensing Program	1	2
Simultaneous	0	1
Initial dispense time (sec)	0.8	0.04
Initial delay (sec)	0	0
Burst Count	2	2
Burst Interval ($msec$)	20	20
Salvo Count	3	2
Salvo Interval (sec)	0.5	1
Dispenser Selection	[1 0 1 0 1 0]	Distance Model
Flare Type	Only Spectral	Spectral - MTV

Table 6.6: Flare Dispensing Programs for Aircraft Maneuver Timing Vector Model Flare Dispense Time

Flare Dispensing Program	1	2
Simultaneous	0	0
t_{DIBM} ($msec$)	50	-50
Maneuver Timing Vector (sec)	[1 3 8]	[1 3 8]
Initial delay (sec)	0	0
Burst Count	2	2
Burst Interval ($msec$)	20	20
Dispenser Selection	[2 3 2 3 2 3]	Distance Model
Flare Type	Only Spectral	Spectral - MTV

Table 6.7: Flare Dispensing Program for Distance between Missile and Target Model Flare Dispense Time

Flare Dispensing Program	1	2
Simultaneous	0	0
T_{Range} (m)	100	200
Initial delay ($msec$)	10	10
Burst Count	2	2
Burst Interval ($msec$)	20	20
Salvo Count	2	1
Salvo Interval (sec)	0.2	0.1
Dispenser Selection	[0 3 0 3]	Distance Model
Flare Type	Only Spectral	Spectral - MTV

time of the missile. As a consequence, total number of successful scenarios which trigger the missile fuze, and failed scenarios which trigger terminated frame number are counted to determine the average miss distance and the average flight time. In Table 6.8, one can see the total number of scenarios (NOS), the number of successfull scenarios ($Success$), the number

of failed scenarios ($Fail$), average flight time of successful scenarios ($\mu_{FT_{suc}}$), average flight time of failed scenarios ($\mu_{FT_{fail}}$), average miss distance of successful scenarios ($\mu_{MD_{suc}}$) and average miss distance of failed scenarios ($\mu_{MD_{fail}}$).

Table 6.8: All Scenarios' Performance Evaluation

NOS	$Success$	$Fail$	$\mu_{FT_{suc}}$ (sec)	$\mu_{FT_{fail}}$ (sec)	$\mu_{MD_{suc}}$ (m)	$\mu_{MD_{fail}}$ (m)
1458	1408	50	5.10	2.07	5.30	705

Batch-run results as shown in Table 6.8 which indicates that, modeled IIR missile has a perfect probability of kill value. 1408 scenarios among 1458 scenarios are successful. This means that probability of kill value is 96.5%. At the same time, average flight time of succesful scenarios is 5 seconds. However, for failed scenarios, this flight time value is 2.07 seconds. This means that, in order to break the lock of the modeled missile, ECM techniques or evasive maneuvers must be applied as soon as possible after the missile is launched. Similarly, average miss distance value of failed scenarios supports this observation. As one can observe, missile track lock is broken at a range of 705 meters between the missile and the target.

Each major and minor case have been simulated. To remove potential confussion about cases, minor cases are indexed in Table 6.9, where, M_C indicates a major case, m_C is associated with a minor case and I_{m_C} is the indices of minor cases. For each minor case, there are successful and failed scenarios example figures with 3D trajectory plots and miss distance information of missile and aircraft. These figures are titled with a 7 digit number to express selected major and minor case indices. The order of selected minor cases is given in Table 6.9. For example, if the title of the demonstrated simulation is 12213131, the first digit 1 indicates the maneuver case index which means that *"Both"* maneuver is selected. Similarly, second digit is 2 which indicates target - missile orientation and position case. In this example, this case is set to *"Head On"* position. The other digits are set as mentioned. As a result, for given figures, selected minor cases for major cases can be comprehended.

Performance analysis with respect to target maneuver case is illustrated at the Table 6.10. Even when the most effective maneuver is *Both* maneuver (as expected) is utilized, performance of ECCM techniques of modeled missile is significantly effective against all these maneuvers. Missile probability of kill performance parameter is 95.4% against *Both* maneuver. Against other maneuvers this performance value is better. As a consequence, modeled IIR missile is highly effective and lethal against aircraft performing evasive maneuvers.

Figure 6.1 demonstrates three examples for each maneuver minor cases. Among these scenarios, the only difference is maneuver cases and all the other minor cases are same. First example, where target maneuver minor case is *S Maneuver*, is a successfull scenario. Missile hits the target at 5.8 seconds with 6.44 meters miss distance. The other two examples indicate *Power on Stall* and *Both* maneuver cases. However, these cases are failed scenarios. In order to comprehend how missile track gate is broken there is an illustration in Figure 6.2. There are yellow, red and white colored gates and labels are shown at the figure. These colors are crucial for missile decision. White gate and label is used for identification of flare. Similarly, yellow and red label and gates are used for identification of target. However, red gate indicates that missile tracks this labeled object thanks to gimbal target track gate ECCM. Lastly, if there is no label or gate for objects, it is identified as non-defined sources. For each maneuver case,

Table 6.9: Indices of Minor Cases

M_C	m_C	I_{m_C}
Maneuver	Both	1
Maneuver	S Maneuver	2
Maneuver	Power on Stall	3
Position	Tail Chase	1
Position	Head On	2
Position	Perpendicular	3
Weather	Good	1
Weather	Typical	2
Kinematic	Gate $=FOV/25$	1
Kinematic	Gate $= FOV/20$	2
Kinematic	Gate $= FOV/30$	3
Area	Gate = 20%	1
Area	Gate = 25%	2
Area	Gate = 15%	3
Sector Strengthening	Gate = 1^o	1
Sector Strengthening	Gate = 1.5^o	2
Sector Strengthening	Gate = 2^o	3
Flare Dispense Time	Basic	1
Flare Dispense Time	Maneuver Time	2
Flare Dispense Time	Distance	3

Table 6.10: Performance Evaluation of Target Maneuver Case

M_C	I_{m_C}	NOS	Suc	$Fail$	$\mu_{FT_{suc}}$ (sec)	$\mu_{FT_{fail}}$ (sec)	$\mu_{MD_{suc}}$ (m)	$\mu_{MD_{fail}}$ (m)
Maneuver	1	486	464	22	5	1.95	5.51	770.65
Maneuver	2	486	476	10	5.32	4.40	5.60	332
Maneuver	3	486	468	18	4.98	0.92	4.79	832

there are three successive frames in Figure 6.2. First row is for the successful *S Maneuver* case. Second and third rows demonstrate *Power on Stall* and *Both* maneuver cases, respectively. At *S Maneuver* case, missile tracks the target and hits it. However missile track gate is broken for all other cases because of maneuvers and spectral flare dispensing. Missile locks on flare and maneuvering targets get out of FOV of the missile.

Perpendicular orientation and position case is the most difficult case for the modeled missile in the light of simulated scenarios in Table 6.11. Among 486 scenarios, there are 35 failed scenarios for this case. However, there is a remarkable performance against *Head On* case where only three of all scenarios are failed. Thus, probability of kill of the missile for *Head On* missile-target engagement is 99.3%. This result shows that modeled IIR missile is highly effective for approaching targets.

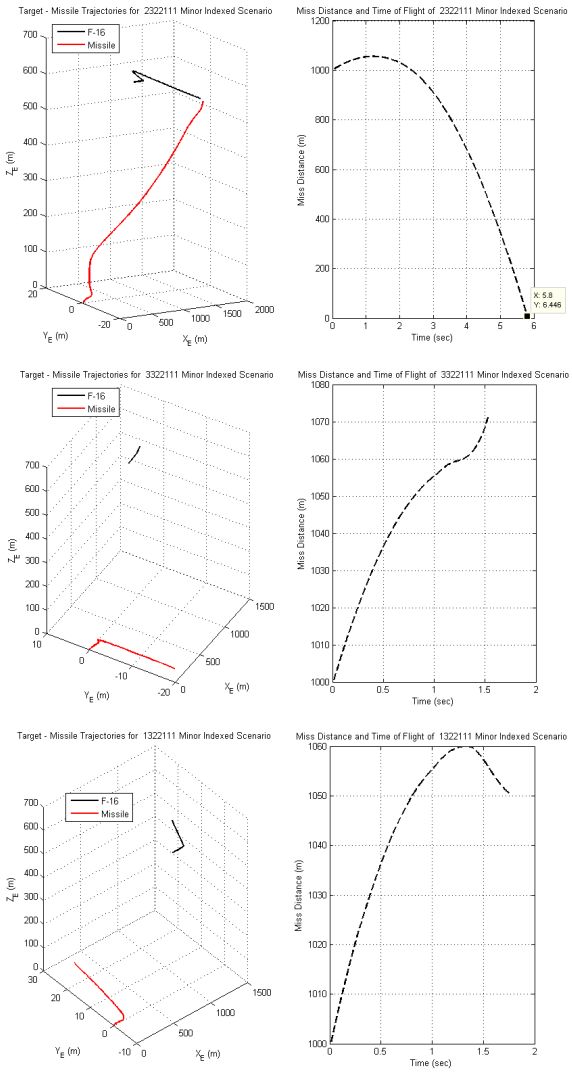

Figure 6.1: Evaluation of Maneuver Cases

Table 6.11: Performance Evaluation of Target - Missile Orientation and Position Case

M_C	I_{mC}	NOS	Suc	$Fail$	$\mu_{FT_{suc}}$ (sec)	$\mu_{FT_{fail}}$ (sec)	$\mu_{MD_{suc}}$ (m)	$\mu_{MD_{fail}}$ (m)
Position	1	486	474	12	5.06	1.16	5.97	774.72
Position	2	486	483	3	4.78	4.74	4.99	24.30
Position	3	486	451	35	5.49	2.15	4.93	739.60

Figure 6.3 shows examples of three different target orientation and position cases. The only failed scenario is the third scenario which is *Perpendicular* movement of target case. It proves that the most difficult problem of the missile seeker is *Perpendicular* target position case. At

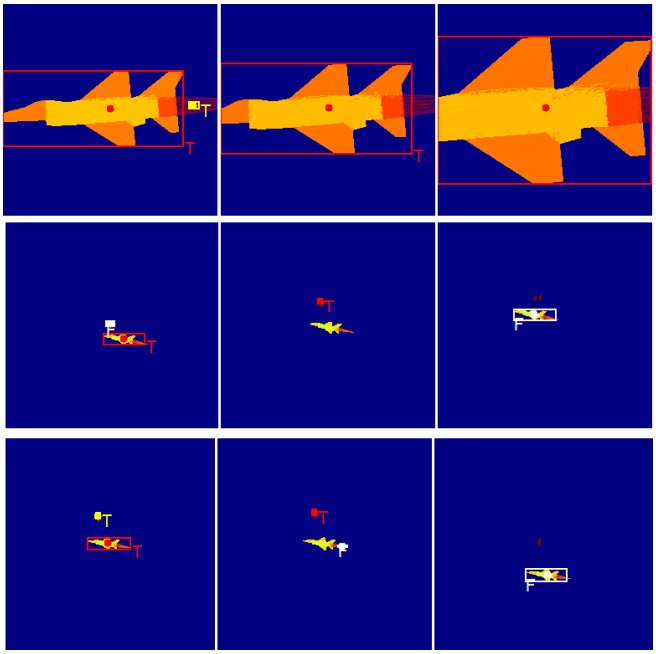

Figure 6.2: Sample Frames for Maneuver Cases

the same time, Figure 6.4 shows that, missile track gate is not broken for first and second examples which are *Tail Chase* and *Head On* cases, respectively as similarly shown at the Figure 6.3. However, at the third example, missile track gate is broken and scenario is failed, which is because of the fact that the angular movement of target is beyond the track gate of missile seeker.

Table 6.12: Performance Evaluation of Weather Condition Case

M_C	I_{m_C}	NOS	Suc	$Fail$	$\mu_{FT_{suc}}$ (sec)	$\mu_{FT_{fail}}$ (sec)	$\mu_{MD_{suc}}$ (m)	$\mu_{MD_{fail}}$ (m)
Weather	1	729	711	18	5.11	2.82	5.28	604.73
Weather	2	729	697	32	5.10	1.65	5.32	761.50

Air transmission effect over missile performance is evaluated at the Table 6.12. With regard to these, *Typical* air condition is more compelling for the missile. This is an expected observation; IR signature of sources on scene are directly affected by the atmospheric transmission. The more rainy or cloudy weather causes the weaker IR signature of sources to be detected by the detector. Under any circumstances, the probability of kill of the missile for the worst case is 95.6%. An example for this condition is shown in Figure 6.5. While, weather condition is *Good*, the missile tracks the target and hit it in 4.77 seconds with 6.45 meter miss-distance. However, for *Typical* weather case, missile track gate is broken at 4.71 seconds when there is 40.19 meters left between the missile and the target.

Kinematic ECCM is the most important technique for matching block because of its weight. For this reason, the performance of missile tracking is directly proportional with this ECCM.

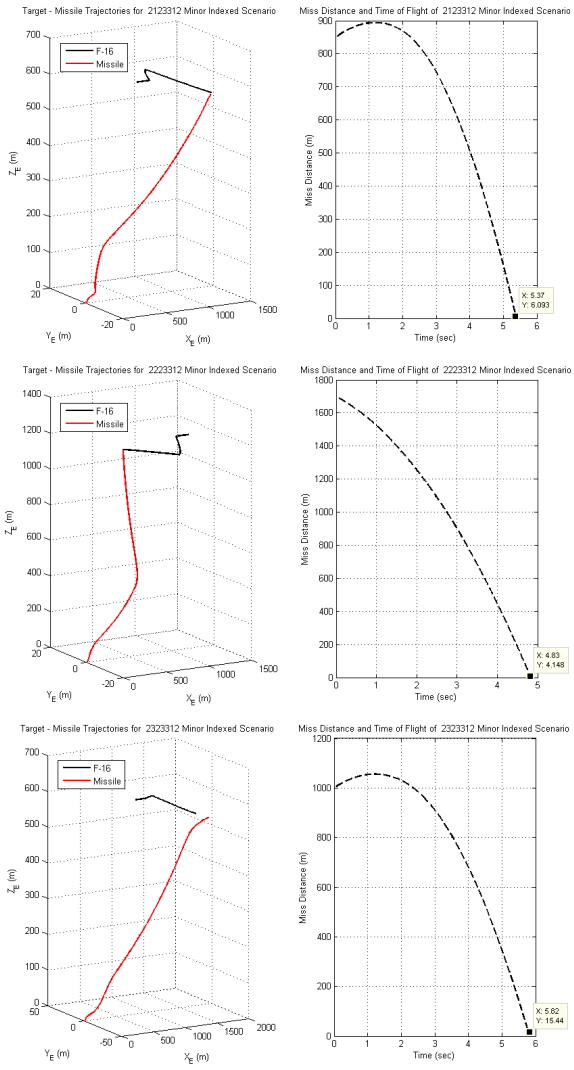

Figure 6.3: Evaluation of Target Orientation and Position Cases

In the light of these, batch-run mode has three different kinematic ECCM position gates. With respect to results as shown in Table 6.13, the performance and effectiveness of ECCM is diminished with not only wider but also narrow gates. This is because wider gate includes more target candidates. Thus, there is more chance for a mismatch to occur. Similarly, narrow gate includes less target candidates inside the gate. Thus target track may be broken while especially the target is maneuvering. The results indicate that, when gate is wider, there are 18 failed scenario. With reference to our results, there are 20 failed scenarios while gate is too narrow. As a consequence of these results, gate value of kinematic ECCM must be arranged carefully and the optimum gate value must be determined. In this study, optimum kinematic position gate is $^{FOV}/_{25}$ as regards to batch-run results.

Figure 6.7 shows the significant examples for three position gates of kinematic ECCM. Only the first example is successful scenario where its position gate is $^{FOV}/_{25}$, which indicates that, wider and narrow gates are not appropriate as declared in Table 6.13. Figure 6.8 shows

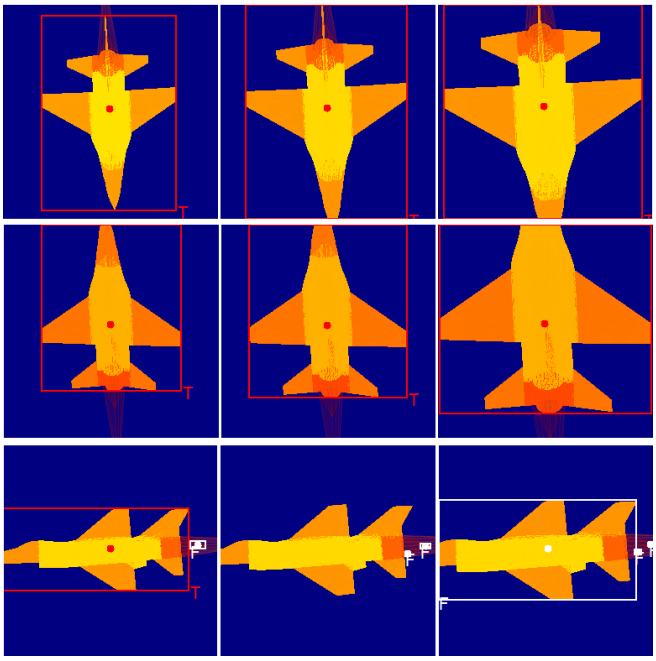

Figure 6.4: Sample Frames for Target Orientation and Position Cases

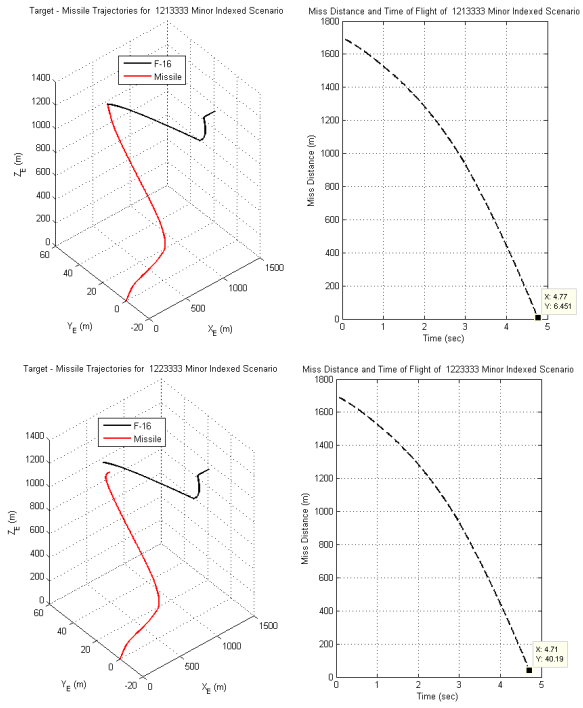

Figure 6.5: Evaluation of Weather Condition Cases

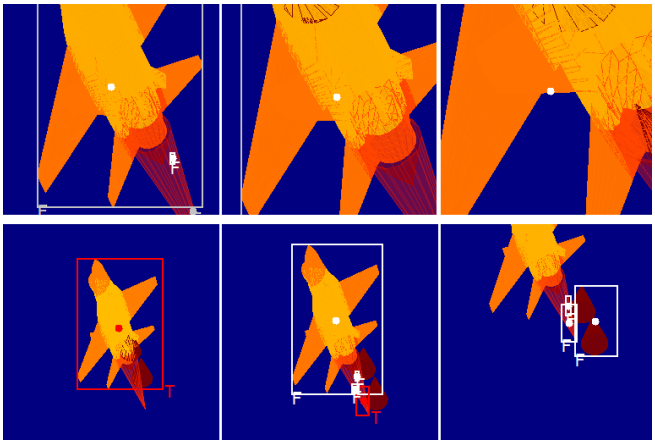

Figure 6.6: Sample Frames for Weather Condition Cases

Table 6.13: Performance Evaluation of Position Gate of Kinematic ECCM Case

M_C	I_{m_C}	NOS	Suc	$Fail$	$\mu_{FT_{suc}}$ (sec)	$\mu_{FT_{fail}}$ (sec)	$\mu_{MD_{suc}}$ (m)	$\mu_{MD_{fail}}$ (m)
Kinematic	1	486	474	12	5.10	2.19	5.31	696.82
Kinematic	2	486	468	18	5.10	1.39	5.32	883
Kinematic	3	486	466	20	5.10	2.61	5.28	549.86

how missile holds the target on track gate for a successful scenario even when the target is maneuvering and applying ECM techniques. However, second and third scenarios, which are associated with $FOV/20$ and $FOV/30$ position gates respectively, are failed, this is because ECM techniques and evasive maneuvers of the target break the missile track gate and the missile lock on flare on scene when these position gates of kinematic ECCM are chosen.

Gate area ECCM performance is shown at the Table 6.14, where there are 3 minor cases. Comparing results with respect to these minor cases, it is seen that the most effective area gate is the biggest area gate. This result is expected, because, if the percentage of the allowed area change between frames is closer to one, the area ECCM may be more effective. The most effective area gate value among 3 minor cases is 25%. There is ony 13 scenarios are failed. However for 20% and 15% area gates, 18 and 19 scenarios are failed, respectively. The probability of kill of the missile for the optimum area gate is 97.3%.

There is an example which contains three scenarios for each area gate case as shown in Figure 6.9. In these scenarios gate values are set to 20%, 25% and 15%, respectively. Only the first scenario is successful. The missile hits the target at 5.35 seconds with a range of 3.47 meters left. However, the second area gate even though it is the optimum area gate, is failed. This is because instantaneous area change is beyond the area gate and matching and identification may not occured for this target. As a result, target track gate of the missile is broken for this scenario. Figure 6.10 shows sample frames of these scenarios indicating that how the missile track gate is broken or not broken against target ECM techniques and evasive maneuvers. At

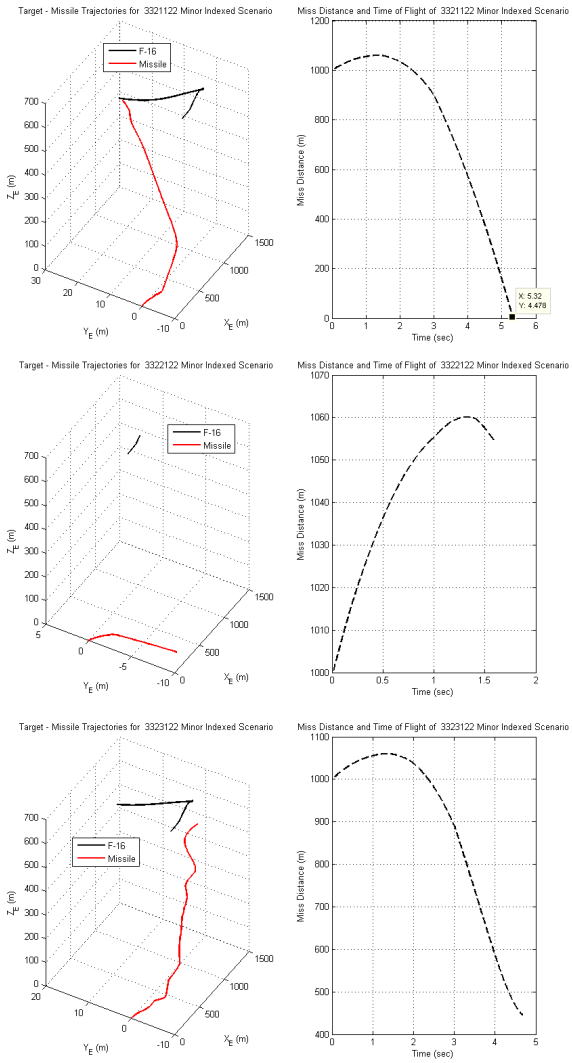

Figure 6.7: Evaluation of Kinematic ECCM Cases

Table 6.14: Performance Evaluation of Area Gate of Area ECCM Case

M_C	I_{m_C}	NOS	Suc	$Fail$	$\mu_{FT_{suc}}$ (sec)	$\mu_{FT_{fail}}$ (sec)	$\mu_{MD_{suc}}$ (m)	$\mu_{MD_{fail}}$ (m)
Area	1	486	468	18	5.10	1.71	5.32	821.49
Area	2	486	473	13	5.10	1.90	5.29	726.35
Area	3	486	467	19	5.10	2.53	5.29	580.31

second and third scenarios, ECM techniques and evasive maneuver are successful so as to break the missile track lock on the target. However, in the first scenario missile track gate is held even if the target applies evasive maneuvers and ECM techniques.

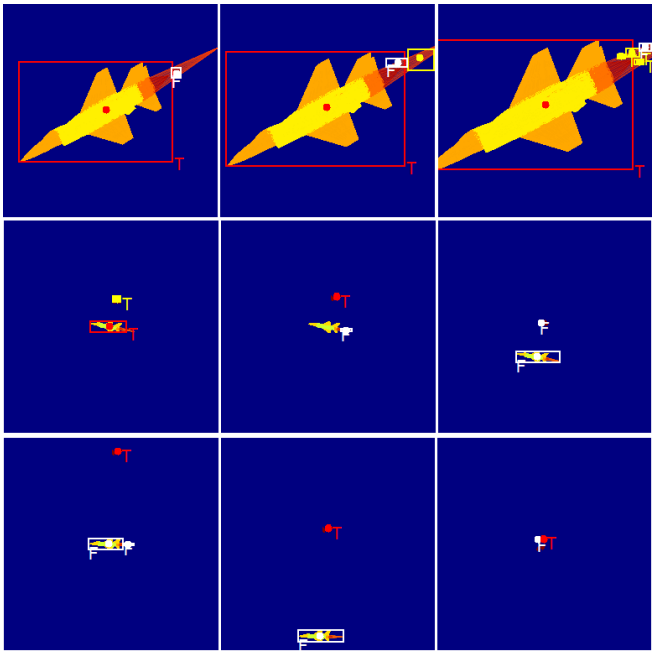

Figure 6.8: Sample Frames for Kinematic ECCM Cases

Sector strengthening ECCM, which labels and identifies sources, affects the missile tracking performance directly. In order to evaulate the performance of this ECCM, there are 3 minor cases chosen as shown in Table 6.15. There are a total of 486 scenarios simulated for each minor case. Missile probability of kill is 95% for the worst case which is 1.5^o for track gate of sector strengthening ECCM.

Table 6.15: Performance Evaluation of Track Gate of Sector Strengthening ECCM Case

M_C	I_{m_C}	NOS	Suc	$Fail$	$\mu_{FT_{suc}}$ (sec)	$\mu_{FT_{fail}}$ (sec)	$\mu_{MD_{suc}}$ (m)	$\mu_{MD_{fail}}$ (m)
Sector Streng.	1	486	462	24	5.10	2.35	5.30	623.17
Sector Streng.	2	486	473	13	5.10	1.83	5.30	790.52
Sector Streng.	3	486	473	13	5.11	1.80	5.30	771

The last, dispense time selection case performance is evaulated with respect to 3 models. These are basic model, maneuver timing model and distance between missile and target model. In the light of results as shown in Table 6.16, basic model performance is the best. At the same time the distance model performance is the worst. This is because of the fact that the flare dispensing trigger of this model is the distance. If flare is dispensed when the missile is too close to the target, this flare would not be effective. For this reason, the distance trigger of this model must be arranged correctly for higher performance. Basic flare dispense time model parameters are arranged before the simulation is run. Due to the optimum choice of the initial parameters of the flare and dispensers, this model is shows the best performance among other models. The last model is the maneuver timing model. This model dispenses flare while target

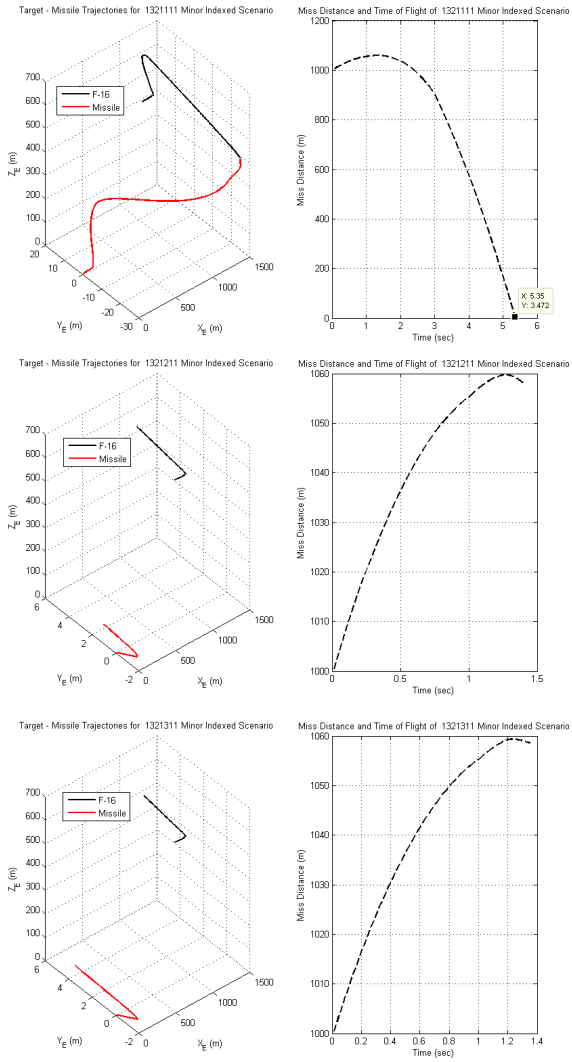

Figure 6.9: Evaluation of Area ECCM Cases

is almost maneuvering. While target is maneuvering, this model expects that the missile track is lock on the flare. However, according to total results shown in Table 6.8, missile response to target maneuver is perfect. Thus this model performance is not as expected.

Table 6.16: Performance Evaluation of Flare Dispense Time Selection Case

M_C	I_{m_C}	NOS	Suc	$Fail$	$\mu_{FT_{suc}}$ (sec)	$\mu_{FT_{fail}}$ (sec)	$\mu_{MD_{suc}}$ (m)	$\mu_{MD_{fail}}$ (m)
Dispense Time	1	486	454	32	5.09	1.65	5.36	798.65
Dispense Time	2	486	473	13	5.10	1.94	5.29	739.62
Dispense Time	3	486	481	5	5.11	5.15	5.27	24.60

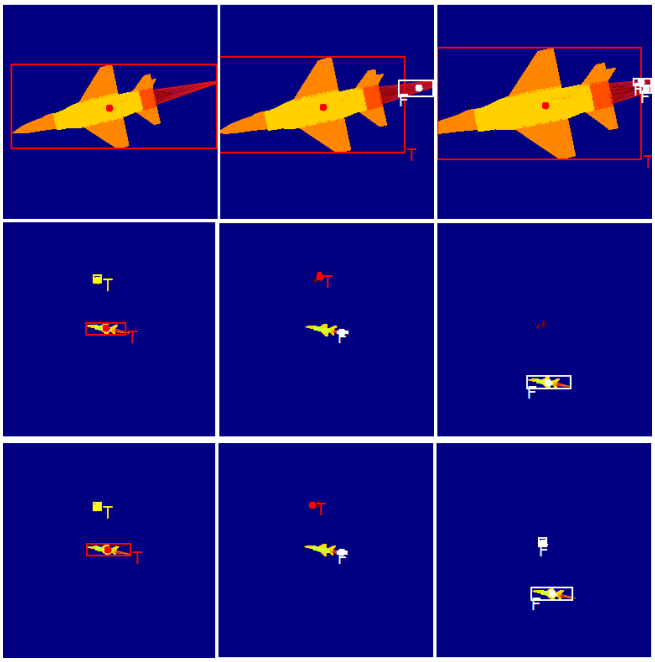

Figure 6.10: Sample Frames for Area ECCM Cases

Figure 6.11 shows three cases of flare dispense time selections. These are basic, maneuver time and range between missile and target models, respectively. Only the maneuver timing model case chosen scenario is successful. This model dispenses 2 spectral flares for each maneuver of the target. The timing of dispensed flares are related with maneuver timing. Target dispenses flares after 50 msec from target maneuvers. Even target dispenses flares, missile does not lock on flares and hits the target as shown in Figure 6.12. However, for other dispense time selection modes, the missile seeker locks on the dispensed flare and scenarios are failed because of ECM tecniques and evasive maneuvers of the target.

After the evaluation of missile seeker performance with respect to major and minor cases, advanced ECCM techniques optimum parameters determination is realized for kinematic, area and sector strengthening ECCM techniques with respect to maneuver, target - missile orientation and position, and dispense time selection modes using batch-run results. In total there are nine tables and each table has 9 different cases because of 3 minor cases for each selection as explained below.

First optimum parameter determination is realized for position gate of kinematic ECCM case. There are three different minor cases for position gate of kinematic ECCM. These are $^{FOV}/_{25}$, $^{FOV}/_{20}$ and $^{FOV}/_{30}$. For each cases, three different maneuver cases, target orientation and position cases and dispense time selection cases are evaluated. As a result, optimum position gate of kinematic ECCM is determined as regards successful and failed scneario numbers.

Thanks to Table 6.17, the optimum position gate of the kinematic ECCM with respect to maneuver case of target is found as $^{FOV}/_{25}$. Similarly, the optimum position gate of the kinematic ECCM with respect to target - missile orientation and position case and flare dispense time case are also $^{FOV}/_{25}$ as shown in Table 6.18 and in Table 6.19, respectively. Consequently, for

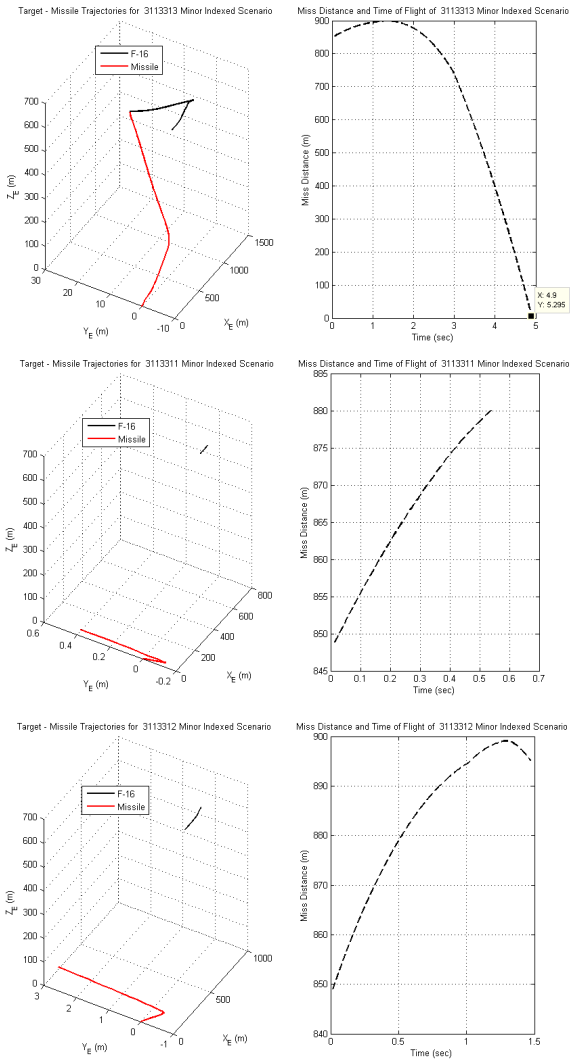

Figure 6.11: Evaluation of Flare Dispense Time Selection Cases

each compared cases, $^{FOV}/_{25}$ position gate of the kinematic ECCM is chosen as the optimum gate value.

Second optimum parameter determination is realized for the gate of sector strengthening ECCM. There are three different cases for this ECCM as well. These are 1.5^o, 1^o and 2^o. For each cases, three different maneuver cases, target orientation and position cases and dispense time selection cases are evaluated. As a result, the optimum position gate of sector strengthening ECCM is determined as regards to successful and failed scenarios.

For the maneuver case, the optimum gate for sector strengthening ECCM is either 1.5^o or 2^o as shown in Table 6.20. However, for target - missile orientation and position, flare dispense time cases, either 1^o or 2^o is optimal as shown in Tables 6.21 and 6.22, respectively. As a result of these observations, the optimum gate value for this ECCM is chosen as 2^o, since, for all compared cases this gate value produces the optimum performance.

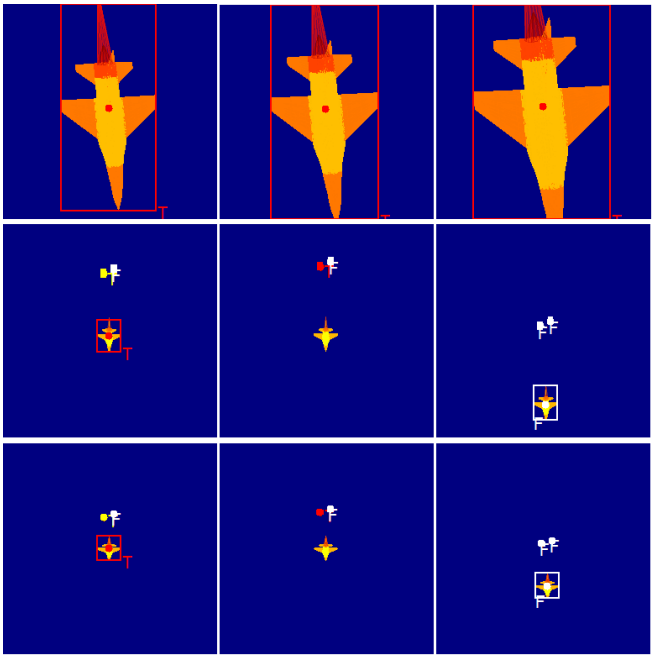

Figure 6.12: Sample Frames for Flare Dispense Time Selection Cases

Table 6.17: Optimum Position Gate of Kinematic ECCM Determination wrt Maneuver Case of Target

Position Gate	Compared Case	Compared Case Value	NOS	$Success$	$Fail$
$^{FOV}/_{25}$	Maneuver	Both	162	155	7
$^{FOV}/_{20}$	Maneuver	Both	162	152	10
$^{FOV}/_{30}$	Maneuver	Both	162	157	5
$^{FOV}/_{25}$	Maneuver	S Maneuver	162	159	3
$^{FOV}/_{20}$	Maneuver	S Maneuver	162	161	1
$^{FOV}/_{30}$	Maneuver	S Maneuver	162	156	6
$^{FOV}/_{25}$	Maneuver	Power on Stall	162	160	2
$^{FOV}/_{20}$	Maneuver	Power on Stall	162	155	7
$^{FOV}/_{30}$	Maneuver	Power on Stall	162	153	9

Final optimum parameter determination is realized for the gate of area ECCM case. There are three different cases for this ECCM as well. These are 20%, 25% and 15%, respectively. For maneuver and flare dispensing time selection cases, the optimum gate of area ECCM value is 25% as shown in Tables 6.23 and 6.25. Yet, for target - missile orientation and position case, with regards to Table 6.24 results and observations, the optimum value is determined as either 20% or 25%. As a result of these observation, the optimum gate value for this ECCM is determined as 25%.

Table 6.18: Optimum Position Gate of Kinematic ECCM Determination wrt Target - Missile Orientation and Position

Position Gate	Compared Case	Compared Case Value	NOS	$Success$	$Fail$
$^{FOV}/_{25}$	Position	Tail Chase	162	161	1
$^{FOV}/_{20}$	Position	Tail Chase	162	160	2
$^{FOV}/_{30}$	Position	Tail Chase	162	153	9
$^{FOV}/_{25}$	Position	Head On	162	161	1
$^{FOV}/_{20}$	Position	Head On	162	162	0
$^{FOV}/_{30}$	Position	Head On	162	160	2
$^{FOV}/_{25}$	Position	Perpendicular	162	152	10
$^{FOV}/_{20}$	Position	Perpendicular	162	146	16
$^{FOV}/_{30}$	Position	Perpendicular	162	153	9

Table 6.19: Optimum Position Gate of Kinematic ECCM Determination wrt Flare Dispense Time Case

Position Gate	Compared Case	Compared Case Value	NOS	$Success$	$Fail$
$^{FOV}/_{25}$	Dispense Time	Basic	162	155	7
$^{FOV}/_{20}$	Dispense Time	Basic	162	149	13
$^{FOV}/_{30}$	Dispense Time	Basic	162	150	12
$^{FOV}/_{25}$	Dispense Time	Maneuver Time	162	159	3
$^{FOV}/_{20}$	Dispense Time	Maneuver Time	162	157	5
$^{FOV}/_{30}$	Dispense Time	Maneuver Time	162	157	5
$^{FOV}/_{25}$	Dispense Time	Distance	162	160	2
$^{FOV}/_{20}$	Dispense Time	Distance	162	162	0
$^{FOV}/_{30}$	Dispense Time	Distance	162	159	3

Table 6.20: Optimum Gate of Sector Strengthening ECCM Determination wrt Maneuver Case of Target

Gate	Compared Case	Compared Case Value	NOS	$Success$	$Fail$
1.5^o	Maneuver	Both	162	152	10
1^o	Maneuver	Both	162	156	6
2^o	Maneuver	Both	162	156	6
1.5^o	Maneuver	S Maneuver	162	156	6
1^o	Maneuver	S Maneuver	162	159	3
2^o	Maneuver	S Maneuver	162	161	1
1.5^o	Maneuver	Power on Stall	162	154	8
1^o	Maneuver	Power on Stall	162	158	4
2^o	Maneuver	Power on Stall	162	156	6

Table 6.21: Optimum Gate of Sector Strengthening ECCM Determination wrt Target - Missile Orientation and Position

Gate	Compared Case	Compared Case Value	NOS	$Success$	$Fail$
1.5^o	Position	Tail Chase	162	156	6
1^o	Position	Tail Chase	162	159	3
2^o	Position	Tail Chase	162	159	3
1.5^o	Position	Head On	162	160	2
1^o	Position	Head On	162	162	0
2^o	Position	Head On	162	161	1
1.5^o	Position	Perpendicular	162	146	16
1^o	Position	Perpendicular	162	152	10
2^o	Position	Perpendicular	162	153	9

Table 6.22: Optimum Gate of Sector Strengthening ECCM Determination wrt Flare Dispense Time Case

Gate	Compared Case	Compared Case Value	NOS	$Success$	$Fail$
1.5^o	Dispense Time	Basic	162	146	16
1^o	Dispense Time	Basic	162	153	9
2^o	Dispense Time	Basic	162	155	7
1.5^o	Dispense Time	Maneuver Time	162	157	5
1^o	Dispense Time	Maneuver Time	162	159	3
2^o	Dispense Time	Maneuver Time	162	157	5
1.5^o	Dispense Time	Distance	162	159	3
1^o	Dispense Time	Distance	162	161	1
2^o	Dispense Time	Distance	162	161	1

Table 6.23: Optimum Gate of Area ECCM Determination wrt Maneuver Case of Target

Gate	Compared Case	Compared Case Value	NOS	$Success$	$Fail$
20%	Maneuver	Both	162	154	8
25%	Maneuver	Both	162	156	6
15%	Maneuver	Both	162	154	8
20%	Maneuver	S Maneuver	162	160	2
25%	Maneuver	S Maneuver	162	158	4
15%	Maneuver	S Maneuver	162	158	4
20%	Maneuver	Power on Stall	162	154	8
25%	Maneuver	Power on Stall	162	159	3
15%	Maneuver	Power on Stall	162	155	7

Table 6.24: Optimum Gate of Area ECCM Determination wrt Target - Missile Orientation and Position

Gate	Compared Case	Compared Case Value	NOS	$Success$	$Fail$
20%	Position	Tail Chase	162	150	12
25%	Position	Tail Chase	162	155	7
15%	Position	Tail Chase	162	149	13
20%	Position	Head On	162	157	5
25%	Position	Head On	162	161 157	5
15%	Position	Head On	162	159	3
20%	Position	Perpendicular	162	161	1
25%	Position	Perpendicular	162	161	1
15%	Position	Perpendicular	162	159	3

Table 6.25: Optimum Gate of Area ECCM Determination wrt Flare Dispense Time Case

Gate	Compared Case	Compared Case Value	NOS	$Success$	$Fail$
20%	Dispense Time	Basic	162	146	16
25%	Dispense Time	Basic	162	153	9
15%	Dispense Time	Basic	162	155	7
20%	Dispense Time	Maneuver Time	162	157	5
25%	Dispense Time	Maneuver Time	162	159	3
15%	Dispense Time	Maneuver Time	162	157	5
20%	Dispense Time	Distance	162	159	3
25%	Dispense Time	Distance	162	161	1
15%	Dispense Time	Distance	162	161	1

CHAPTER 7

CONCLUSION AND FUTURE WORKS

In this study, the aim is to develop a new IR guided missile equipped with an advanced imaging seeker. In this direction, first, the IR seeker model is obtaied. This model consists of a dual band FPA detector, a processor, utilization of advanced ECCM techniques and a gimbal model. Dual band detectors' spectral responses are in the MWIR and LWIR bands and their resolutions are $256X256$ pixels. These detectors are modeled in such a way that they process an IR image formed with received radiation from the scene. Processor model captures the image from the scene and extracts features of objects. These features are sent to the ECCM model to analyse and to be identified. As ECCM techniques, denomination, track gate, sector strengthening, area, kinematic and dual band ratio information of objects are used. These are compared with the history of tracked object and a match is sought. After that, identification block identifies these matched objects as target or flare. Then gimbal tracks the decided target and sends its angular position to the guidance algorithm.

After modeling the IR seeker, guidance algorithm and the kinematic motion models are derived. In this study, the PNG law is used. Closing velocity is taken as constant; $200\ {}^{m}/_{sec.}$ Navigation constant is set to 3.1. The azimuth and elevation LOS rate values are obtained by the gimbal. As a result, horizontal and vertical accelerations are measured to be used by the guidance law. Then, kinematic model moves the missile towards the target. For this purpose, commanded horizontal and vertical accelerations and thrust force are required. In this study, instead of using the thrust force directly, a velocity profile is generated with respect to time. As a consequence of these, 3D accelerations, total velocity and position information are calculated.

In order to evaluate performance of this proposed missile, F-16 target model is developed. This model contains 3D IR signature model with different temperature zones and 6-DOF nonlinear dynamic model. Thanks to the motion model, target model can execute evasive maneuvers. Moreover, target model may apply ECM techniques. These are dispensing spectral and/or MTV flares, which have 3D IR signatures and kinematic motion model as well, to deceive or break the track gate of the missile. Next, atmospheric effects are included in IR scene generation to obtain high fidelity modeling. Finally, simulations are executed to evaluate the performance of proposed IIR missile seeker and advanced ECCM techniques.

In Chapter 6, the performance of the proposed missile has been evaluated. In the light of these results, *Both* type maneuver case is the most effective evasive maneuver technique to deceive the missile seeker. However, *S Maneuver* case is not as effective as other maneuvers. Similarly, proposed missile is highly effective against approaching (*Head On*) targets. There are only 3 scenarios among 486 that failed with approaching and maneuvering targets. Weather

condition is also a crucial performance parameter. Even, for not only under *Typical* but also under *Good* conditions, missile is highly lethal against targets. Although, at *Good* weather, missile seeker performance is significantly better. Missile seeker is highly effective against target maneuvers, position and orientation of the target, and weather conditions (the probability of kill value of the missile is beyond 90% for these cases). Last, flare dispensing time selection mode is tested as well. There are 3 models which are basic, maneuver timing and distance between target and missile models. Among these model, basic model is the most effective case against the missile seeker.

At the same time, modeled advanced ECCM techniques are investigated with the simulator developed in this study. Area, kinematic, sector strengthening ECCM techniques have been investigated. In addition to these evaluated techniques, spectral, denomination and target track gate ECCM are inserted in simulator. For kinematic ECCM, the gate of position directly affects the performance. The wider and narrow gates are inversely proportional with missile performance. Thus, for position gate optimum value of gate size found in this study is $^{FOV}/_{25}$. Area gate is crucial not only for matching but also for the identification block of the missile. Thus, the determination of area gate is also an important performance parameter. With respect to batch-run results, optimum area gate is found as 25%. However, for other gate values (20%, 15%), missile performance is still highly effective as well. Sector strengthening ECCM technique is used only for identification so as to identify sources as *"T"*, if the source is inside the gate of sector strengthening. Note that even when a source satisfies all other ECCM techniques at the identification block, unless it is inside the sector strengthening gate, it will not be labeled as *"T"*. Thus, this gate value is also a crucial performance parameter. In the light of these observations and comments, the gate value of sector strengthening ECCM was chosen as 2^o according to batch-run results.

The original contributions of this study in literature are the determination of the effective evasive maneuvers against IIR missile, applying and defining the effective flare dispensing programs, determination of the optimal initial position and orientation of target with respect to missile. Flare dispensing time sequences, dispenser selection and dispensed flare types are crucial parameters to evaluate effectiveness of the flare dispense programs. In addition to these contributions, atmosphere model, which contains atmospheric transmittance, sky-radiance and path-radiance, is developed in order to evaluate effect of weather condition over performance of proposed IIR missile.

In literature, there are few studies about IIR missile which has advanced ECCM techniques. However, in this study modeled surface-to-air missile has a combination of six advanced ECCM techniques. Simulator can evaluate that which ECCM technique or techniques among these 6 ECCM techniques is/are more effective against target evasive maneuvers, initial position and orientation of target and weather conditions. At the same time, for each ECCM techniques, required parameters can be determined thanks to batch-run results. Thus, advanced ECCM techniques can be modeled easily with information shown and derived in this study.

The last, IIR missiles are used against the naval targets in general. However, proposed IIR missile is a surface-to-air missile and used against aircraft. In the light of these proposed improvements, this study has its own originality among other porposed IIR seeker studies. All these contributions may be helpful for advanced future works and may guide new studies about IIR seeker design equipped with new advanced ECCM techniques.

In general, as future studies, IR seeker E/O part and detector may be modeled nonideally,

which means that E/O and detector loses can be inserted in the seeker model. In this study, all IR scene is generated with respect to the radiation level of sources on scene. However, generation of IR scene may be modeled with respect to detected power/voltage level of sources by the detector. In this direction, detector spectral responsivity, detector area, solid angle, NEP, SNR and sources real area information are required. Similarly, reflectance of 3D models and sun, cloud IR models may be inserted in signature calculations. All these future work suggestions until now are related with the IR signature modeling and scene generation. In a different direction, missile motion model can be updated with a non-linear dynamical model with aerodynamic effects and perturbations. An autopilot may be worked out for the missile to control its maneuvering capability under stability conditions. Instead of the velocity profile, direct thrust force may be used to accelerate the missile, then. For centroid detection, there are better methods to measure the target angular position. As for the last suggestions, in order to present more realistic difficulties for the missile seeker, more advanced ECM techniques may be used; for instance, kinematic and spatially distributed flares is an suitable idea for this job. Optimization of the dispenser rotation and position with respect to aircraft body-coordinates, flare dispensing time, dispensed flare types and dispensed dispenser can be realized in order to improve the performance.

REFERENCES

[1] Dr.EW Johnny Heikell. *Directed Infrared Countermeasures (DIRCM) Principles*. Espoo, Finland 2006-2010, www.heikell.fi/downloads/helicosample.pdf (last visited: 30.07.2013).

[2] Ali Erdem Özcan. Autopilot and guidance for anti-tank imaging infrared guided missiles. Master's thesis, METU, 2008.

[3] Bülent Özkan. *Dynamic Modeling, Guidance, and Conrol of Homing Missiles*. PhD thesis, METU, 2005.

[4] Bryan J Forney. Spectral analysis of ultraviolet clutter sources to improve probability of detection in helicopter uv missile warning systems. Master's thesis, Naval Postgraduate School, 2008.

[5] George M. Siouris. *Missile Guidance and Control Systems*. Springer-Verlag New York, Inc., 2004.

[6] Michal Fiszer. On arrows and needles: Russia's strela and igla portable killers. *Journal of Electronic Defense*, 2002.

[7] Kayhan Çağlar Kılıç. Autopilot and guidance algorithms for infrared guided missiles. Master's thesis, METU, 2006.

[8] John L. Minor. *HELICOPTER EW SELF-PROTECTION from Femtoseconds to Operational Capability*. 349 Berkshire Drive, Riva, Marylan 21140, 2012.

[9] Shahid Baqar. *Low-Cost PC-Based High-Fidelity Infrared Signature Modelling and Simulation*. PhD thesis, Cranfield University, 2007.

[10] Electronic warfare fundamentals, 2000.

[11] Tanel Prank. Thermal imaging using infrared cameras. Technical report, VIA University College Bachelor of Architectural Technology and Construction Management, Denmark, 2009.

[12] David L. Shumaker George J. Zissis, Joseph S. Accetta. *The Infrared and Electro-Optical Systems Handbook. Sources of Radiation*, volume 4. SPIE Optical Engineering Press, 1993.

[13] K. Chrzanowski A. Rogalski. Infrared devices and techniques. *Opto-Electronics Review 10(2), 111–136*, 2002.

[14] Shefali Aggarwai. *Principles of Remote Sensing*. Photogrammetry and Remote Sensing Division, Indian Institute of Remote Sensing, Dehra Dun.

[15] Filippo Neri. *Introduction to Electronic Defense Systems*. SciTech Publishing Inc, 2 edition, 2006.

[16] John L. Minor. *Technical Information SD-12 Characteristics and use of infrared detectors*. 1126-1 Ichino-cho Higashi-ku Hamamatsu City, Japan, 2012.

[17] Emin Güven. The feasibility and efficiency analysis of infrared radiation reduction methods for warships. Master's thesis, Marmara University, 2006.

[18] Johnny Heikell. *Electronic Warfare Self-protection of Battlefield Helicopters: A Holistc View*. PhD thesis, Helsinki University of Technology, Applied Electronics Laboratory, 2005.

[19] Dr. T. W. Tucker. *Evaluating Airliner MANPADS Protection*. Ottawa, ON K2A 3V6, info@tti.on.ca, 2009.

[20] C. R. Viau. *Expendable Countermeasure Effectiveness against Imaging Infrared Guided Threats*. 356 Woodroffe Ave., Ottawa, ON Canada, 2012.

[21] L.W. Abreu F. X. Kneizys. *The MODTRAN 2/3 Report and LOWTRAN 7 Model*. 9 Village Way, North Andover, MA 01845, USA, 1996.

[22] David C. Robertson Alexander Berk, Lawrence S. Bernstein. *The MODTRAN 2/3 Report and LOWTRAN 7 Model*. 99 South Bedford Street, Number 7, Burlington MA, USA, 1989.

[23] J. P. Tremblay; C. R. Viau. A matlab/simulink methodology for simulating dynamic imaging ir missile scenarios for use in countermeasure development and evaluation. *Technologies for Optical Countermeasures VI, 2009 SPIE*, 2009.

[24] The MathWorks. *MATLAB The Language of Technical Computing, Using MATLAB Graphics*. The MathWorks Inc.,3 Apple Hill Drive, Natick MA 01760-2098, 6 edition, 2002.

[25] Rafael Yanushevsky. *Missile Guidance and Control Systems*. CRC Press, Taylor and Francis Group, 2008.

[26] Kenneth W. Iliff Richard E. Maine. *Application of Parameter Estimation to Aircraft Stability and Control*, 1986.

[27] Muhammet Sert. A rule based missile evasion method for fighter aircrafts. Master's thesis, METU, 2008.

[28] Lars Sonneveldt. Nonlinear f-16 model description. Technical report, Control and Simulation Division Faculty of Aerospace Engineering, Delft University of Technology, The Netherlands, 2006.

[29] Jan Roskam. *Airplane Flight Dynamics and Automatic Flight Controls*, 1979.

[30] Peter H. Zipfel. *Modeling and Simulation of Aerospace Vehicle Dynamics*. American Institute of Aeronautics and Astronautics, Inc., 2 edition, 2007.

[31] Özgür Vural. Fuzzy logic guidance system design for guided missiles. Master's thesis, METU, 2003.

[32] Patrick Costello. Simulink simulation of proportional navigation and command to line of sight missile guidance. Master's thesis, Naval Postgraduate School, 1995.

[33] Paul Zarchan. *Tactical and Strategic Missile Guidance*, volume 157. American Institute of Aeronautics and Astronautics Inc., 2 edition, 1994.

[34] Justin M. Lloyd Neil F. Palumbo, Ross A. Blauwkamp. *Basic Principles of Homing Guidance*, 2010.

[35] P. R. Mahapatra U. S. Shukla. The proportional navigation dilemma - pure or true? *IEEE Transactions on Aerospace and Electronics Systems*, 26:382--392, 1990.

[36] Çağdaş Evcimen. Development and comparison of autopilot and guidance algorithms for missiles. Master's thesis, METU, 2007.

[37] Rafael Yanushevsky. *Guidance of Unmanned Aerial Vehicles*. CRC Press, Taylor and Francis Group, 2011.

[38] Richard S. Russell. Non-linear f-16 simulation using simulink and matlab. Technical report, University of Minnesota, 2003.

[39] Eugene A. Morelli Frederico R. Garza. *A Collection of Nonlinear Aircraft Simulations in MATLAB*. Hampton, Virginia 23681-2199, 2003.

[40] Nassim Khaled. *Virtual Reality and Animation for MATLAB and Simulink Users, Visualization of Dynamic Models and Control Simulations*. Springer London Dordrecht Heidelberg New York, 2012.

[41] Sandy Doyle, editor. *Electronic Warfare handbook 2008*. Shephard Press, 2008.

[42] David L. Adamy. *EW 102 A Second Course in Electronic Warfare*. Horizon House Publications, Inc., 2004.

[43] Ernst-Christian Koch. *Pyrotechnic Countermeasures: II. Advanced Aerial Infrared Countermeasures*. Fischbachstrasse 16,D-90552 Röthenbach a. d. Pegnitz, Germany, 2006.

[44] Navy training system plan for the an/ale-47 countermeasures dispensing system, 2002.

[45] Mohammad H. Sadraey. *Aircraft Design, A Systems Engineering Approach*. A John Wiley and Sons, Ltd., Publication, 2013.

[46] Shane Maxemow. That's a drag: The effects of drag forces. *Undergraduate Journal of Mathematical Modeling: One + Two*, 2 Issue:1, Article:4, 2009.